Effects of Turbulence Modeling on RANS Simulations of Tip Vortices

Jesse Wells

Thesis submitted to the faculty of
Virginia Polytechnic Institute and State University
in partial fulfillment of the requirements for the degree of

Master of Science
in
Engineering Mechanics

Saad A. Ragab, Chair
William J. Devenport
Mark S. Cramer

August 3, 2009
Blacksburg, Virginia

Keywords: CFD, RANS, Turbulence Model, Wing-Tip Vortex, Reynolds Stress, Wall Function, Rotor, Wake, Grid

Effects of Turbulence Modeling on RANS Simulations of Tip Vortices

Jesse Wells

ABSTRACT

The primary purpose of this thesis is to quantify the effects of RANS turbulence modeling on the resolution of free shear vortical flows. The simulation of aerodynamic wing-tip vortices is used as a test bed. The primary configuration is flow over an isolated finite wing with aspect ratio, $AR = 8.66$, and Reynolds number, $\mathrm{Re} = 530000$. Tip-vortex velocity profiles, vortex core and wake turbulence levels, and Reynolds stresses are compared with wind tunnel measurements. Three turbulence models for RANS closure are tested: the Lumley, Reece, and Rodi full Reynolds stress transport model and the Sparlart-Allmaras model with and without a proposed modification. The main finding is that simulations with the full Reynolds stress transport model show remarkable mean flow agreement in the vortex and wake due to the proper prediction of a laminar vortex core. Simulations with the Spalart-Allmaras model did not indicate a laminar core and predicted over-diffusion of the tip-vortex.

Secondary investigations in this work include the study of wall boundary layer treatment and simulating the wake-age of an isolated rotorcraft in hover using a steady-state RANS solver. By comparing skin friction plots over the NACA 0012 airfoil, it is shown that wall functions are most effective in the trailing edge half of the airfoil, while high velocity gradient and curvature of the leading edge make them more vulnerable to discrepancies. The rotorcraft simulation uses the modified Spalart-Allmaras turbulence model and shows proper, qualitative, resolution of the interaction between the vortex sheet and the tip vortex.

ACKNOWLEDGEMENTS

I would first like to thank my Mom and Dad for their support of my college education and their valuable life-advice. I would then like to thank my friend and academic advisor, Dr. Ragab. Dr. Ragab has one of the warmest and most welcoming personalities I have ever met. Despite his busy schedule, he has addressed every question or comment of mine with a perspicacious calm; often followed by a remarkably simple figure or equation (sketched on the back of discarded printer paper) that makes all the sense in the world. He has made his office a welcoming place for work and chat and has dedicated many hours with me during both my undergraduate and graduate careers at Virgina Tech. I could not imagine the experience being more pleasant. I have the utmost respect for him. Thank you very, very much. I would also like to thank Dr. Salem Said. He has also spent many hours with me during my time at Virgina Tech teaching me how to use the engineering tools for this thesis and also my undergraduate senior capstone project. Dr. Salem Said has also made his office a welcoming place for me and I greatly appreciate it. I would then like to thank Tim Tomlin for managing the lcc cluster and solving all my computer qualms with routine check-ups and emails. I don't know how else I could have gotten the results. I would then like to thank my committee, Dr. Devenport and Dr. Cramer, for their input and taking the time out of their busy schedules to review my work. I would also like to thank my close friends and family for their support.

Thank you.

TABLE OF CONTENTS

LIST OF TABLES

LIST OF FIGURES

Chapter 1 Introduction

This work is an investigation to the study on turbulence modeling for closure of the Reynolds Averaged Navier-Stokes (RANS) equations. The RANS equations are used in the Computational Fluid Dynamics methodology. The scope of this thesis is limited to aerospace flows and is mainly focused on external, free-shear flow and vortex roll-up. The introduction proceeds with the following sections: an overview of computational fluid mechanics, a description of turbulence and its modeling difficulties, a description of wing-tip vortices, literature review, and a statement on the goals and scope of this thesis.

1.1: Overview of Computational Fluid Dynamics

Computational Fluid Dynamics (CFD) represents the science and methodology of predicting fluid flow by solving governing equations using a numerical algorithm and necessary empirical models. Traditionally, the field of fluid dynamics was served by theoretical and experimental work only. CFD was made possible with the advent of the computer and is continually benefited by increased processor speeds and memory allowance. The best work in fluid dynamics usually involves a tandem of computational and experimental studies backed with strong theoretical foundation.

There are three main components to the implementation of CFD methodology: grid generation, algorithm development, and turbulence / empirical modeling. *Grid generation* refers to segregating the flow domain into individual cells or elements. The grid is used to calculate derivatives and fluxes for the numerical algorithm. The numerical algorithm refers to *how* the derivatives and fluxes are calculated i.e. central differenced or up-winded and order of accuracy etc. Models are used to reduce computational requirements (such as processor speed and memory) involved in resolving turbulent flow. The next section discusses turbulence and why it is necessary to model.

1.2: Overview of Turbulence

Turbulence is a phenomenon of fluid flow that occurs when momentum effects dominate viscous effects (high Reynolds number). It is usually triggered by some kind of disturbance, like flow around an object / streamline separation, and is characterized by

randomly fluctuating velocity fields at many distinct length and time scales. The fluctuating velocity fields manifest themselves as eddies (or regions of swirling motion). Despite the random, chaotic fluctuations, local average velocities (and other fluid properties) can be discerned [1]. The fluctuating velocity fields directly affect transported quantities such as momentum and energy. They too have fluctuating quantities with distinct average values.

In laminar flows, viscous effects dominate momentum effects. Any fluctuating or swirling tendencies are damped by viscous properties of the fluid. The fluid can be thought of as flowing in layers, all of which are parallel to each other. Simple laminar flows often times permit analytic solutions to the Navier-Stokes equations. An accurate solution to laminar flows is a relatively easy task—if an analytic solution is not possible, a numerical one almost always is. The presence of turbulence introduces many difficulties in obtaining a solution because of its inherently wide range of length and time scales.

1.2.1: Difficulty of Simulating Turbulence

Turbulence has been described as the "chief outstanding difficulty of our subject" [2] and "the last unresolved classical physics problem" [3]. The governing equations of fluid flow (Navier-Stokes equations) together with boundary and initial conditions will completely describe any flow condition. However, no analytic solution exists even for the simplest turbulent flow [4]. Most fluid flows of engineering interest exhibit turbulence and, as a result, they have been and will be the source of research for quite some time.

It was stated previously that turbulence is manifested as many eddies belonging to a wide range of length and time scales (also velocity scales). These scales make up a continuous spectrum ranging many orders of magnitude; resolving all scales of turbulence is a daunting task [1]. The largest length scale is on the order of some characteristic length of the flow-field—perhaps the channel width, boundary layer thickness, or mixing layer thickness [4]. These large scale eddies swirl around and shed smaller eddies who in turn do the same in a cascading fashion. The swirling and shedding eddies are unpredictable and highly three dimensional. Compared to the surrounding laminar flow-field, turbulence features huge levels of vorticity in all

directions. This makes it highly diffusive and results in vigorous mixing of mass, momentum, and energy; it is the reason why turbulent boundary layers are more resistant to adverse pressure gradients. Biferale et al. [5] suggested a chaotic turbulence cascade model in which eddies cascade upon each other in the form of a fractal. Kinetic energy from large eddies is transferred to the smaller eddies during the cascading process until it is dissipated into heat. Kolmogorov's famous universal equilibrium theory states that nearly all of the kinetic energy is assumed to dissipate (into heat) in eddies of the smallest scale through viscous effects [6]. If this is true, then the length and time scales of the smallest eddies depend on the rate they receive energy (from larger eddies), ε, and the kinematic viscosity, ν. The kinetic energy (per unit mass) due to turbulence is *k* and then the dissipation is $\varepsilon = -dk/dt$. Using dimensional arguments, Kolmogorov shows that the length and time scales of the *smallest* eddies are $\eta = \left(\nu^3/\varepsilon\right)^{1/4}$ and $\tau \equiv \left(\nu/\varepsilon\right)^{1/2}$, respectively. For an automobile moving at 65mph $\eta \approx 1.8\times10^{-4}$ [1]. The Kolmogorov scales are extremely small and serve to show the resolution needs to properly resolve turbulent flow. However small the Kolmogorov scales may be, they are significantly larger than molecular scales—providing evidence that turbulence is a continuum phenomenon [1]. The purpose of this section is to appreciate the difficulty of dealing with turbulence.

Turbulence can either be *resolved* or *modeled*. Resolving implies proper solution of the governing equations (at all scales) with no modeling or empirical assumptions. Modeling implies a solution that uses some degree of approximation, intuition, and empiricism. The next sections discuss resolving and modeling respectively.

1.2.2: Resolving Turbulence

There are three levels of resolving turbulence: fully resolved, partially resolved, and unresolved. A brief description of each is included below.

A Direct Numerical Simulation (DNS) is one that attempts to fully resolve all regimes of the flow by solving the Navier-Stokes equations all the way down to the Kolmogorov scales. Turbulence / empirical models are not required because DNS resolves the governing equations at all length and time scales. The problem with this technique is that it can consume enormous computational resources and pose numerical difficulties because grid resolution must be on the order of the Kolmogorov scales.

Currently, DNS is a research tool and is only feasible for simple flows at lower Reynolds numbers. Sometimes inflow boundary conditions are prescribed from experimental datasets and a small subset of a total flow is considered. It is universally agreed that DNS is not an option in the foreseeable future—at least for general engineering problems and industrial applications. Moin and Mahesh provide a useful review of the work and contributions of DNS [4].

A Large Eddy Simulation (LES) is one that attempts to partially resolve turbulence. The fundamental idea is that the small scales of turbulence (close to the Kolmogorov scales) mainly dissipate energy and are more homogenous / universal in nature—implying that they can be modeled with relative ease. Zhou calls this a *data redundancy* that should be fully taken advantage of [7]. The larger scales, on the other hand, are more dependent on specific flow conditions and geometry. Therefore, the larger scales are resolved by the governing equations and the smaller scales are spatially filtered out and modeled. Grid resolution is on the order of some turbulent scale. LES offers considerable computational savings over DNS at the expense of modeling and a more complex numerical algorithm. Piomelli provides a more detailed overview of LES and its achievements [7]. LES will probably become the mainstream for CFD, but, not for some time to come. For most engineering applications, particularly aerospace, LES is not yet feasible.

The most computationally practical method of dealing with turbulence is by way of the Reynolds Averaged Navier-Stokes (RANS) equations. With this method turbulence is completely unresolved. Only mean flow quantities are sought after. This is accomplished by time averaging (or Reynolds averaging) the governing Navier-Stokes equations. It was stated previously that, even in turbulent flow, distinct average quantities can be discerned. Therefore, it seems reasonable that one can "get away" with only resolving mean quantities. In the RANS method, all scales of turbulence are modeled; grid resolution must be on the order of the *mean* flow—not a turbulent scale. This offers huge computational savings when compared to both DNS and LES. But, turbulence modeling becomes crucial to the fidelity of the solution. RANS is currently the state-of-art for most types of fluid flows. This present work is an investigation to

turbulence modeling for the RANS equations. More information on both RANS and the turbulence models is included in subsequent sections / chapters.

1.2.3: Modeling Turbulence

The goal of RANS turbulence modeling is to prescribe the correlation, $\overline{u'_i u'_j}$ (Reynolds stress tensor) and thus provide closure of the RANS equations. Physically, the correlation is an artifact of Reynolds averaging the Navier-Stokes equations. It represents the time-averaged rate of turbulent momentum transfer [1]. There are several mainstream turbulence models of varying degrees of complexity. They can be classified by the number of extra partial differential (or *transport*) equations that must be solved (in addition to the conservation equations). Transport equations allow non-local and flow history effects to be included in the description of the local turbulence. The most simple turbulence models are *algebraic* or zero-equation models; they require no solution of differential equations and therefore can only use information from local variables. There are also several prominent one and two equation turbulence models. The most complex class of turbulence models are *Full Reynolds Stress Models* (FRSM) with which each independent component of the Reynolds stress tensor is solved for by a transport equation.

Spalart, one of the most recognizable names in the CFD field, identifies two main challenges posed to a turbulence model [8]. Challenge one is the growth and separation of the boundary layer. Most turbulence models are calibrated with a flat-plate boundary layer and, regardless of complexity, provide outstanding skin friction and boundary layer thickness results (at least for modest curvature and pressure gradient). Challenge two is predicting the transfer of momentum after separation. This is where the benefit of a more complex model comes in and is largely the purpose of the present work.

Nearly all algebraic, one, or two equation turbulence modes rely on Boussinesq's eddy-viscosity model—that the Reynolds stress tensor is proportional to the mean rate of strain tensor by some scalar called the eddy-viscosity. This is to say that the mechanism of turbulence is identical to that of molecular viscosity. The constitutive relationship is most easily seen as $\tau_{ij} = \nu_T s_{ij}$ (applicable for incompressible gases and most one-equation turbulence models that do not calculate *k*, such as the SA model, see section 4.4.3 for

more information). The most common eddy-viscosity models (EVMs) and FRSMs are highlighted in Table 1.1 and 1.2, respectively.

Table 1.1 Common EVMs

Algebraic	Cebeci-Smith (1967) Baldwin-Lomax (1978) Johnson-King (1985)
One-Equation	Bradshaw-Ferriss-Atwell (1967) Baldwin-Barth (1990) Sparlart-Allmaras (1992) Menter (1994)
Two-Equation	$k-\omega$ (various versions from 1972 – 2006) $k-\varepsilon$ (1974) $k-\omega$ SST (1993, and various modifications) $\overline{v}^2-f$ (1991)

Table 1.2 Common FRSMs

Seven-Equation	Launder, Reece & Rodi (LRR) (1975, 1992) Speziale, Sarkar & Gatski (SSR) (1991) Wilcox Stress - ω (2006)

Despite several questionable assumptions, EVMs generally yield acceptable results, particularly for Sparlart's "challenge one". Although, as pointed out by Wilcox [1], these models can fail drastically when the flow contains any of the following features: sudden changes in mean strain rate, curved surfaces, secondary motions, rotation, or if the flow is 3D. Most flows of interest include some or all of these features. A great test bed for the study of complex turbulence models is the generation and evolution of tip vortices. Tip vortices are an example of a coherent turbulent structure [9] and can pose interesting difficulties for a turbulence model.

1.3: Tip Vortices

When a relative free-stream velocity is imparted on a lifting body, such as a wing, the wake rolls up into a vortex near the tip region and evolves downstream by convection.

The main physical mechanism for this occurrence is the pressure difference between the pressure and suction sides of a lifting body. Tip vortices are most commonly studied in the analysis of finite wings, rotorcraft, propellers, compressors, and even flight formation of birds and planes. The existence and persistence of a tip vortex is a crucial element of lifting line theory: that the total circulation of the tip vortex is equal (for potential flow) to the bound circulation over the wing, which is proportional to lift. Their salient features are high swirl velocities [10], low vortex core pressures [9], their contribution to induced drag [11], axial velocity deficits with respect to the surrounding flow [12], and persistence [13-15]. Air traffic regulations specify a flight separation distance of large aircraft of roughly five nautical miles [16]. Figure 1.1 shows a pair finite wing-tip vortices and the induced downwash.

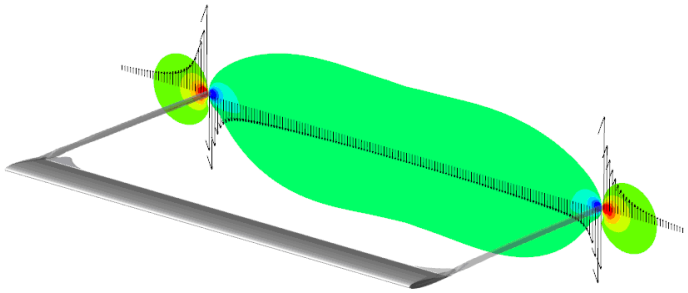

Figure 1.1 Fixed Wing-Tip Vortex and Associated Downwash

Tip vortices have been the subject of numerous theoretical, experimental, and computational investigations. Experimental investigations include [7, 15, 17-21, and many others]. Many of them are plagued by vortex "wandering" or "meandering", an artifact of wind tunnel unsteadiness making even mean velocity profiles unreliable for extended downstream distance. Devenport et al. [15] and Heyes et al. [18] address this issue. Computational investigations are numerous as well [14, 22-28]. The majority of computational investigations are focused on grid generation and algorithm development. Duraisamy [22] studies the entire computational methodology for the resolution of fixed wing and rotorcraft tip-vortices. It contains a great review of the field, but, again most attention is focused on grid and algorithm development.

For less than 0.1% percent error in vortex convection a fifth order accurate scheme or higher and 10 grid points in both spanwise and cross wise directions was used.

The Chimera overlap grid scheme was investigated. The overlap grid is beneficial (and arguably necessary) to mesh complex geometries. For turbulence, the SA model was used. But, other than using a vortical correction, little attention was given to the effect of turbulence modeling. By convecting a laminar isolated vortex Dacles-Mariani et al. [27] agree that a fifth-order upwind biased scheme is required but that 15 – 20 grid points are necessary for grid independence. Egolf et al. [29] convect a Lamb-Oseen vortex and show that 14 grid points across the vortex core and fifth order scheme was required for "minimal diffusion for a long distance". A 9^{th} order scheme and only 7 grid points yielded almost "perfect" convection. Higher order methods were shown to relax grid requirements.

1.4: Pertinent Literature Review

Pertinent literature is divided into four groups: turbulence in the vortex core, sensitizing EVMs to rotation, turbulence model comparisons, and the alternatives.

1.4.1: Turbulence in the Vortex Core

This section describes physical attributes of tip-vortices that pose serious challenges to a turbulence model. The main finding is that the stabilizing swirl velocity tends to overcome the destabilizing axial velocity deficit leading to the eventual laminarization of the vortex core.

Zeman [14] is one of the first to show evidence of the laminar vortex core. Zeman solves the RANS equations using an FRSM on an idealized turbulent line vortex (axisymmetric, zero axial velocity) in cylindrical coordinates. Zeman concludes, "The angular momentum transfer by turbulence is suppressed by the stabilizing effect of flow rotation". He also determines that EVMs will conversely predict a fully turbulent vortex core, resulting in diffusion and core growth.

Ragab et al. [28] perform high Reynolds number LES on an idealized *q* vortex. The *q* vortex is a closer model (compared to a Lamb-Oseen) to a real tip vortex because it includes the axial velocity deficit. Ragab et al. subject their vortex to random controlled perturbations to shed light on the discord between the stabilizing swirl velocity and destabilizing (jet-like) axial velocity deficit. They discover that, if the vortex becomes linearly unstable, disturbances will grow in the form of helical sheets which effectively redistribute axial and angular momentum with the surroundings. Somewhat surprisingly,

the redistribution results in a reduction of axial velocity deficit and strengthened rigid-body rotation and a return to a stable laminar core. The argument is supported with low Reynolds number DNS. These findings are confirmed by Qin [30].

Devenport et al. [15] are the first to provide accurate experimental Reynolds stress measurements in the wake and vortex core of a finite wing using a four-sensor hot wire probe. He develops a correction scheme for "vortex wandering", a phenomenon of wind tunnel unsteadiness. Spectral decomposition is used to show that velocity fluctuations in the vortex core are orders of magnitude lower than the turbulent wake. This is the first conclusive experimental evidence of a laminar core.

Chow et al. [20] perform experimental wind tunnel tests of the near-field roll up of the vortex. Using a seven hole pressure probe they find an initial axial velocity *surplus* as high as $1.77U_\infty$. In addition, they find the vortex is initially *fully turbulent* because of the roll-up of top and bottom boundary layers. But, rather quickly they notice an "extraordinary decay rate of the overall turbulence" consistent with the re-laminarization effect of rigid body rotation. They observe anisotropy and misalignment of the mean strain rate and Reynolds stress tensors.

1.4.2: Sensitizing EVMs to Rotational Effects

There have been attempts made to sensitize EVMs to effects of system rotation and streamline curvature (part of Spalart's challenge two). With respect to model modifications, Spalart explains, "it is highly desirable for new versions to preserve all or almost all of the past successes of a model" [31]. Most EVMs perform well with boundary layer predictions (challenge one) and modifications should not adversely effect this. In general, "New versions create cost, dilute validation work, and erode user confidence." [31]. Nonetheless, there is a decent body of work regarding model modifications.

One form of modification is using a non-linear eddy-viscosity constitutive relationship. Quadratic forms include those proposed by Lumley [32], Saffman [33], Wilcox and Rubesin [34]. Craft et al. [35] propose a cubic form and show consistently better results over the linear variants. The cubic version increases computational time by 10%.

Another form of modification is by adding terms that reflect system rotation to the scalar eddy-viscosity function. Reif et al. [36] add a velocity gradient invariant term and test their model with rotating channel flow, flow over a curved surface, and a rotating backstep diffuser. They find excellent agreement with low Reynolds number DNS comparisons, but caution that it does not necessarily mean high Reynolds number accuracy. Spalart and Shur [37] developed an invariant model add-on to better accommodate rotational effects, although it does not seem to have garnished much attention. Menter et al. [38] hint at future plans to sensitize their SST model. A simple "ad-hoc" modification was used by Dacles-Mariani et al. [27] and Duraisamy [22] based on a suggestion by Spalart. Shear layers are not affected by the modification so as to not erode other validation work. ANSYS offers this variant in its commercial code, FLUENT v6.3 [39].

1.4.3: Turbulence Model Comparisons

It is highly desirable to compare and validate turbulence models. This is based on the facts that: there is no universally accepted model; once a model is engrained in industry and commercial code it is unlikely to change; and, modeling is critical to the fidelity of RANS simulations. Review of the literature indicates that model comparisons of complex flows extending beyond the shear layer are lacking, and even non-existent with FRSMs. The review is limited to comparisons that attempt to show the effects of system rotation; most involve Reynolds stress models.

Wallin et al. [24] wished to ultimately develop a three dimensional unsteady RANS method for full detailed simulation of trailing vortices. As part of this effort, they compare explicit algebraic (two-equation) Reynolds stress models (EARSM) to the full (seven-equation) transport model. They take an isolated Lamb vortex (zero axial velocity) and replace the axial spatial variable with time evolution to see if the EARSMs can predict proper vortex properties seen in Zeman's work (laminar core, minimal circulation overshoot). The EARSMs offer considerable computational savings of the more complex models. Two proposals for the Reynolds stress pressure-strain term are tested: the Launder, Reece, & Rodi (LRR) model and the Speziale, Sarkar, & Gatski (SSG) model. It was found that the algebraic models closely follow the full transport models with one important detail: that the algebraic assumption be made in a streamline based coordinate

system. If this detail is neglected, the algebraic Reynolds stress models were found to be a bad as eddy-viscosity models at predicting a laminar vortex core with minimal circulation overshoot. Unless corrected, this eliminates algebraic Reynolds stress models from contention for more complex 3D flows. Even the simplest wing-tip vortex will drift slightly down and inward, making a streamline based coordinate system unreasonable.

Jakirlic et al. [40] also investigate the problem that severe rotation and streamline curvature pose to eddy-viscosity turbulence models. They simulated rotating pipe flow, channel flow with streamwise and spanwise rotation, rotating Couette flow, swirling flow in a combustion chamber, and swirl in long straight pipes. They show that a strong swirl near a boundary will drastically alter the logarithmic law of the wall, reducing the efficacy of wall functions. They determine that a full Reynolds stress transport model is superior and that the major advantage is its ability to capture stress anisotropy.

Dacles-Mariani et al. [27] perform a computational companion study with Chow et al. [20]. They first solve a subset problem involving convection of a laminar isolated vortex with the purpose of finding a suitable grid and differencing scheme. The Baldwin-Barth (BB) model with and without a rotational correction and the SA model are tested. Despite reasonable crossflow velocity agreement with experiment, they suggest that the misalignment of the principal axes of the Reynolds stress and mean strain rate tensors is detrimental to EVMs at predicting a laminar vortex core. The authors suggest that the issue should be studied further.

Thakur and Shyy [41] review various developments, variations, and implementation methods of FRSMs. Selected versions are tested against the $k-\varepsilon$ model (an EVM) for the following flows: $180°$ bend U-duct, square duct, and a hydraulic turbine draft tube. All of these flows feature system rotation or strong secondary flow features. It was concluded that for all flows "the additional expense incurred in employing the FRSMs is justified".

Hytopoulos et al. [42] review various developments in Reynolds stress models. The importance of the pressure-strain term is investigated. With respect to EVMs, they conclude that Reynolds stress models perform better in some cases but not others.

Liu et al. [26] perform a RANS turbulence model assessment in the simulation of an axial compressor rotor. They use six different turbulence models including the SA,

$k-\varepsilon$, an algebraic mixing length model, SST, $\overline{v}^2 - f$, and the full Reynolds stress model. Comparison is made with experimental SPIV measurements. At the design condition the Reynolds stress model was the only one to adequately predict the structure, strength, and trajectory of the tip leakage vortex. But, they conclude that the tip leakage vortex and the corner vortex will continue to be a big numerical challenge and that the flow mechanism has large discrepancy with reality.

It is evident from this review that, with the exception of the work of Liu et al. performed in 2008, all simulations using FRSMs are on isolated vortices and simple flows.

1.4.4: Alternatives

One of the most common alternatives, particularly for rotorcraft, is modeling the near-field with a RANS solver and coupling it to the far-field with an Euler or vortex lattice solver. The majority of vortex and wake convection is therefore inviscid, and void of turbulence modeling. Examples include Bhagwat et al. [25], Srinivasan et al. [43], Egolf et al.[29], Dimanlig et al. [44], Lockard et al. [23], and many others. Dimanlig et al. mention in 2007,

> The effects of surface boundary-layer turbulence are modeled using the Sparlart-Allmaras one-equation turbulence model. For the off-body grids, the viscous terms are not included since the grid-related dissipation is already much larger than any viscous dissipation that might be present.

There is no mention of the excessive *turbulent* dissipation that is also being avoided. This method of using two different solvers for the near-field and far-field is useful for industry to obtain solutions of complex configurations, but at the same time ignores the important effect that turbulence can have on mean flow.

Mazher [45] proposes a drastic alternative to classical turbulence modeling based on variational methods. Reynolds stresses are represented by functionals to maximize a performance index. A suitable differencing scheme and implementation of the method has not been completed.

1.5: Goal, Scope, and Outline

The main goal of this thesis is to quantify the difference between an FRSM and EVM for simulation of complex vortical flow. It is desired to show that RANS solutions

are very dependent on turbulence modeling, regardless of however excellent the grid or numerical differencing scheme may be. Review of the literature suggests that the benefit of an FRSM is largely unknown. One of two things will eventually occur: either complex RANS turbulence models will become main-stream for time to come; or, the simple act of Reynolds averaging suppresses too much information to properly predict certain flow mechanisms and LES will step in sooner than later. The test bed for this study is predicting the flow mechanism of wing-tip vortices, in particular, the re-laminarization of the vortex core. Secondary goals are to investigate the use of wall functions in boundary layer prediction, and to investigate the SA model for simulating rotorcraft wake-age.

With the exception of the recent work of Liu et al. on the axial compressor rotor, most turbulence model comparisons using FRSMs have been on isolated model vortices (q-vortex, Lamb-Oseen vortex) and other simple configurations (curved channel flow, etc.). The continued advancement of computing power has permitted the use of FRSMs in complex flows. A quantitative comparison between an FRSM and an EVM (with and without corrections) would be very useful. The development and evolution of aerodynamic wing-tip vortices is an excellent test bed. It is a rich field with complex and interesting flow physics.

The scope of the present work is to investigate the effects of RANS turbulence modeling in simulating flow over an isolated wing and isolated rotor (no fuselage). The effects of the grid and numerical algorithm have been researched significantly in previous work and are not fully investigated in the present. The ANSYS commercial CFD code, FLUENT v6.3, is used for all simulations. The rest of this paper is organized as follows:

Chapter two is a review of general theory. It includes the governing equations, Reynolds averaging, and turbulence model formulation.

Chapter two is a 2D flow analysis using the NACA 0012 airfoil. This is a prelude to the full 3D fixed wing case. The main purpose of the 2D analysis is to show grid independence and analyze the use of wall functions for the attached part of the boundary layer (BL). Also the ability for RANS simulations to predict separation and stall is investigated. Pressure distribution plots, gross quantities, and Reynolds stresses are included.

Chapter four includes the analysis of turbulence modeling on finite wing-tip vortex formation and evolution. Included in the analysis is vortex mean velocity profiles, Reynolds stresses, the ability to predict re-laminarization, pressure distributions, comparison of gross quantities, Reynolds stresses, vortex formation analysis, and other qualitative comparisons. Computational results are compared with experimental results from Devenport et al. [15].

Chapter five includes a qualitative investigation of the wake-age from a RANS simulation of a hovering rotorcraft. Only the SA model (with a vortical correction) is tested. This is a computationally demanding problem and serves to show the current state of RANS CFD.

Chapter six summarizes the main conclusions from this thesis.

Chapter 2 Theory

This chapter is a review of general theory. It includes the governing equations, Reynolds averaging, and turbulence model formulation.

2.1: Governing equations

The governing equations of fluid flow are called the Navier-Stokes equations. They are derived based on conservation principals of mass, momentum, and energy and can be written in integral or differential form. The Navier-Stokes equations are coupled non-linear partial differential equations. With boundary and initial conditions, they can be used to solve virtually any flow condition. Numerical differencing schemes can be based on the differential and integral forms. The differential Navier-Stokes equations are shown per unit mass (in the absence of source terms):

Conservation of mass: $$\frac{\partial \rho}{\partial t} + \frac{\partial}{\partial x_i}(\rho u_i) = 0 \tag{2.1}$$

Conservation of momentum: $$\frac{\partial}{\partial t}(\rho u_i) + \frac{\partial}{\partial x_j}(\rho u_j u_i) = \frac{\partial \sigma_{ij}}{\partial x_i} \tag{2.2}$$

Conservation of Energy: $$\frac{\partial}{\partial t}(\rho E) + \frac{\partial}{\partial x_j}(\rho u_j H) = \frac{\partial}{\partial x_j}(u_i t_{ij}) + \frac{\partial}{\partial x_j}\left(k \frac{\partial T}{\partial x_j}\right) \tag{2.3}$$

The spatial variable is x_i, $\rho \equiv$ density, $u_i \equiv$ velocity vector, $E \equiv$ total energy, $H \equiv$ total enthalpy, $k \equiv$ thermal conductivity coefficient, $t_{ij} \equiv$ viscous stress tensor, and $T \equiv$ temperature. Energy and enthalpy equations are:

$$E = e + \frac{1}{2} u_i u_i \tag{2.4}$$

$$H = h + \frac{1}{2} u_i u_i \tag{2.5}$$

Where, $e \equiv$ internal energy per unit mass, $h \equiv$ enthalpy. σ_{ij} is the stress tensor. It can be separated into a conservative part and a dissipative part.

$$\sigma_{ij} = -p\delta_{ij} + t_{ij} \tag{2.6}$$

Where, $-p\delta_{ij}$ is the thermodynamic pressure tensor and t_{ij} is the viscous stress tensor and accounts for molecular viscosity. For most fluids the viscous stresses depend almost entirely on the rate of strain. A Newtonian fluid is one with which the viscous stress tensor is assumed proportional to the rate of strain tensor:

$$t_{ij} \propto s_{ij} \tag{2.7}$$

Where, s_{ij} is the rate of strain tensor:

$$s_{ij} = \frac{1}{2}\left(\frac{\partial u_i}{\partial x_j} + \frac{\partial u_j}{\partial x_i}\right) \tag{2.8}$$

Including viscosity coefficients and considering all components of the viscous stress tensor and the rate of strain tensor the proportionality is shown as:

$$t_{ij} = \tilde{C}_{ijkl} s_{kl} \tag{2.9}$$

$\tilde{C}_{ijkl}$ is a fourth order tensor containing the viscosity coefficients. The Newtonian fluid proportionality is analogous to Hooke's law for an elastic solid—the only difference being stress is proportional to strain for solids. The fourth order viscosity coefficient tensor contains $3^4 = 81$ components but only $6^2 = 36$ of them are independent in the most general case. This is because the viscous stress tensor and the rate of strain tenor are symmetric, meaning they only have six independent components (instead of nine). A further reduction of independent components can be made by assuming isotropy and homogeneity. An isotropic fluid exhibits the same properties in all directions (they are independent of the coordinate system) and a homogenous fluid contains the same properties throughout the entire continuum. With respect to the viscosity coefficients, isotropy implies:

$$\tilde{C}_{ijkl} = \tilde{C}'_{ijkl} \tag{2.10}$$

Where, the prime denotes an arbitrary transformation of the axes. Homogeneity implies:

$$\frac{\partial}{\partial x_m}\tilde{C}_{ijkl} = 0 \tag{2.11}$$

For an isotropic, homogenous, Newtonian fluid, the principal axes of the rate of strain tensor, s_{ij}, and the viscous stress tensor, t_{ij}, are coincident throughout the entire domain. It can be shown by invoking the isotropy assumption (with several rotations and reflections of the axes) that the 4th order viscosity coefficient tensor only contains two unique components (μ and λ, the first and second coefficients of viscosity). The constitutive relationship between the viscous stress tensor and the rate of strain tensor can then be simplified:

$$t_{ij} = 2\mu s_{ij} + \lambda s_{mm}\delta_{ij} \tag{2.12}$$

Where, $s_{mm} \equiv \frac{\partial u_m}{\partial x_m}$. With statistical mechanics it can be shown for a monatomic gas $\lambda = -\frac{2}{3}\mu$. This assumption is known as Stokes' hypothesis, and is used in nearly all gases for CFD simulations and also in the present work. Equation 1.12 is then simplified to:

$$t_{ij} = 2\mu s_{ij} - \frac{2}{3}(\mu s_{mm})\delta_{ij} \tag{2.13}$$

The need for compressibility effects ($\frac{D\rho}{Dx_i} \neq 0$) increases as the local flow speed approaches transonic. It becomes crucial in problems with combustion, heat transfer, and supersonic flow / shockwaves. In the present work, compressibility effects are included for all flows, even at low Mach number. The inclusion of compressibility effects does not significantly increase computation time, stiffness, or resource. The standard continuity and momentum equations in the FLUENT code are already configured for compressibility effects. Necessary add-ons are the energy equation (2.3) and a thermodynamic equation of state. It is very common for most gases, including air, to use the ideal gas law as the equation of state:

$$\rho = \frac{p}{\frac{R}{M_W}T} \tag{2.14}$$

Where, p, is the local static pressure, R, is the universal gas constant, M_W, is the molecular weight, and T, is temperature. Temperature is obtained from solution of the

energy equation. All flows in the present work are solved in a steady state frame of reference. For finite wing applications the steady state reference frame is translational and moves at flight velocity. For rotorcraft applications the steady state frame is rotational and moves with the same angular velocity as the rotors (centripetal and Coriollis effects are added to the governing equations as source terms). As a result, all derivatives with respect to time are zero ($\frac{\partial}{\partial t}[] = 0$).

2.2: Reynolds Averaging

Reynolds averaging [45] is a technique used to derive equations that govern the mean flow variables. It is founded on the idea that a fluid flow can be described by statistically averaged quantities, even in extreme turbulence. Each flow variable can be represented by a mean part and a fluctuating part i.e. $\phi(x_i,t) = \Phi(x_i,t) + \phi'(x_i,t)$, where the first and second terms on the right hand side are mean and fluctuating parts, respectively. The fluctuating part is with respect to the mean and can be orders of magnitude smaller than mean flow scales. Flow variables can be averaged over time for "steady" fluctuations, $\Phi_T(x_i) = \lim_{T\to\infty} \frac{1}{T} \int_t^{t+T} \phi(x_i,t)dt$, or, over space for homogenous fluctuations, $\Phi_V(t) = \lim_{V\to\infty} \frac{1}{V} \iiint_V \phi(x_i,t)dV$. An ensemble average is when variables are averaged over a set of N unique simulations i.e. $\Phi_E(x_i,t) = \lim_{N\to\infty} \frac{1}{N} \sum_{n=1}^{N} \phi(x_i,t)$. Time averaging is most common for statistically stationary flows. Even if the flow is unsteady on a macro-scale, fluctuations can still be averaged because their time scales are much smaller. For compressible flow, it is mathematically convenient to time average velocity fluctuations as *density-weighted* averages. For the velocity variable this becomes, $U_T(x_i) = \lim_{T\to\infty} \int_t^{t+T} \rho(x_i,t)u(x_i,t)dt$. This technique was developed by Farve [46] and is called *Farve-averaging*, although in literature, *Reynolds-average* is sometimes used all-inclusively.

The steady state compressible Navier-Stokes equations are repeated below for convenience (with the substitution for $\sigma_{ij} = -p\delta_{ij} + t_{ij}$). Even though the energy

equation is also Farve-averaged, it is not critical for the purpose of explanation and is solved in a de-coupled manner from the mass and momentum equations.

Conservation of mass: $$\frac{\partial \rho}{\partial t} + \frac{\partial}{\partial x_i}(\rho u_i) = 0 \tag{2.1}$$

Conservation of momentum: $$\frac{\partial}{\partial t}(\rho u_i) + \frac{\partial}{\partial x_j}(\rho u_j u_i) = -\frac{\partial p}{\partial x_i} + \frac{\partial t_{ij}}{\partial x_j} \tag{2.2}$$

Now each variable is replaced by a mean part and a fluctuating part. If the flow is assumed to be steady on the macro-scale, average quantities are only functions of space:

$$\rho(x_i,t) = \overline{\rho}(x_i) + \rho'(x_i,t) \tag{2.15}$$

$$p(x_i,t) = P(x_i) + p'(x_i,t) \tag{2.16}$$

$$\overline{\rho} u_i(x_i,t) = \overline{\rho} U_i(x_i) + \overline{\rho} u'_i(x_i,t) \tag{2.17}$$

Equations 2.15– 2.17 are then substituted into the Navier-Stokes equations.

$$\frac{\partial}{\partial t}(\overline{\rho} + \rho') + \frac{\partial}{\partial x_i}(\overline{\rho} U_i + \overline{\rho} u'_i) = 0 \tag{2.18}$$

$$\frac{\partial}{\partial t}(\overline{\rho} U_i + \overline{\rho} u_i') + \frac{\partial}{\partial x_j}(\overline{\rho} U_i U_j + \overline{\rho} u'_i U_j + \overline{\rho} U_i u'_j + \overline{\rho} u'_i u'_j) =$$

$$-\frac{\partial}{\partial x_i}(P + p') + \frac{\partial}{\partial x_j}(\bar{t}_{ij} + t'_{ij}) \tag{2.19}$$

To complete the process, each term is averaged (denoted with an overbar) and assuming that averaging and differentiation commute, one obtains:

$$\frac{\partial}{\partial t}(\overline{\overline{\rho}} + \overline{\rho'}) + \frac{\partial}{\partial x_i}(\overline{\overline{\rho} U_i} + \overline{\overline{\rho} u'_i}) = 0 \tag{2.20}$$

$$\frac{\partial}{\partial t}(\overline{\overline{\rho} U_i} + \overline{\overline{\rho} u_i'}) + \frac{\partial}{\partial x_j}(\overline{\overline{\rho} U_i U_j} + \overline{\overline{\rho} u'_i U_j} + \overline{\overline{\rho} U_i u'_j} + \overline{\overline{\rho} u'_i u'_j}) =$$

$$-\frac{\partial}{\partial x_i}(\overline{P} + \overline{p'}) + \frac{\partial}{\partial x_j}(\overline{\bar{t}_{ij}} + \overline{t'_{ij}}) \tag{2.21}$$

The average of any term with a single fluctuating quantity is zero. If a term has more than one fluctuating quantity, a statistical correlation between the variables must be accounted for. Eliminating all zero terms and assuming steady state yields the steady state compressible Reynolds Averaged Navier Stokes (RANS) equations:

$$\frac{\partial}{\partial x_i}\left(\bar{\rho}U_i\right)=0 \tag{2.22}$$

$$\frac{\partial}{\partial x_j}\left(\bar{\rho}U_iU_j+\overline{\rho u'_i u'_j}\right)=-\frac{\partial P}{\partial x_i}+\frac{\partial \bar{t}_{ji}}{\partial x_j} \tag{2.23}$$

In the derivation, the expansion of t_{ij} was not included because it does not introduces new terms (or correlations). remains the same. The only new term from Reynolds averaging is $\bar{\rho}\overline{u'_i u'_j}$. It is commonly re-written on the right-hand side of the equation, introducing a negative sign:

$$\frac{\partial}{\partial x_j}\left(\bar{\rho}U_iU_j\right)=-\frac{\partial P}{\partial x_i}+\frac{\partial}{\partial x_j}\left[\bar{t}_{ji}-\overline{\rho u'_i u'_j}\right] \tag{2.24}$$

Physically, it represents the time averaged rate of turbulent momentum transfer. It is famously referred to as the Reynolds stress tensor:

$$\tau_{ij}=-\overline{\rho u'_i u'_j}=-\bar{\rho}\begin{bmatrix}\overline{u'^2} & \overline{u'v'} & \overline{u'w'}\\ \cdots & \overline{v'^2} & \overline{v'w'}\\ \cdots & \cdots & \overline{w'^2}\end{bmatrix} \tag{2.25}$$

Where, $u'_i=\langle u' \quad v' \quad w'\rangle$. Reynolds averaging introduces six addition unknowns to the governing equations. Because there are more unknown variables than equations, the six Reynolds stresses must be prescribed using a turbulence model. This provides *closure* to the RANS equations.

A turbulence model that prescribes a Reynolds stress tensor as shown in equation 2.24 is called a *first-order closure* or *first-moment closure*. It is possible to extract a differential Reynolds stress tensor by taking higher central "moments" of the Navier-Stokes equations.

2.3: Second-Moment Closure

The Reynolds averaging technique makes logical sense from a physical standpoint: that one can solve an equation for average flow quantities. The Reynolds stress correlation also makes physical sense. The so called *first order* technique described above yields scalar Reynolds stress relationship. It is sometimes desirable to have a differential form. This can be performed with a manipulation of the Navier-Stokes equation that produces extra correlations (of unclear physical meaning). This is

done (prior to time averaging) by multiplying each term of equation 2.23 by a fluctuating primitive variable, the density weighted velocity fluctuation, $\tilde{u}''_i$ (because these are Farve-averaged and the equations are solved for in the Euler reference frame). Then, the time average of each term is taken, just like the above derivation. Following Wilcox [1] it is convenient to denote a Navier-Stokes Operator:

$$\mathrm{N}(\tilde{u}_i) = \frac{\partial}{\partial t}\left(\rho\tilde{u}_i\right) + \frac{\partial}{\partial x_j}\left(\rho\tilde{u}_j\tilde{u}_i\right) + \frac{\partial p}{\partial x_i} - \frac{\partial t_{ij}}{\partial x_j} = 0 \tag{2.26}$$

Then, the time average (denoted with the overbar) of the following quantity is taken:

$$\overline{\tilde{u}''_i\,\mathrm{N}(\tilde{u}_j) + \tilde{u}''_j\,\mathrm{N}(\tilde{u}_i)} = 0 \tag{2.27}$$

Expansion of equation 2.27 yields the transport equations for the Reynolds stress tensor:

$$\begin{aligned}
&\frac{\partial}{\partial t}(\overline{\rho}\tau_{ij}) + \frac{\partial}{\partial x_k}(\overline{\rho}\tilde{u}_k\tau_{ij}) = -\overline{\rho}\tau_{ik}\frac{\partial\tilde{u}_j}{\partial x_k} - \overline{\rho}\tau_{jk}\frac{\partial\tilde{u}_i}{\partial x_k} + \overline{\rho}\varepsilon_{ij} - \overline{\rho}\Pi_{ij} \\
&+ \frac{\partial}{\partial x_k}\left[-\left(\overline{t_{kj}\tilde{u}''_i + t_{ki}\tilde{u}''_j}\right) + \overline{\rho}C_{ijk}\right] + \tilde{u}''_i\frac{\partial P}{\partial x_j} + \tilde{u}''_j\frac{\partial P}{\partial x_i}
\end{aligned} \tag{2.28}$$

2.4: Spalart-Allmaras Model Theory

The Spalart-Allmaras (SA) [47] model is a one equation eddy-viscosity model. A single transport equation is solved for a working variable, $\tilde{\nu}$, identical to the eddy-viscosity, ν_T, except in near wall viscous boundary layers. The SA transport equation (2.29) and its various algebraic relationships are shown:

$$\frac{\partial}{\partial t}\left(\rho\tilde{\nu}\right) + \frac{\partial}{\partial x_i}\left(\rho\tilde{\nu}u_i\right) = G_\nu + \frac{1}{\sigma_{\tilde{\nu}}}\left[\frac{\partial}{\partial x_j}\left\{\left(\mu+\rho\tilde{\nu}\right)\frac{\partial\tilde{\nu}}{\partial x_j}\right\} + C_{b2\rho}\left(\frac{\partial\tilde{\nu}}{\partial x_j}\right)^2\right] - Y_\nu \tag{2.29}$$

Eddy viscosity: $\nu_T = \tilde{\nu}f_{v1}$ (2.30)

where, $f_{v1} = \dfrac{\chi^3}{\chi^3 + C_{v1}{}^3}$, and $\chi = \dfrac{\tilde{\nu}}{\nu}$. (2.31)

Production: $G_\nu = C_{b1}\rho\tilde{S}\tilde{\nu}$ (2.32)

where, $\tilde{S} \equiv S + \dfrac{\tilde{\nu}}{\kappa^2 d^2}f_{v2}$ (2.33)

$$S \equiv \sqrt{2\omega_{ij}\omega_{ij}} \quad \text{and} \quad \omega_{ij} = \frac{1}{2}\left(\frac{\partial u_i}{\partial x_j} - \frac{\partial u_j}{\partial x_i}\right) \tag{2.34}$$

$$f_{v2} = 1 - \frac{\chi}{1+\chi f_{v1}} \tag{2.35}$$

Destruction: $$Y_\nu = C_{w1}\rho f_w \left(\frac{\tilde{\nu}}{d}\right)^2 \tag{2.36}$$

where, $$f_w = g\left[\frac{1+C^6{}_{w3}}{g^6 + C^6{}_{w3}}\right]^{1/6} \tag{2.37}$$

$$g = r + C_{w2}\left(r^6 - r\right) \tag{2.38}$$

$$r \equiv \frac{\tilde{\nu}}{\tilde{S}\kappa^2 d^2} \tag{2.39}$$

Model constants: $C_{b1} = 0.1355$, $C_{b2} = 0.622$, $\sigma_{\tilde{\nu}} = 7.1$,

$$C_{w1} = \frac{C_{b1}}{\kappa^2} + \frac{\left(1+C_{b2}\right)}{\sigma_{\tilde{\nu}}},\ C_{w2} = 0.3,\ C_{w3} = 2.0,$$

$$\kappa = 0.4187$$

The formulation above is the original SA model presented in 1992 [47]. Spalart later proposed a simple modification in the production term. Instead of equation 2.34 he suggested using [27]:

$$S \equiv \left|\omega_{ij}\right| + 2.0\min\left(0, \left|s_{ij}\right| - \left|\omega_{ij}\right|\right) \tag{2.40}$$

This modification keeps the SA model Galilean invariant and it is passive in most boundary layers, so as to no erode previous validation work. The modification effectively reduces the production of turbulent viscosity when vorticity is greater than strain, $\left|\omega_{ij}\right| > \left|s_{ij}\right|$. This often occurs in free-shear vortical flows. The modification has been used in simulating wing-tip vortices by Dacles-Mariani et al. [27] and Duraisamy [22]. This modification is available in FLUENT CFD code as an option and is tested in this thesis.

2.5: Full Reynolds Stress Model Theory

Full Reynolds Stress Models (FRSMs) are second moment-closure models and therefore use the differential form of the Reynolds stress tensor, equation 2.28 repeated here:

$$\frac{\partial}{\partial t}(\overline{\rho}\tau_{ij}) + \frac{\partial}{\partial x_k}(\overline{\rho}\tilde{u}_k\tau_{ij}) = -\overline{\rho}\tau_{ik}\frac{\partial \tilde{u}_j}{\partial x_k} - \overline{\rho}\tau_{jk}\frac{\partial \tilde{u}_i}{\partial x_k} + \overline{\rho}\varepsilon_{ij} - \overline{\rho}\Pi_{ij}$$

$$+ \frac{\partial}{\partial x_k}\left[-\left(\overline{t_{kj}\tilde{u}'_i + t_{ki}\tilde{u}'_j}\right) + \overline{\rho}C_{ijk}\right] + \tilde{u}'_i\frac{\partial P}{\partial x_j} + \tilde{u}'_j\frac{\partial P}{\partial x_i} \qquad (2.28)$$

From the above equation, four groupings of terms need to be modeled. They are (written in terms of fluctuating velocities, u_i'):

Turbulent Diffusion: $D_{T,ij} \equiv -\frac{\partial}{\partial x_k}\left[\overline{\rho u'_i u'_j u'_k} + \overline{p\left(\delta_{kj}u'_i + \delta_{ik}u'_j\right)}\right]$ (2.41)

Buoyancy Production: $G_{ij} = -\rho\beta\left(g_i\overline{u'_j\theta} + g_j\overline{u'_i\theta}\right)$ (2.42)

Pressure-Strain: $\phi_{ij} = p\left(\frac{\partial u'_i}{\partial x_j} + \frac{\partial u'_j}{\partial x_i}\right)$ (2.43)

Dissipation: $\varepsilon_{ij} = -2\mu\overline{\frac{\partial u'_i}{\partial x_k}\frac{\partial u'_j}{\partial x_k}}$ (2.44)

The turbulent diffusion term is simplified in FLUENT to a scalar, turbulent diffusivity, μ_T:

$$D_{T,ij} = \frac{\partial}{\partial x_k}\left(\frac{\mu_t}{\sigma_k}\frac{\partial u'_i u'_j}{\partial x_k}\right) \qquad (2.45)$$

where, $\mu_t = \rho C_\mu \frac{k^2}{\varepsilon}$, $C_\mu = 0.09$ (2.46)

Buoyancy Production is simplified when using the ideal gas law as:

$$G_{ij} = -\frac{\mu_t}{\rho\,\mathrm{Pr}_t}\left(g_i\frac{\partial p}{\partial x_j} + g_j\frac{\partial \rho}{\partial x_i}\right) \qquad (2.47)$$

The pressure-strain is the most sensitive and critical term to model. Variations of the Reynolds stress model are usually defined by how the pressure-strain term is modeled. The FLUENT default model [39] is used in this thesis. The pressure-strain term is modeled using the Launder, Reece, and Rodi (LRR) method [48]. It is common practice

to separate it into three parts, $\phi_{ij} = \phi_{ij,1} + \phi_{ij,2} + \phi_{ij,w}$, and model each separately. The first term, on the right-hand side, is called the slow return-to-isotropy:

$$\phi_{ij,1} \equiv -C_1 \rho \frac{\varepsilon}{k}\left[\overline{u'_i u'_j} - \frac{2}{3}\delta_{ij}k\right],\ C_1 = 1.8 \tag{2.48}$$

The second is called the rapid term and is modeled:

$$\sigma_{ij,2} \equiv -C_2\left[\left(P_{ij} + F_{ij} + G_{ij} - C_{ij}\right) - \frac{2}{3}\delta_{ij}\left(P + G - C\right)\right] \tag{2.49}$$

where, $C_2 = 0.60$ and,

$$P_{ij} \equiv -\rho\left(\overline{u'_i u'_j}\frac{\partial u_j}{\partial x_k} + \overline{u'_j u'_k}\frac{\partial u_i}{\partial x_k}\right), \text{ and } P = \frac{1}{2}P_{ii} \tag{2.50}$$

$$F_{ij} \equiv -2\rho\Omega_k\left(\overline{u'_j u'_m}\varepsilon_{ikm} + \overline{u'_i u'_m}\varepsilon_{jkm}\right), \text{ and } F = \frac{1}{2}F_{ii} \tag{2.51}$$

$$C_{ij} \equiv \frac{\partial}{\partial x_k}\left(\rho u_k \overline{u'_i u'_j}\right) \text{ , and } C = \frac{1}{2}C_{ii} \tag{2.52}$$

The G_{ij} term is define in equation 1.44, and again $G = \frac{1}{2}G_{ii}$. $\phi_{ij,w}$ is called the wall-reflection term.

$$\phi_{ij,w} \equiv C'_1 \frac{\varepsilon}{k}\left(\overline{u'_k u'_m}n_k n_m \delta_{ij} - \frac{3}{2}\overline{u'_i u'_k}n_j n_k - \frac{3}{2}\overline{u'_j u'_k}n_i n_k\right)\frac{C_l k^{3/2}}{\varepsilon d}$$
$$+ C'_2\left(\phi_{km,2}n_k n_m \delta_{ij} - \frac{3}{2}\phi_{ik,2}n_j n_k - \frac{3}{2}\phi_{jk,2}n_i n_k\right)\frac{C_l k^{3/2}}{\varepsilon d} \tag{2.53}$$

where, $C'_1 = 0.5$, $C'_2 = 0.3$, $n \equiv$ unit normal, $d \equiv$ normal distance to wall, $C_l = \frac{C_\mu^{3/4}}{\kappa}$, $C_\mu = 0.09$, von Karman constant, $\kappa = 0.4187$.

Regarding Reynolds stress models, Hytopoulos et al. [42] state,

> The motivation behind the use of the second-order closures can be summarized as follows: If crude approximations for the second moments in eddy viscosity models can yield adequate approximations for first-order moments, then it is reasonable to assume that crude approximations for the third order moments can yield adequate approximations for the second-order moments in Reynolds-stress transport models.

2.6: Conclusion

This chapter reviewed the governing equations, Reynolds averaging techniques, and turbulence model formulation. Three turbulence models are tested in this thesis. They are summarized in Table 2.1.

Table 2.1: Tested Turbulence Models

Model	Type	Modeling Options
SA original	1-equation EVM	$S \equiv \sqrt{2\omega_{ij}\omega_{ij}}$
SA w/ correction	1-equation EVM	$S \equiv \left\|\omega_{ij}\right\| + 2.0\min\left(0, \left\|s_{ij}\right\| - \left\|\omega_{ij}\right\|\right)$
LRR Reynolds stress	7-equation FRSM	Wall reflection effects included

Chapter 3 NACA 0012 Airfoil Simulation

Chapter three is a 2D analysis of a NACA 0012 airfoil. This is a prelude to the full 3D fixed wing study. The main purpose is to show grid independence and analyze the use of wall functions. Also the ability for RANS simulations to predict separation and stall is analyzed. Pressure distribution plots, gross quantities, and Reynolds stresses are included.

3.1: NACA 0012 Airfoil Geometry

The NACA 0012 airfoil is used in all 2D and 3D fixed wing (chapter four) simulations. The geometry is shown in Figure 3.1. It was created with ANSYS' GAMBIT pre-processor by interpolating 129 unique points from a dataset that defines the airfoil. The dataset was downloaded from the UIUC Airfoil Coordinates Database [49] on the internet and is included in Appendix B. The reason for using the NACA 0012 airfoil is to replicate the experimental configuration of Devenport et al. [15]. It is one of the most commonly tested airfoils and is suitable for subsonic and transonic flows. It lends itself well to CFD simulations because it is relatively thin and has zero camber. Camber adds streamline curvature effects which is bad news for EVMs. Most turbulence models, such as the SA, calibrate shear layers with flow of over a flat plate [47]. The closer the airfoil resembles a flat plate the better. For fair comparison, it is desirable to give all turbulence models the best chance at success.

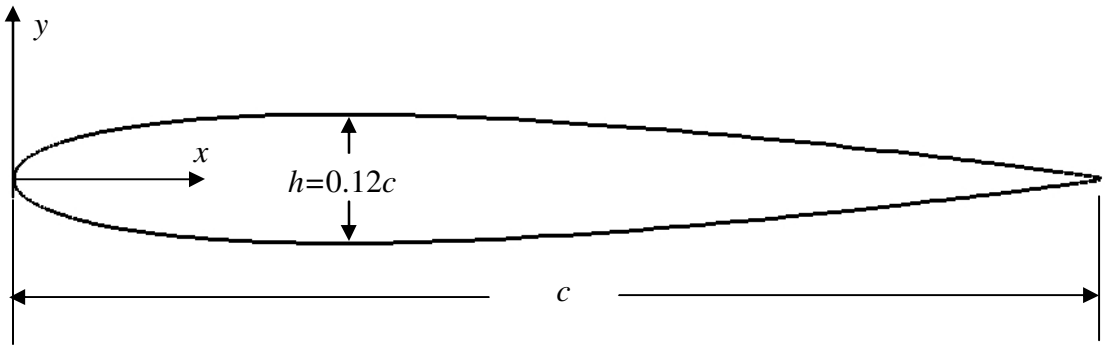

Figure 3.1 Schematic of NACA 0012 Airfoil

3.2: Numerical Errors and Grid Considerations

There are two types of errors incurred during any numerical computation: errors due to the differencing scheme, and errors due to modeling. Gridding is intrinsically linked to the differencing scheme. As the literature review indicates, there has been significant work performed in reducing differencing errors. The main effort of this thesis is quantifying turbulence modeling errors and to properly do so the errors from differencing must be accounted for. This is done by running identical simulations on multiple grids. Three different NACA 0012 2D grids were created. It is desirable to obtain a solution that is completely independent of grid effects. This is an excellent quality reassurance method.

Grid independence is accomplished when the number of nodes in each dimension can be reduced by a half and the exact same solution is obtained. For a 2D grid comprised of quadrilateral elements this means a reduction by a factor of 2^2, and, for a 3D grid of hexahedral elements, a factor of 2^3. Because of the (exponentially) increased reduction factor for 3D simulations (not to mention increased complexity) it is extremely difficult to obtain grid independence for complex 3D flows.

Much care needs to taken when developing a grid. Characteristics of a quality grid include: minimal element-to-element stretching ratio, adequate resolution of high-gradient regions (i.e. boundary layer, vortices, etc.), and minimal element skewness. Also, even though it is very difficult to avoid, high aspect ratio elements can increase convergence time and / or pose numerical difficulties. When the numerical algorithm is implemented, skewed elements lead to ill-conditioned matrices. There has been a great deal of previous research performed to quantify numerical errors due to stretching ratio. A good guideline is to keep the ratio, $r \leq 1.1$ [22, 31]. But, arguably, the most important part of the grid is the boundary layer resolution.

3.3: Boundary Layers

A guideline to boundary layer grid resolution can be formed using dimensional arguments and empiricism. The most consequential variables in a near incompressible boundary layer are molecular viscosity, μ, and surface shear stress, τ_w. It is convenient to rewrite them as kinematic viscosity, $\nu = \mu / \rho$, and τ_w / ρ. Turbulent velocity and

length scales are $u_T \equiv \sqrt{\tau_w / \rho}$ and $l_T = \nu / \sqrt{\tau_w / \rho}$ respectively. The law of the wall [50] is an empirically derived formula that can be used to predict the boundary layer velocity field:

$$\text{Law of the Wall:} \qquad u^+ = \frac{1}{\kappa} \ln y^+ + C \tag{3.1}$$

Where, $u^+ \equiv \frac{U}{u^T}$, $y^+ \equiv \frac{u_T y}{\nu}$, $\kappa \approx 0.41$ (Karman's constant), and $C \approx 5$ (u^+ and y^+ are dimensionless). The boundary layer is considered to be made up of three distinct layers: the viscous sub-layer, the log layer, and the defect layer. The law of the wall gives excellent agreement in the log layer as long as near wall swirl and rotation effects are minimal [40]. The dimensionless quantity, y^+, is commonly used as the guideline for determining the off-wall normal length of the first grid element. In Spalart's review, *Trends in Turbulence Treatments* [31], he states that typical values of $y^+ \approx 2$ are used, but that FRSMs can require smaller. The FLUENT manual suggests $y^+ \approx 1$ to fully resolve the viscous sub-layer [39]. If $y^+ = 1$, than one *wall unit* is $y = \nu / u_T$. It is attempted for the first off-wall normal length to be a *wall unit.* Unfortunately, τ_w is not known *a priori* when one creates a grid; therefore, an analytic flat-plate approximation based on the turbulent Blasius velocity profile was used [11]:

$$\tau_w(x) \approx \frac{0.0135 \mu^{1/7} \rho^{6/7} U_\infty{}^{13/7}}{x^{1/7}} \tag{3.2}$$

For the simulation with $\mathrm{Re} = 530000$ the constants are: $\mu = 1.7894 \times 10^{-5} \, {kg}/{m-s}$, $\rho \approx \rho_\infty = 1.225 \, {kg}/{m^3}$, $U_\infty = 38.1 \, {m}/{s}$. Substituting these into equation 3.2 and then into the wall unit equation gives the recommended wall spacing. This is show in Figure 3.2. The wall unit distance is very small, $O(10^{-6})$. To relax the unit wall normal spacing requirements, wall functions can be used. Figure 3.14 *b)* in the results section confirms a fully resolved boundary layer.

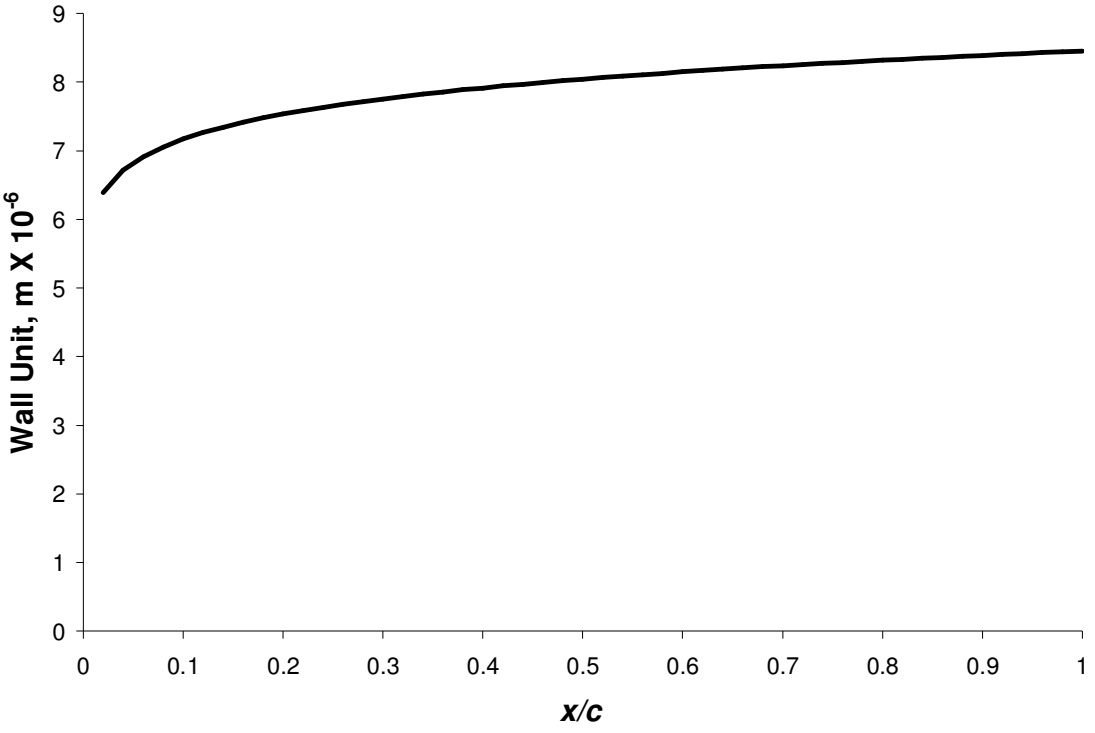

Figure 3.2 Flat Plate Boundary Wall Unit

3.4: Wall Functions

It was stated in the previous section that if wall curvature and other flow rotation effects are minimal, then the boundary layer can be predicted quite well with empirical models. Instead of resolving the boundary layer a *wall function* can be used. The FLUENT manual recommends if wall functions are used that the y^+ criteria can be relaxed from $y^+ \approx 1$ to $y^+ \approx 30$ [39]. FLUENT's standard wall function equations are those of Launder and Spalding [51] are shown:

Momentum: $$U^* = \frac{1}{\kappa}\ln(Ey^*) \tag{3.3}$$

where $$U^* \equiv \frac{U_P C_\mu^{1/4} k_P^{1/2}}{\tau_w / \rho} \tag{3.4}$$

$$y^* \equiv \frac{\rho C_\mu^{1/4} k_P^{1/2} y_P}{\mu} \tag{3.5}$$

Energy:
$$T^* = \Pr\, y^* + \frac{1}{2}\rho \Pr \frac{C_\mu^{1/4} k_P^{1/2}}{\dot{q}} U_P^{\,2} \quad (y^* < y_T^{\,*}) \tag{3.6}$$

$$T^* = \Pr_t \left[\frac{1}{\kappa} \ln(E y^*) + P \right] + \frac{1}{2}\rho \frac{C_\mu^{1/4} k_P^{1/2}}{\dot{q}} \left\{ \Pr_t U_P^{\,2} + (\Pr - \Pr_t) U_c^{\,2} \right\} \quad (y^* > y_T^{\,*}) \tag{3.7}$$

where
$$T^* = \frac{(T_w - T_P)\rho c_p C_\mu^{1/4} k_P^{1/2}}{\dot{q}} \tag{3.8}$$

$$P = 9.24 \left[\left(\frac{\Pr}{\Pr_t} \right)^{3/4} - 1 \right] \left[1 + 0.28 e^{-0.007\, \Pr/\Pr_t} \right] \tag{3.9}$$

where

κ = von Karman constant (=0.4187)

E = empirical constant (=9.793)

U_P = mean velocity of the fluid at point P

k_P = turbulence kinetic energy at point P

y_P = distance from point P to the wall

μ = viscosity

ρ = density

c_p = specific heat

$\dot{q}$ = wall heat flux

T_P = temperature at first off-wall element

T_w = wall temperature

$\Pr = \mu c_p / k_f$ molecular Prandtl number

$\Pr_t$ = turbulent Prandtl number (=0.85 at the wall)

A = Van Driest constant (=26)

U_c = mean velocity magnitude at $y^* = y_T^{\,*}$

The two different types of grid wall treatments are shown in Figure 3.3.

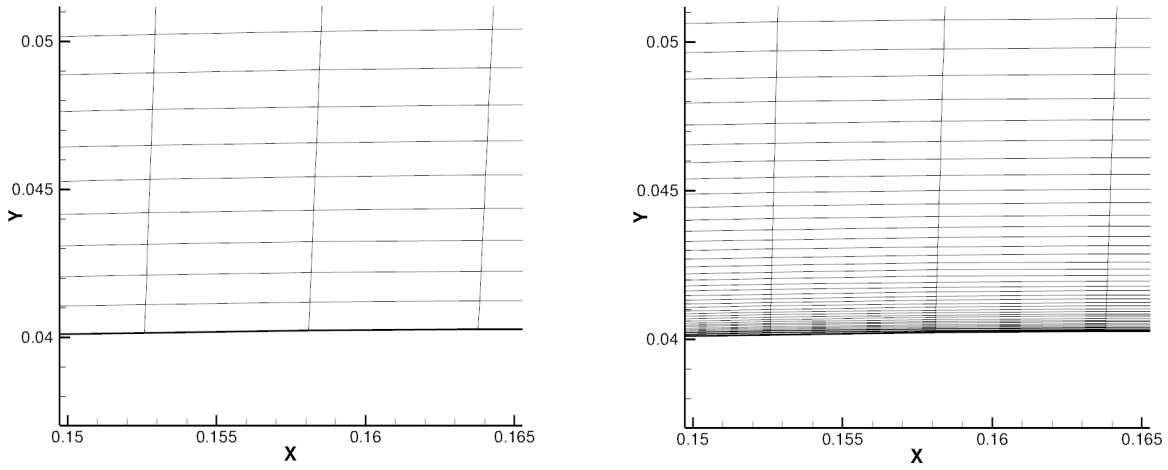

a) Unresolved Boundary Layer

b) Resolved Boundary Layer

Figure 3.3 Boundary Layer Grid Comparison

3.5: Grid Description

Three 2D grids were created with GAMBIT. They are summarized in Table 3.1. The different grids are needed to quantify differencing errors and errors from wall functions. Resolved boundary layers use the $y^+ \approx 1$ criteria, and unresolved use $y^+ \approx 30$.

Table 3.1 Grid Summary

Grid name	Element count	Wall function use	Highest aspect ratio element in BL	Wall-normal stretching ratio, *r*
Fine R-BL (Resolved BL)	60600	No	790	1.1
Fine U-BL (Unresolved BL)	58248	Yes	15	1.04
Coarse	15204	Yes	30	1.1

The computation domain and boundary conditions of all grids are identical. They are shown in Figure 3.3. An image of each grid is shown in Figures 3.4 through 3.8. The node count, *n*, and stretching ratio, *r*, is included for selected characteristic lines. The far-

field grid image for the *Fine Unresolved BL* grid is omitted because it is very similar to the *Fine Resolved BL* grid. The grids are designed for optimal use at a five degree angle of attack; that is, the high resolution grid section captures the wake at $\alpha = 5°$.

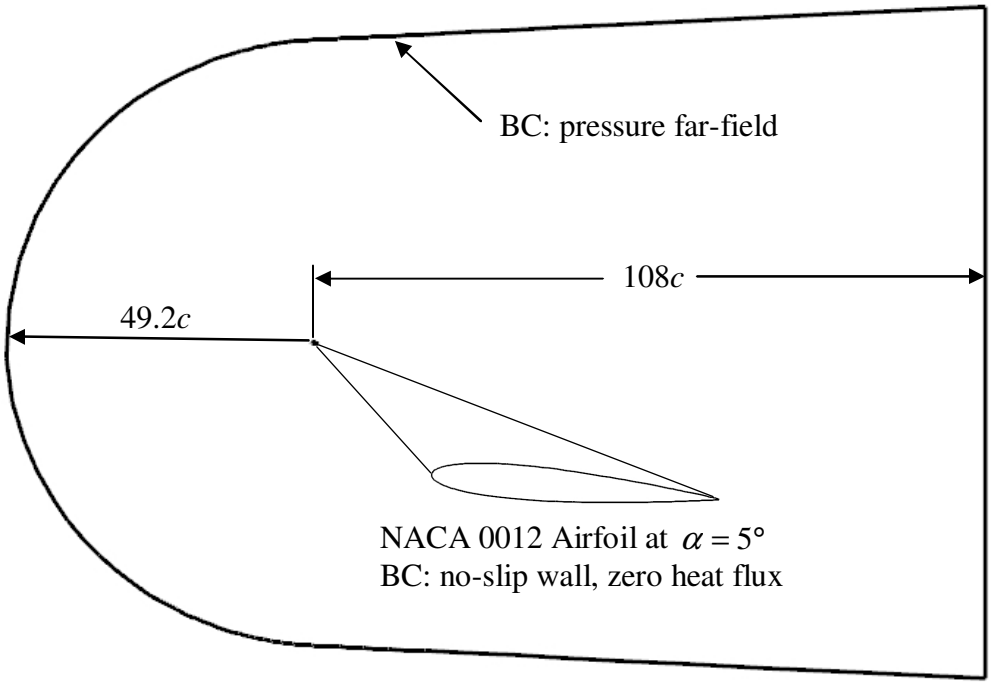

Figure 3.4 Computational Domain

Coarse Grid

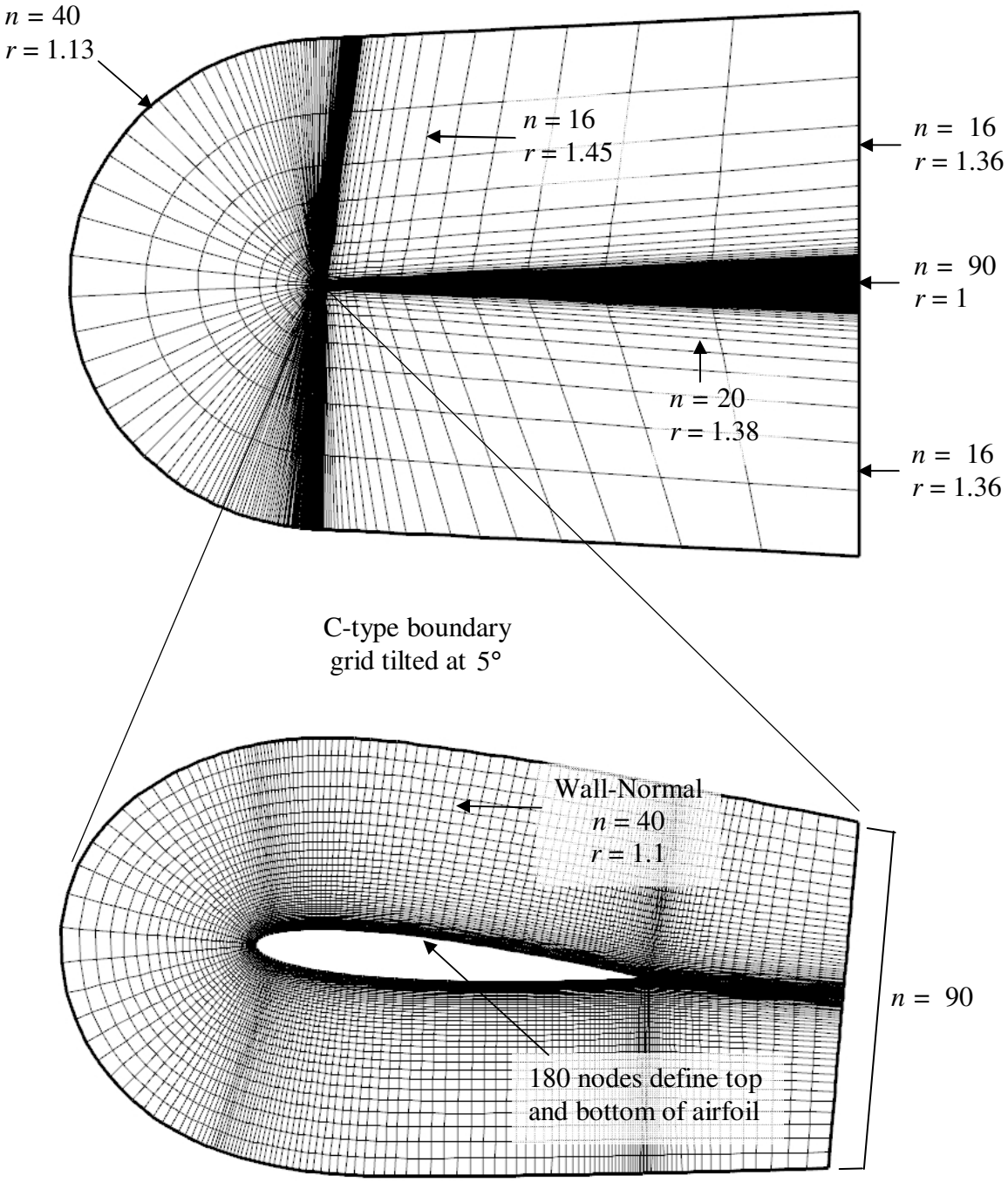

Figure 3.5 Coarse Mesh Grid Description

Fine Grid

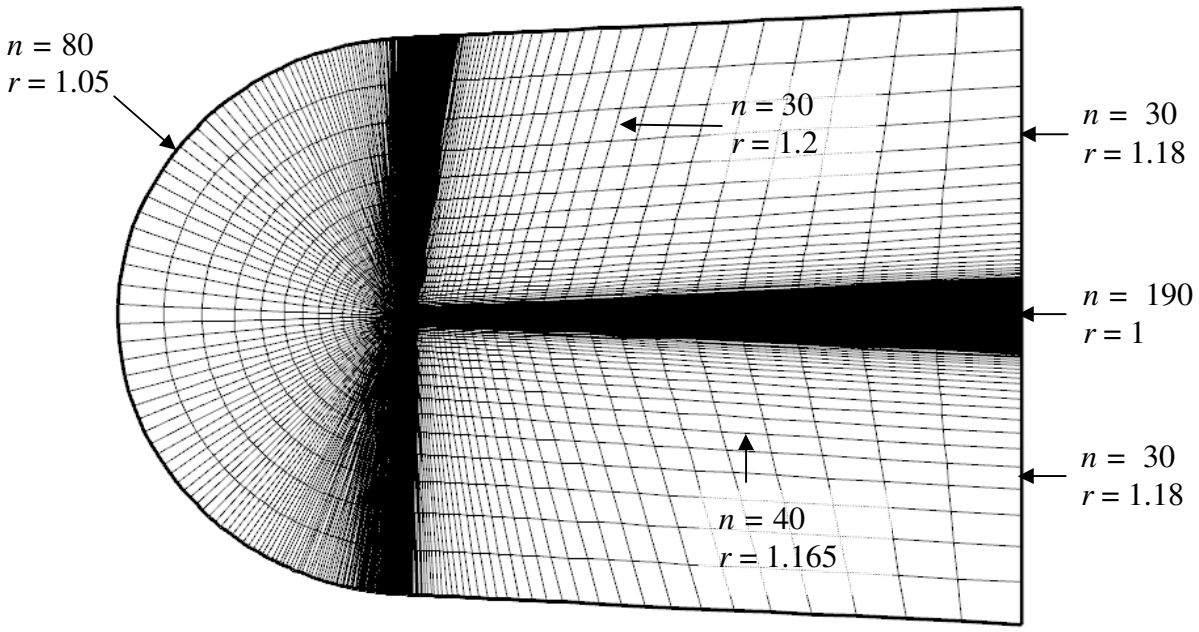

Figure 3.6 Fine Grid Far-Field

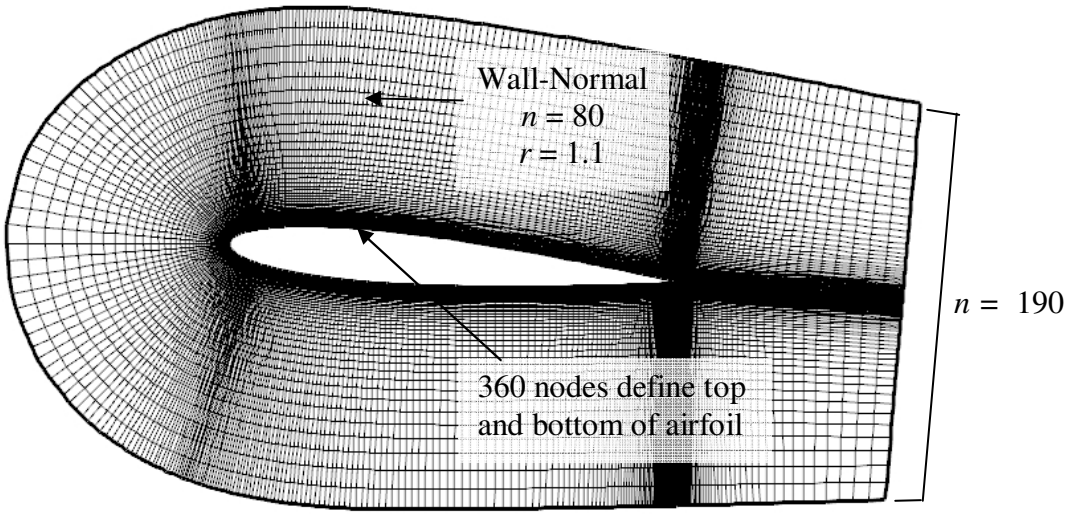

Figure 3.7 Fine Resolved Boundary Layer Grid

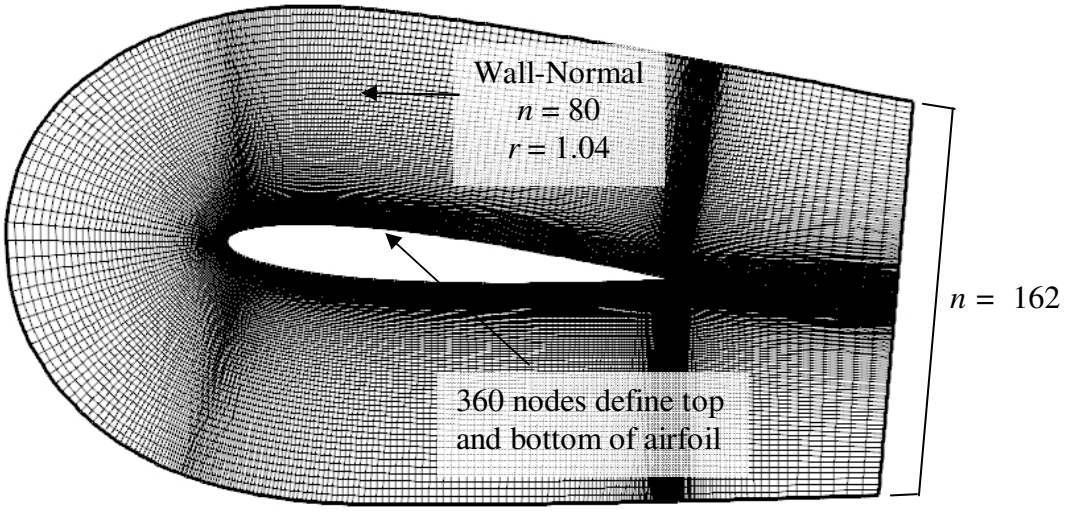

Figure 3.8 Fine Unresolved Boundary Layer Grid

Computational cost savings from using wall functions is minimal. As Spalart points out, the use of wall functions might reduce the wall normal node count by "12 layers or so" [31]. If 360 nodes are used to define the wall, than there is a total element reduction of $360 \times 12 = 4320$, or about seven percent of the total grid. The *real* benefit of using wall functions can be summarized in Table 3.1. With roughly the same number of total elements, the wall normal stretching ratio can be reduced from 1.1 to 1.04 and the maximum BL cell aspect ratio is reduced from 790 to 15. High aspect ratio cells can be introduce numerical difficulties, so the usefulness of wall functions goes far beyond the seven percent computational savings.

3.6: Code Settings

In this section the various CFD code settings and options are summarized. A steady state, pressure based solver is used. A node based Green-Gauss method is used to calculate gradients. Air properties are summarized in Table 3.2. Boundary conditions are summarized in Table 3.3. Different discretization schemes are used depending on the turbulence model. They are summarized in Table 3.4. In 2D simulations, the modification to the SA model is almost completely passive. That is to say, both SA model versions yielded nearly identical solutions. Therefore, only data from the original

SA model is presented. Because of the non-linearity in the governing equations up-winding differencing schemes are more stable. For the FRSM simulations all turbulence transport equations were discretized with the 2nd order up-wind scheme. Even though the 3rd order MUSCL scheme is up-wind biased, the 2nd order scheme is more stable and sometimes necessary for solution convergence. Pressure-velocity coupling is performed with FLUENT's SimpleC scheme, unless the boundary layer is resolved, in which case they are coupled. When the boundary layer is resolved, FLUENT's *enhanced wall treatment* is used. See the FLUENT manual [39] for more information.

Table 3.2 Air Properties

Density, ρ	Ideal gas law, $\rho_\infty = 1.225 kg/m^3$
Specific heat, c_p	$1006.43\, J/kg-K$
Thermal Conductivity, k	$0.0242 w/m-K$
Viscosity, μ	$1.7894\times10^{-5}\, kg/m-s$
Molecular weight, MW	$28.966 kg/kgmol$

Table 3.3 Boundary Conditions

Pressure far-field	$p_\infty = 101325 Pa$ (or $p_{guage} = 0$) $\vec{U}_\infty =$ constant (depends on Re and angle of attack) $T_\infty = 300k$ $k = 1 m^2/s^2$ $\varepsilon = 1 m^2/s^3$ OR $\nu_T = 0.001 m^2/s$ (depends on turbulence model)
Wall	$\vec{U}_\infty = 0$ (no-slip condition) Roughness Constant = 0.5 Heat flux = 0

Table 3.4 Differencing Schemes

with SA original model	Pressure	Standard
	Density	3rd order MUSCL
	Momentum	3rd order MUSCL
	ν_T	3rd order MUSCL
	Energy	3rd order MUSCL
with FRSM	Pressure	Standard
	Density	3rd order MUSCL
	Momentum	3rd order MUSCL
	ε	2nd order upwind
	Reynolds stresses (all 6)	2nd order upwind
	Energy	3rd order MUSCL

3.7: Results

The results section is divided into three sections: gross quantities, wall function analysis, and a brief Reynolds stress analysis.

3.7.1: Gross Quantities

Lift and drag plots as a function of AOA are shown for $\mathrm{Re} = 2M$, even though the grid was generated for $\mathrm{Re} = 530000$ (in consideration for finite wing simulations). Figures 3.9 and 3.10 include lift and drag data up to predicted stall, respectively. Experimental data is from Sandia National Laboratories [50]. These figures confirm that the steady RANS simulations, regardless of grid or modeling, cannot accurately predict stall. The reason is that the turbulence models are "reluctant" to predict flow separation. The use of the FRSM is no remedy. Unsteady effects exist near stall (and certainly beyond) from vortex shedding. Several unsteady RANS simulations were performed but, because the grid was designed for $\alpha = 5°$, gross quantities were the same as the steady state simulations and are not included. The high density grid region does not capture the wake at high AOA. In the figure legends "R-BL" means *resolved* boundary layer and "U-BL" is *unresolved* boundary layer.

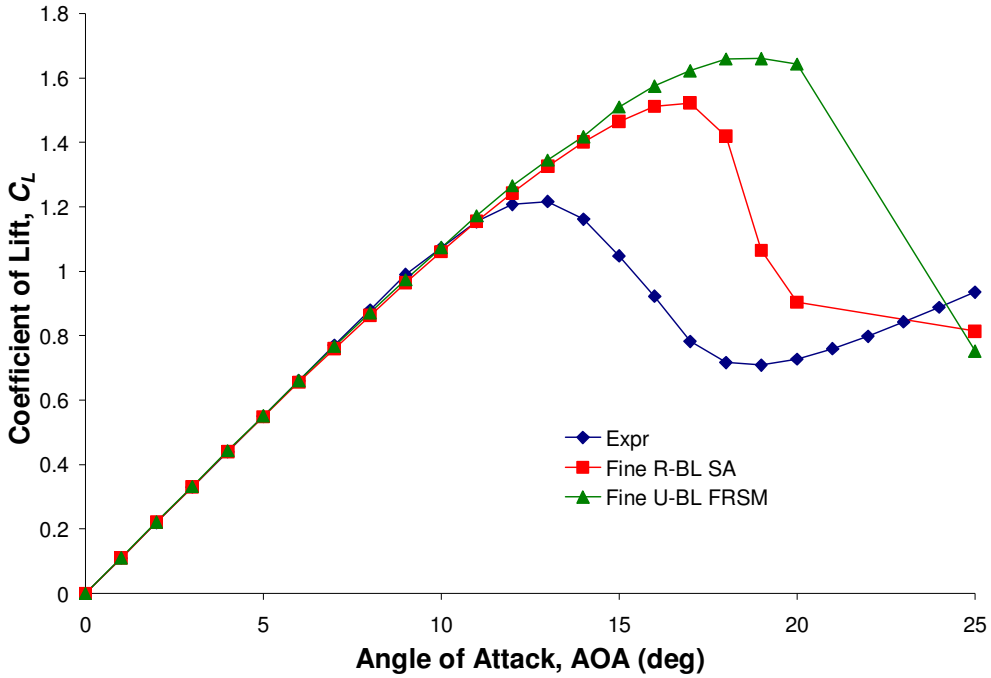

Figure 3.9 Lift Comparison up to Predicted Stall.

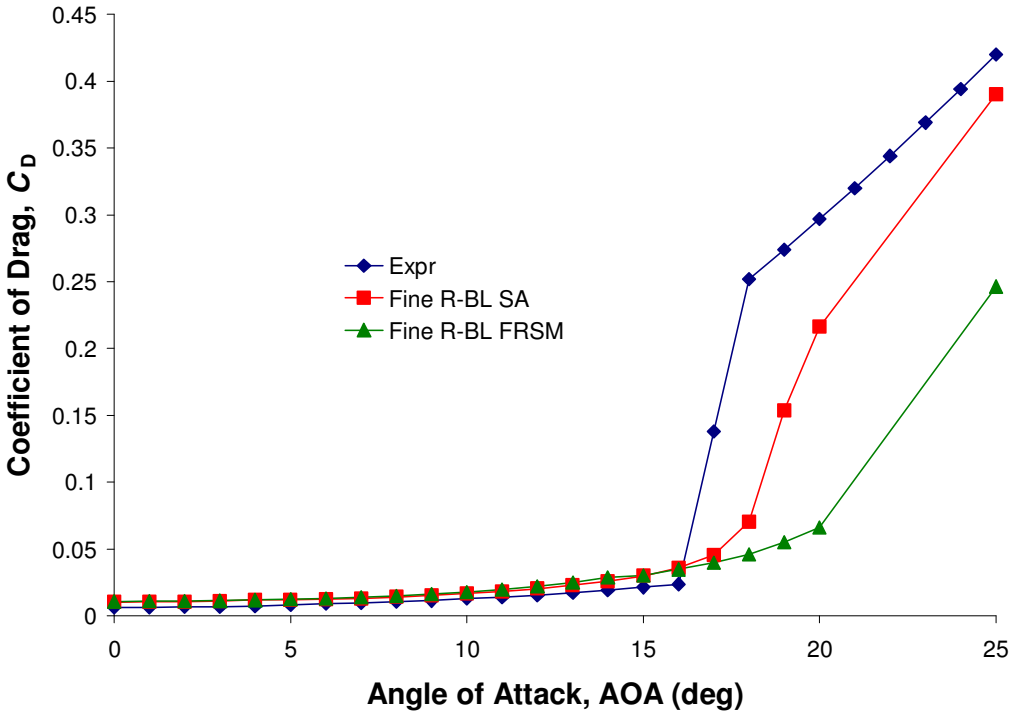

Figure 3.10 Drag Comparison up to Predicted Stall

The plots indicate that the RANS simulations are completely inadequate near stall. Therefore the plots of Figures 3.9 and 3.10 are reproduced at low AOA, see Figures 3.11 and 3.12. It is easy to tell that all simulations and turbulence models predict lift very well. Best accuracy is obtained at the lowest AOA, perhaps $\alpha \leq 5°$. In general, the less flow separation, the better the results. Qualitatively, all simulations predict the correct drag features but there exists a baseline shift of about 50%. It is possible that the wall roughness constant should be changed from 0.5 (the default value recommended for aerospace flows).

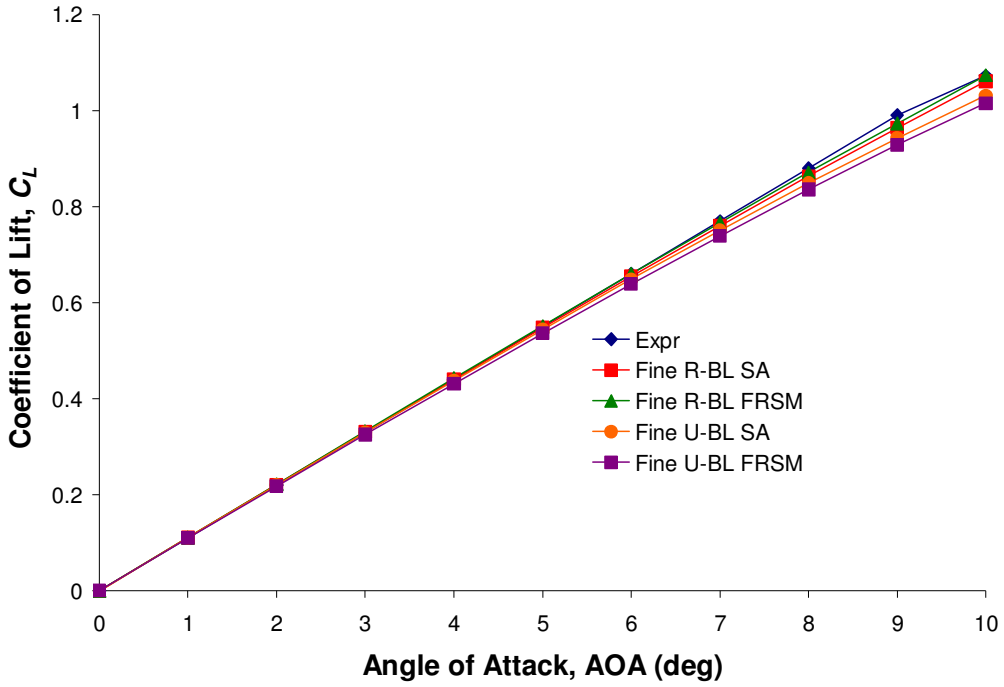

Figure 3.11 Before Stall Lift Comparison

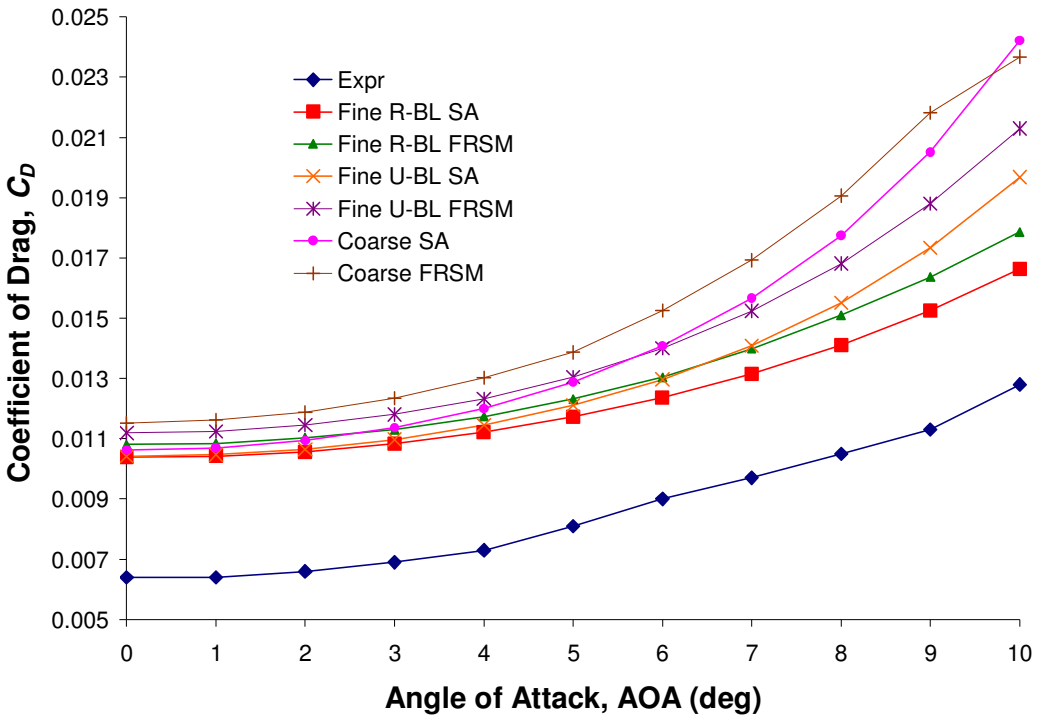

Figure 3.12 Before Stall Drag Comparison

All simulations predict nearly identical pressure distributions. This is illustrated in Figure 3.13 for $\mathrm{Re} = 530000$. The Fine R-BL FRSM simulation is compared with the Coarse SA. These simulations feature different grid counts, wall function treatments, and turbulence models; but, the pressure distribution remains independent. To properly compare the use of wall functions another flow parameter should be used.

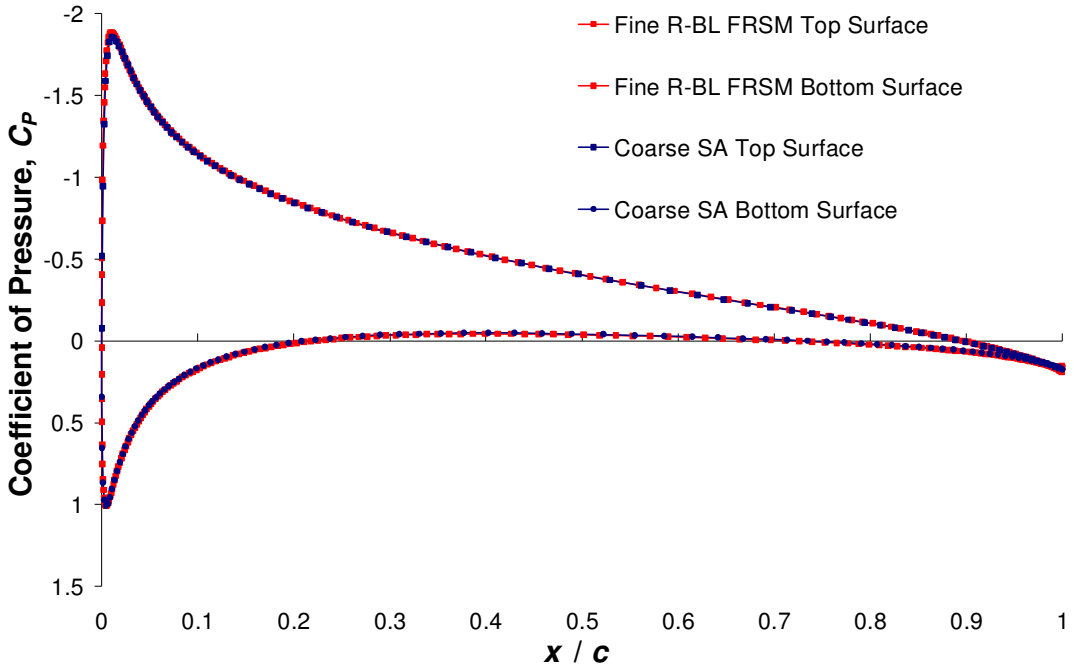

Figure 3.13 Pressure Distribution Comparison

3.7.2: Wall Function Comparison

It was noted in the above section that another flow parameter is required to properly quantify the penalty that may exist in using wall functions. Wall shear stress is the best choice because it requires accurate information of the high-gradient, near-wall velocity field.

Wall shear stress: $$\tau_w = \mu\left(\frac{\partial u}{\partial y}\right)_{y=0} \tag{3.10}$$

Skin friction coefficient: $$C_f = \frac{\tau_w}{\frac{1}{2}\rho_\infty U_\infty^{\,2}} \tag{3.11}$$

Based on the near-wall velocity field comparison shown in Figure 3.14, it would appear that the unresolved boundary layer cannot stand a chance at accurate prediction of the velocity gradient.

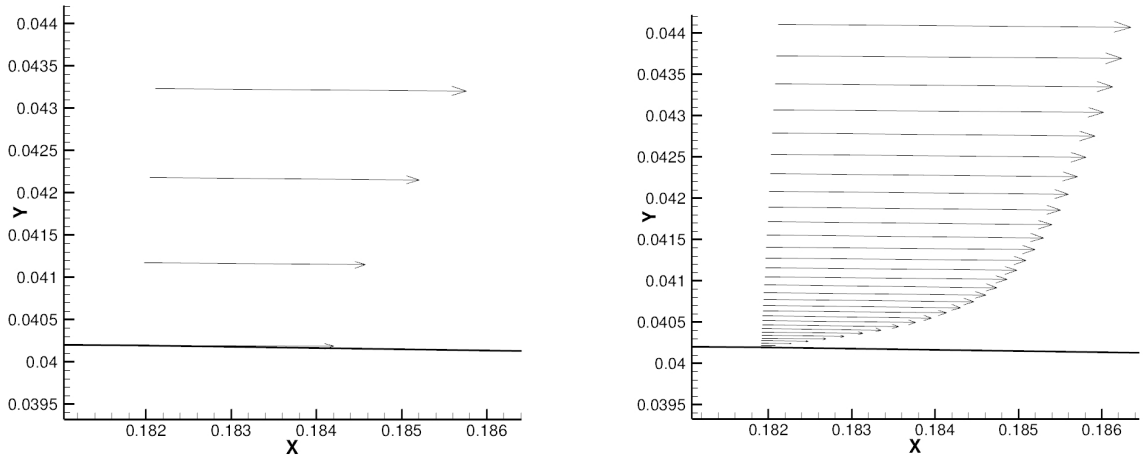

a) Unresolved velocity field *b) Resolved velocity field*

Figure 3.14 Near-Wall Velocity Field Comparison

Figure 3.15 shows the wall shear stress results. For fair comparison, both simulations use the fine grid, FRSM, $\alpha = 5°$, and $\mathrm{Re} = 530000$. The only difference is use of wall functions. Excellent agreement is shown for the trailing edge half of the airfoil ($x/c \geq 0.5$). This is because of mild velocity gradient in this region. Also, the flatness of the trailing edge half of the airfoil probably improves the accuracy of wall functions. Discrepancies exist in the leading edge half of the airfoil ($x/c \leq 0.5$). The wall functions miss the peak wall shear stress near the leading edge and then continue to over-predict it, a common observation in any modeling approximation. The leading edge is more difficult for wall functions because of higher velocity gradient and airfoil curvature. For the highest fidelity solution, wall functions should be avoided; otherwise, their predictions are not far off and they greatly alleviate the challenge of gridding a fully resolved boundary layer.

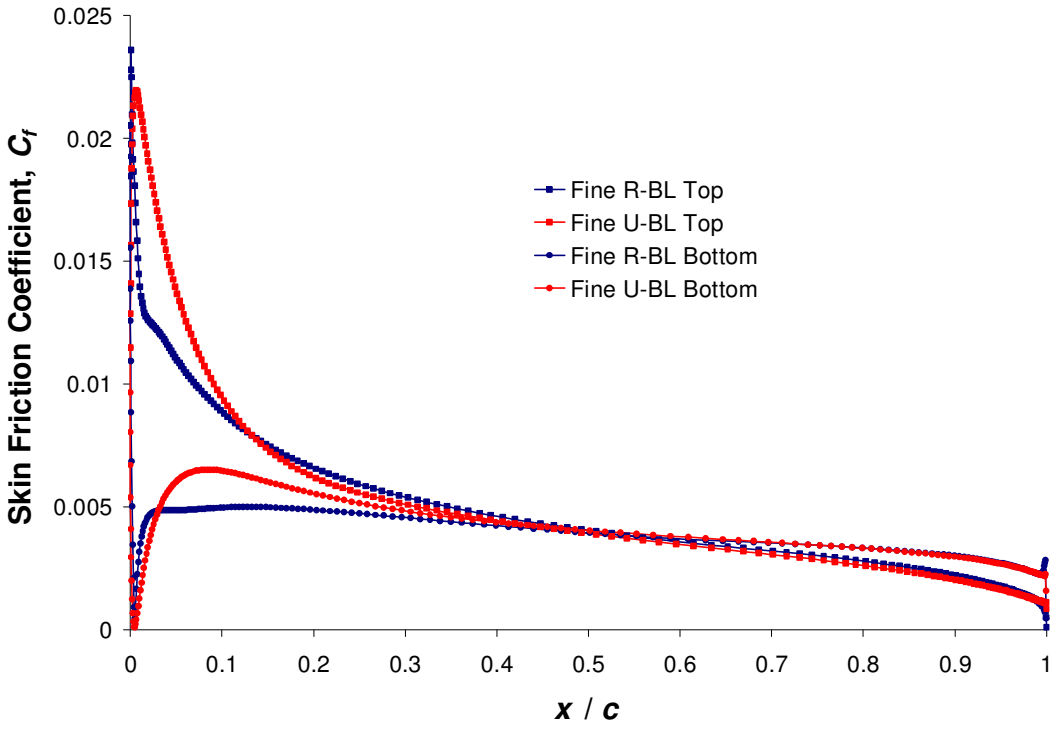

Figure 3.15 Skin Friction Coefficient Comparison with and with out Wall Functions

3.7.3: Analyzing the Wake with Reynolds Stresses

One of the advantages FRSMs is that the Reynolds stresses can be analyzed very easily. Figure 3.16 shows a contour plot of the $\overline{u'v'}$ Reynolds stress component. This is a useful parameter to discern the contribution of the top and bottom boundary layers to the total wake. The top boundary layer $\overline{u'v'}$ stresses take negative values and the bottom boundary layer takes positive. When moving in the positive y direction, the u velocity component introduces a turbulent moment surplus (positive value) to the bottom boundary layer, and a deficit (negative value) to the top boundary layer. This is an artifact of the coordinate system and the gradient direction. The velocity field in the trailing edge region, Figure 3.17, clarifies this.

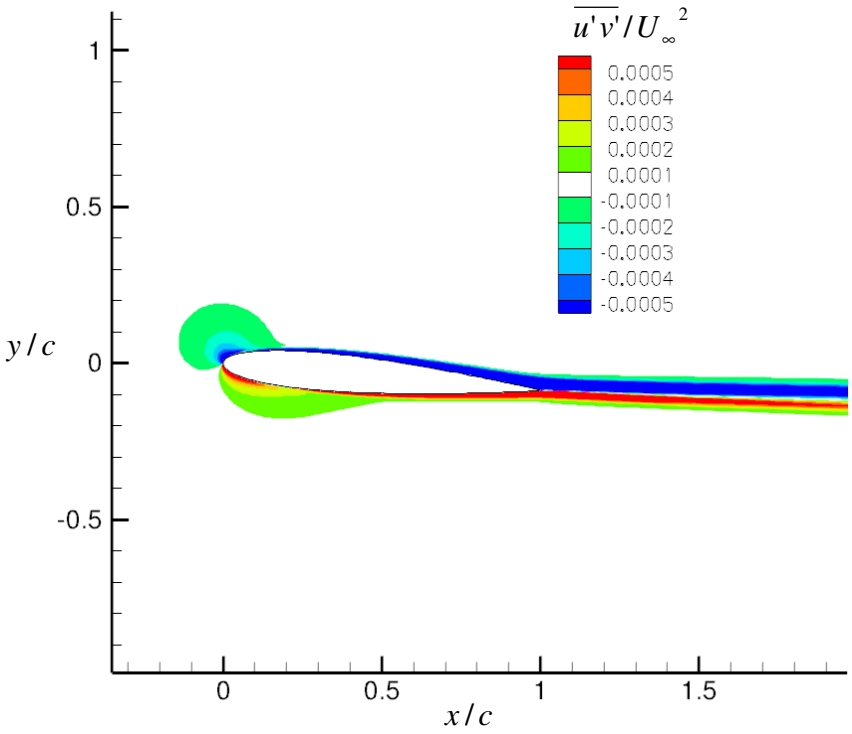

Figure 3.16 uv Reynolds Stress Component

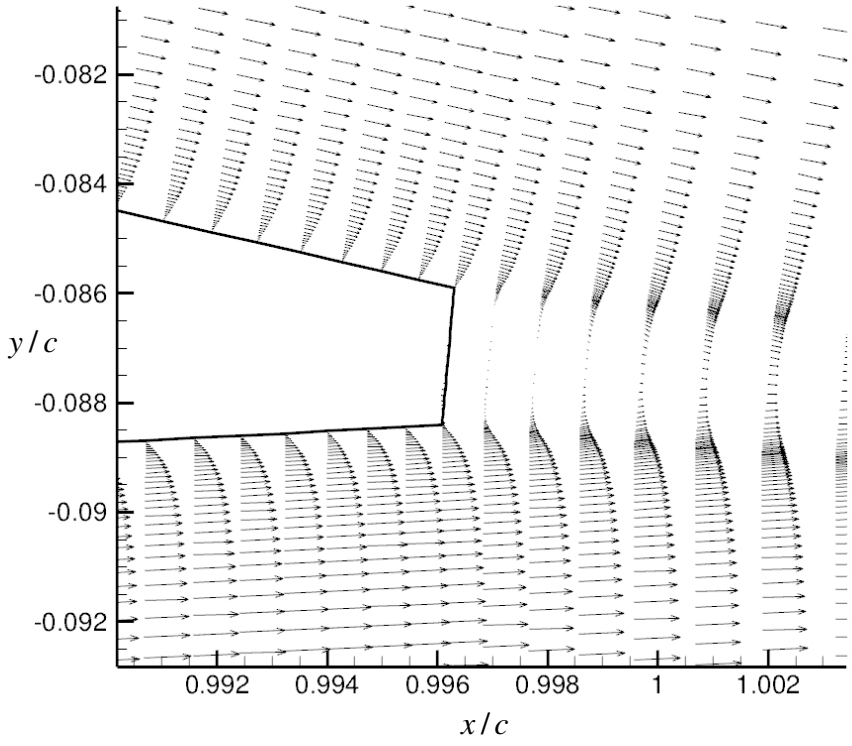

Figure 3.17 Velocity Vectors in the Wake

3.8: Conclusions

There were several conclusions in this chapter. More evidence is provided that RANS simulations (regardless of turbulence model) cannot predict—or at least show difficulty in predicting—near stall flow features. If attention is kept in the realm of attached flow, than both the SA model and FRSM were found to give very similar results. There is little use for a complex turbulence model in the 2D simulations contained in this chapter, unless Reynolds stresses are being calculated. Pertaining to wall functions, their use should be avoided if the highest fidelity solution is sought after; otherwise, their predictions are not far off and they greatly alleviate the challenge of gridding a fully resolved boundary layer.

Chapter 4 Finite Wing Simulation

This chapter addresses the simulation of a finite span wing, which is a 3D flow-field. Computationally, 3D is far more demanding than 2D. The governing equations feature increased complexity. An extra transport equation must be solved for the third velocity component. For the FRSM, two extra transport equations are solved for $\overline{u'w'}$ and $\overline{v'w'}$.

Physically, 3D fixed wing flows are much more interesting. There exists uneven spanwise pressure loading and tip vortex formation. The tip vortices entrain much of the turbulent wake behind the wing and evolve downstream. Their existence and persistence is a crucial element of lifting line theory: that the total circulation of the tip vortex is equal (for potential flow) to the bound circulation over the wing, which is proportional to lift. Their salient features are high swirl velocities [10], low vortex core pressures [9], their contribution to induced drag [11], axial velocity deficits with respect to the surrounding flow [12], and persistence [13-15]. Tip vortices are an example of a coherent turbulent structure [9] and can pose interesting difficulties for a turbulence model.

The main purpose of chapter 4 is to quantify the effects of turbulence modeling with regard to Spalart's challenge two: transfer of momentum after separation [8]. The grid considerations, boundary layer requirements, wall function usage, and CFD settings from chapter three all extend to three dimensions. Only the differences that are unique to 3D simulations will be highlighted.

4.1: Geometry of the Finite Wing

The full finite wing model uses the NACA 0012 airfoil geometry and has a rectangular planform and blunt tip. Only an isolated wing is simulated (no fuselage or tail). The computational domain takes advantage of spanwise symmetry. The half wing span is $b/2 = 0.879m$ and the chord is $c = 0.203m$. Angle of Attack is $\alpha = 5°$ and the chord based Reynolds number is $\mathrm{Re} = 530000$. These conditions correspond to experimental setup tested by Devenport et al [15]. Because of the symmetry, only one tip vortex is actually resolved. The aspect ratio of the wing is $AR = 8.66$, which is high

enough to neglect the vortex pair crow instability. The freestream velocity is $U_\infty = 38.1 m/s$ in the positive *x*-direction.

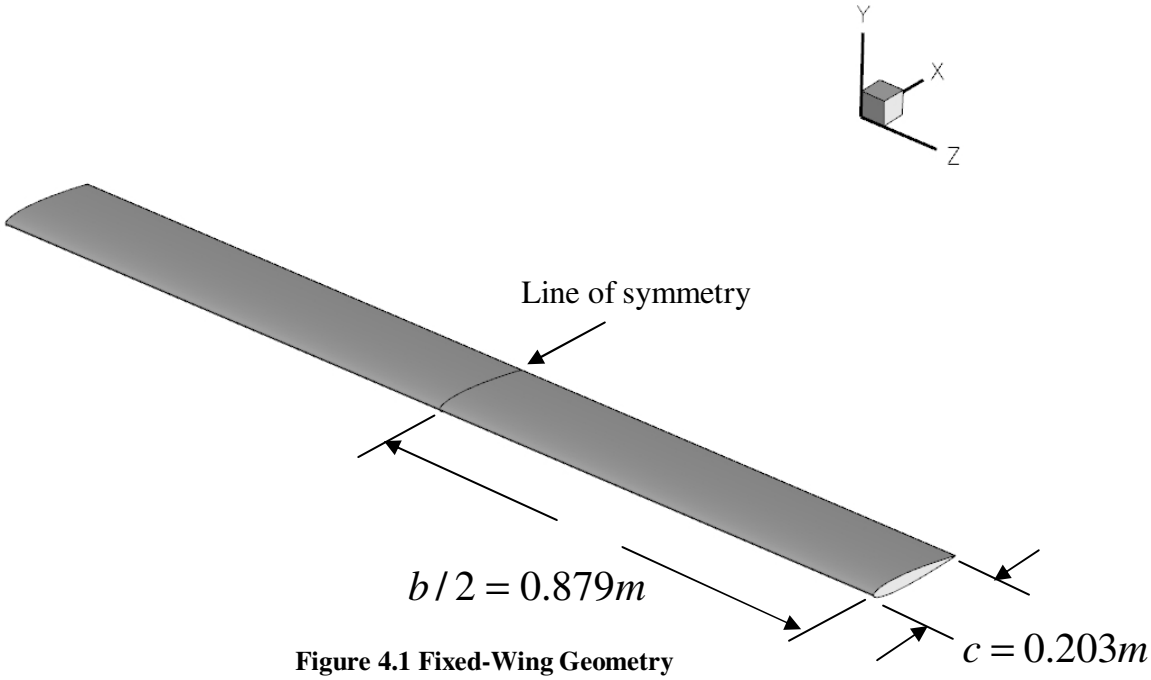

Figure 4.1 Fixed-Wing Geometry

4.2: Computational Domain and Boundary Conditions

A schematic of the computational domain is shown in Figure 4.2. The width in the spanwise, *z,* direction is 3.516*m*, or four half-wing spans. The boundary conditions on the domain are all pressure far-field except the shaded plane, which uses symmetry condition. The wing surface utilizes the no-slip wall condition.

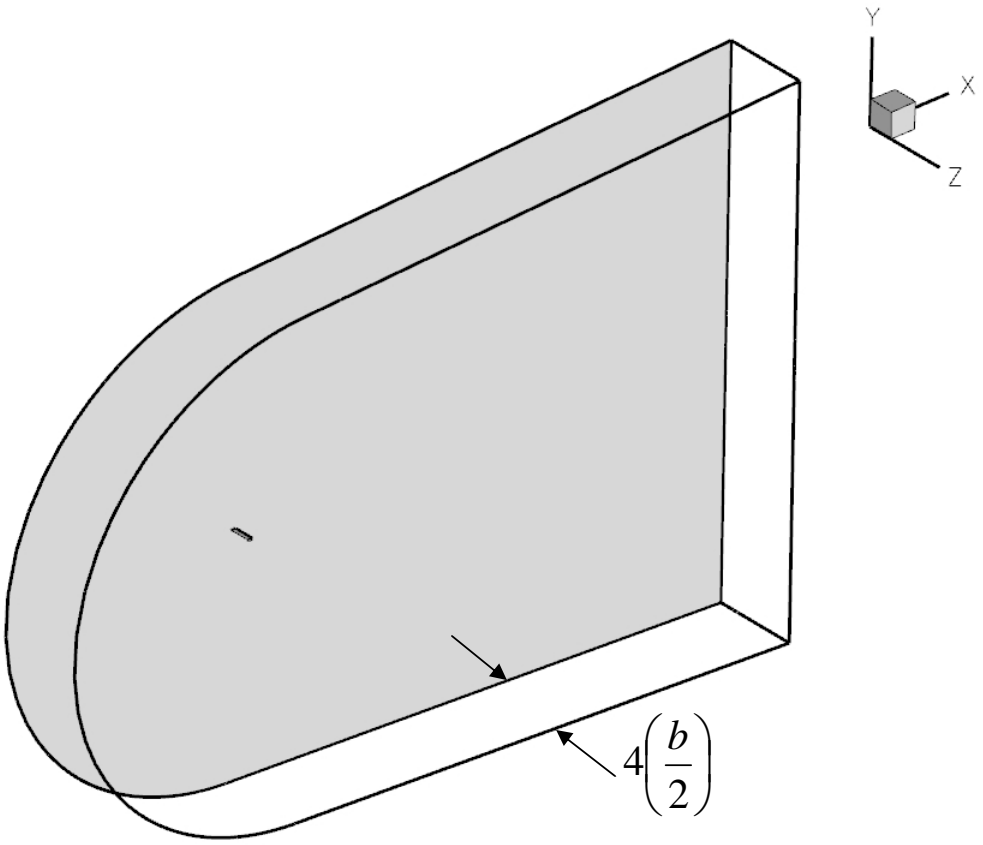

Figure 4.2 Computational Domain

4.3: Grid

The 3D grids were created in GAMBIT by extracting 2D *x*-y cross section grids (from chapter three) in the spanwise, *z,* direction. Three different *x-y* cross section grids were used in the 2D analysis, but only two of them were successful for 3D simulations when using the FRSM. The Fine R-BL grid section (that resolved the boundary layer) posed numerical difficulty with the FRSM and is not included in this analysis. The two successful 3D fixed wing grids are summarized in Table 4.1.

Table 4.1 Grid Summary

Grid name	Element count	*x-y* cross-section element count	Wall function use	Highest aspect ratio element in BL	Wall-normal stretching ratio, *r*
Fine	11.9M	58248 (Fine U-BL)	Yes	15	1.04
Coarse	1.46M	15204 (Coarse)	Yes	30	1.1

An important grid feature that must be accounted for in 3D is meshing the wing tip region. This is the only part of the grid that features un-structured elements. Care needs to be taken when gridding this region. The tip mesh region for the fine and coarse grids is shown in Figure 4.3 and Figure 4.4 respectively, and also Figure 4.5. The fine grid features two different spanwise stretching ratios to resolve the vortex in a nearly square mesh cross-section (see Figure 4.8).

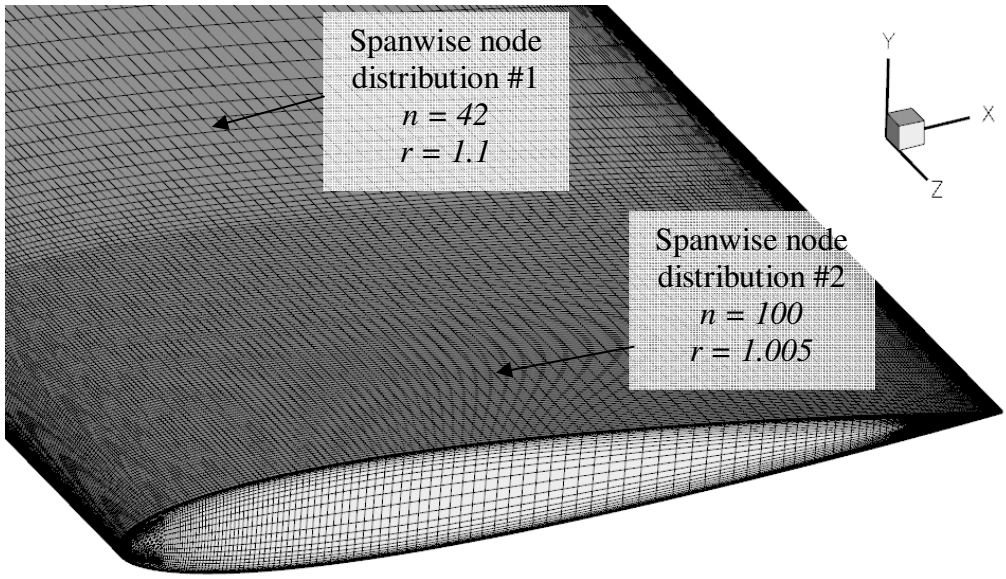

Figure 4.3 Fine Grid Tip Mesh

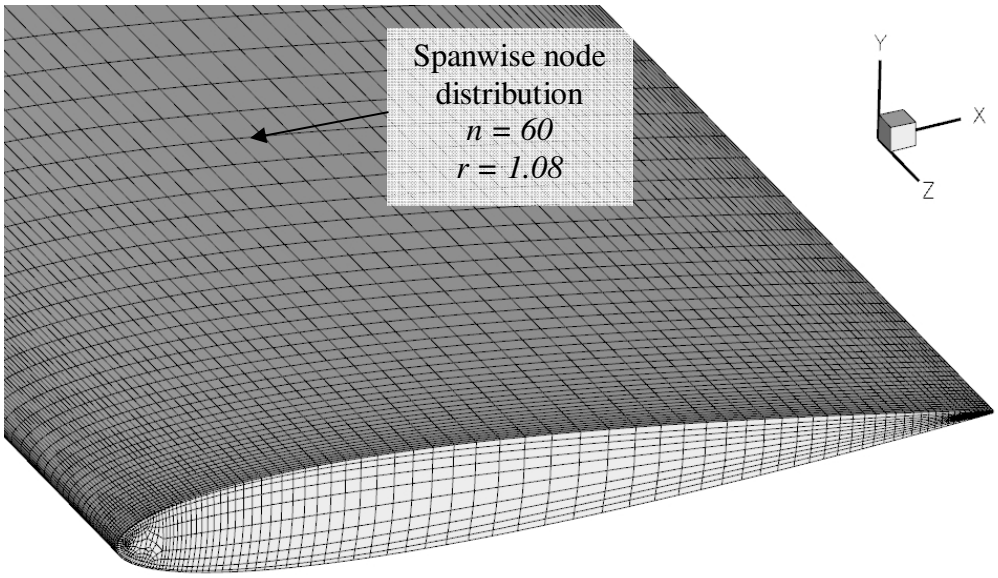

Figure 4.4 Coarse Grid Tip Mesh

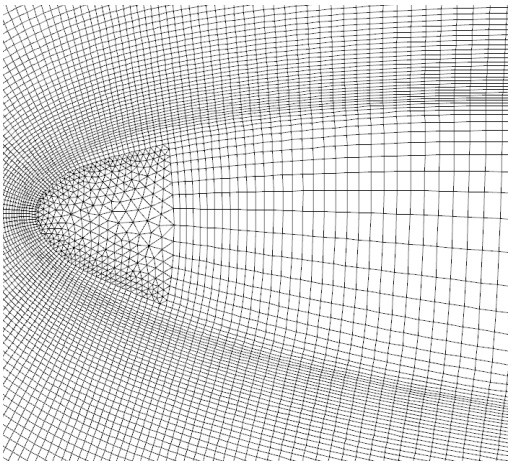

a) fine grid front

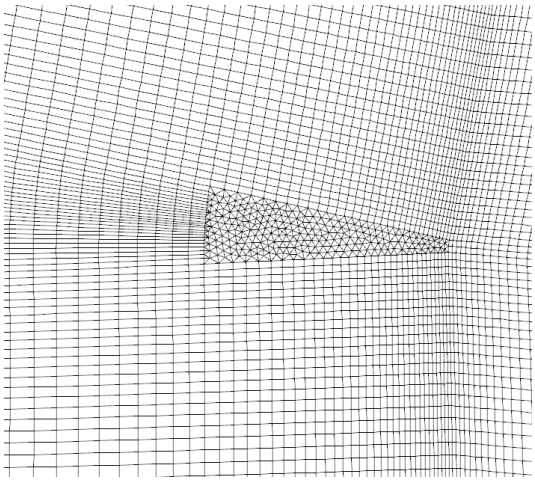

b) fine grid rear

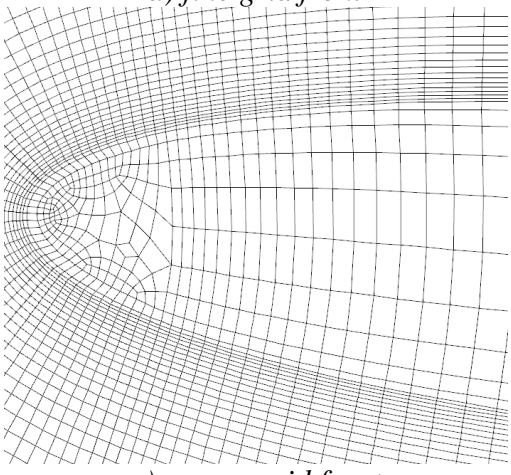

c) coarse grid front

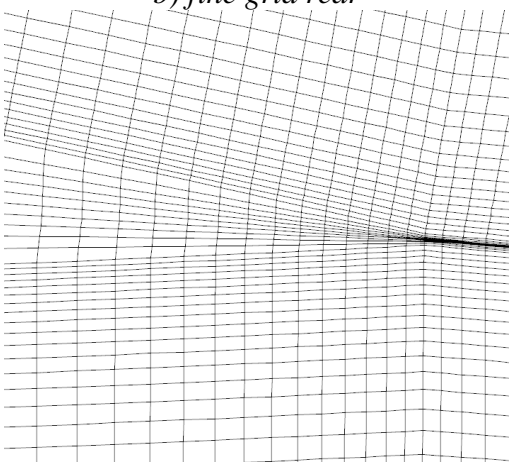

d) coarse grid rear

Figure 4.5 Fine and Coarse Grid Wing Cap Mesh Comparison

4.4: Results

Results in this chapter are divided into five sections: gross quantities, mean vortex velocity profiles, Reynolds stress—mean strain rate anisotropy, predicting a laminar vortex core, and near-field vortex roll-up analysis.

4.4.1: Gross Quantities and Grid Independence

Lift, drag, and pitching moment coefficients for all simulations are summarized in Table 4.2. For both versions of the SA model the difference in lift prediction for fine and coarse grids is just over one percent. Grid effects are more pronounced with FRSM simulations. This is strong evidence that complex models require higher grid resolution and / or higher order differencing schemes. Based on Table 4.2, one might conclude that solutions are nearly grid independent if the SA model is used. If the FRSM is used, the solutions are not independent of the grid. Large discrepancies exist in all simulations for the pitching moment coefficient, which is taken about quarter chord. It is a *very* sensitive quantity, particularly when taken about quarter chord. The difference percentages should not be given as much weight as lift or drag.

Table 4.2 Gross Quantities

Turbulence model	Grid	Lift coefficient	Difference, percentage	Drag coefficient	Difference, percentage	Pitching moment coefficient	Difference, percentage
FRSM	Fine	0.400	4.00	0.0214	15.0	0.00648	40.9
	Coarse	0.384		0.0246		0.00913	
SA w / Correction	Fine	0.408	1.47	0.0188	6.4	0.00533	36.0
	Coarse	0.414		0.0200		0.00341	
SA Original	Fine	0.409	1.22	0.0189	6.3	0.00523	35.9
	Coarse	0.414		0.0201		0.00335	

Pressure coefficient and skin friction coefficient contour plots are shown in Figure 4.6 and Figure 4.7, respectively for fine grid simulations. The wing is mirror-imaged along the line of symmetry. The SA simulation (w/ correction) is on the left and the FRSM simulation is on the right. Just like the 2D results from Chapter 3, there is very little

difference in the pressure distribution. The FRSM simulation predicts higher skin friction at all locations on the wing, consistent with the slightly higher drag prediction.

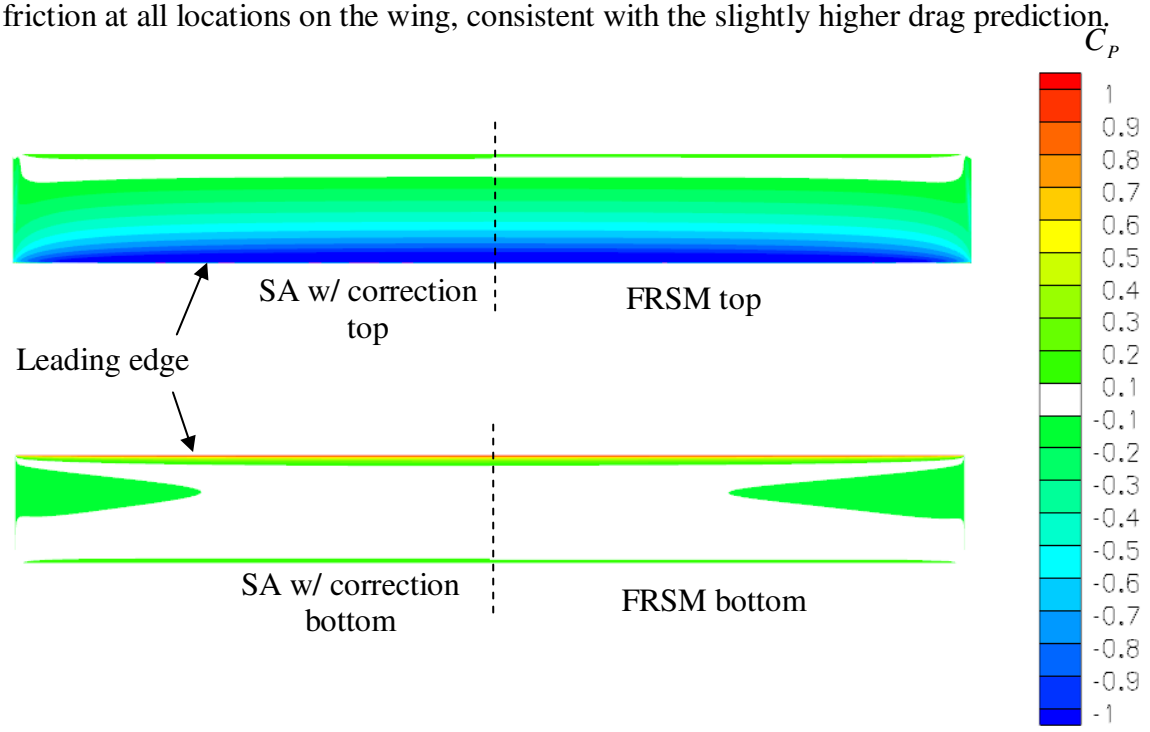

Figure 4.6 Pressure Coefficient Comparison on Top and Bottom of Wing

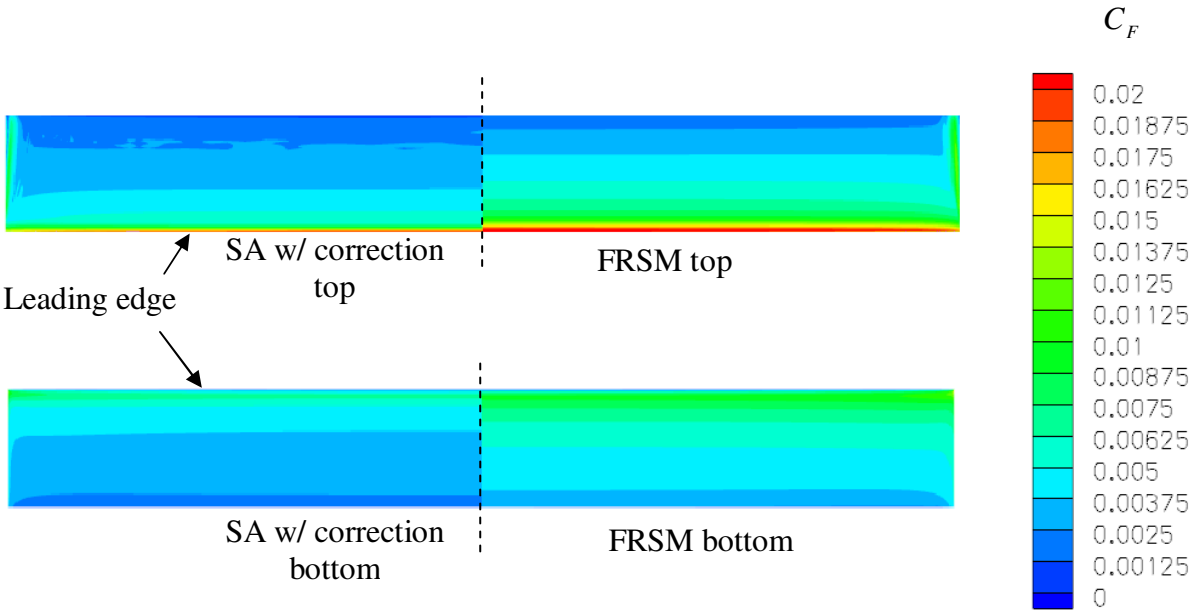

Figure 4.7 Skin Friction Coefficient Comparison on Top and Bottom of Wing

4.4.2: Mean Vortex Velocity Profiles

One of the simplest ways to quantify a vortex is by examining the mean velocity profiles. Comparing with experimental results is a necessary accuracy check for computational simulations. In this section the computational simulations are compared to wind tunnel tests performed by Devenport et al. [15]. Their experimental measurements were taken with a low intrusive four-sensor hot-wire probe calibrated for velocity and angle response. Most wind tunnel measurements in the past are plagued with effects of induced fluctuations from "vortex wandering", an artifact of the wind tunnel and not flow geometry. Devenport et al. developed a theory to quantify the uncertainty of wandering and suggested a scheme to correct velocities for it. The profile comparisons are made with uncorrected velocities at 5*c* and 10*c* downstream (of the trailing edge) stations. The computational *y* and *z* axes are different from the experimental axes. The transformation matrix is:

$$a_{ij} = \begin{bmatrix} 1 & 0 & 0 \\ 0 & 0 & 1 \\ 0 & -1 & 0 \end{bmatrix} \tag{4.1}$$

Experimental velocity component uncertainties are $\frac{\Delta u_i}{U_\infty} = 0.015$ (or about five percent of the peak swirl velocity) and r.m.s. amplitudes due to wandering (in the experimental) *y* and *z* directions are $\sigma_y / c = \sigma_z / c = 0.004$ at 5*c*, and $\sigma_y / c = 0.007$, $\sigma_z / c = 0.005$ at 10*c*. The effects of wandering increase with downstream distance. For the needs of the present comparison, wandering is considered negligible.

Both computational and experimental profile velocities are resolved in core aligned coordinate systems parallel to the vertical axis. This accounts for a small inward "drift" in the spanwise direction. For the computational profiles, a linear interpolation of vortex center location 1*c* up and downstream of the station is used to calculate the drift angle. For example, to fine the drift angle at $x = 5c$, the vortex center is identified at $x = 4c$ and $x = 6c$. The vortex center is identified with the point of maximum helicity ($u_i \omega_i$) (information on a more elaborate scheme for vortex identification is included in Appendix A). The angle about the *y*-axis is then:

$$\theta = \tan^{-1}\left[\frac{z_2 - z_1}{x_2 - x_1}\right] \tag{4.2}$$

Where, the vortex center 1*c* upstream is $(x_1, \approx 0, z_1)$ and 1*c* downstream is $(x_2, \approx 0, z_2)$. At the *5c* and 10*c* stations, $\theta = 1°$ and $\theta = 0.56°$, respectively; both slightly lower than experiment. The transformation matrix for resolving velocity components is:

$$a_{ij} = \begin{bmatrix} \cos\theta & 0 & \sin\theta \\ 0 & 1 & 0 \\ -\sin\theta & 0 & \cos\theta \end{bmatrix} \tag{4.3}$$

A summary of vortex core parameters is shown in Table 4.3 including data from Devenport et al [15]. The vortex core radius, *r*, is calculated as the distance from peak-to-peak tangential velocity.

Table 4.3 Vortex Core Parameters

Turbulence Model (or Experiment)	Grid	x/c	Core radius r/c	Peak V_θ/U_∞	Peak Deficit U_D/U_∞
FRSM	fine	5	0.043	0.277	0.168
	coarse	5	0.070	0.195	0.155
SA w/ correction	fine	5	0.081	0.175	0.124
	coarse	5	0.087	0.165	0.095
SA original	fine	5	0.136	0.147	0.063
	coarse	5	0.135	0.149	0.068
FRSM	fine	10	0.068	0.199	0.134
	coarse	10	0.108	0.134	0.086
SA w/ correction	fine	10	0.123	0.175	0.075
	coarse	10	0.142	0.165	0.059
SA original	fine	10	0.205	0.147	0.040
	coarse	10	0.237	0.149	0.043
Experiment	N/A	5	0.036	0.286	0.165
Experiment	N/A	10	0.037	0.286	0.152
Experiment	N/A	15	0.036	0.277	0.141
Experiment	N/A	20	0.039	0.278	0.153
Experiment	N/A	25	0.033	0.275	0.147
Experiment	N/A	30	0.036	0.263	0.160

The computational data is not presented beyond 10*c* because of excessive diffusion. All simulations diffuse the vortex significantly beyond 5*c*; this is revealed by increased core radius and decreased swirl and axial deficit velocities. Even the best simulation (FRSM

fine grid) predicts an increased core radius from 5*c* to 10*c* by 58%, while the experimental data indicates a perfectly consistent vortex. The diffusion is clearly numerical. There is a good deal of literature describing grid and differencing schemes for "acceptable" vortex convection. The conditions can be simplified by considering the number of grid points inside the core (in both spanwise and crosswise directions) and the order of accuracy of the differencing scheme. A summary of previous results is shown in Table 4.4.

Table 4.4 Conditions for Acceptable Vortex Convection

Author(s)	Suggested core grid count	Differencing Scheme
Duraisamy [22]	10	5^{th} order (WENO)
Dacles-Mariani [27]	15 – 20	5^{th} order
Egolf et al. [29]	14	5^{th} order
	7	9^{th} order "for near perfect convection"

The highest differencing scheme available in the FLUENT code is a 3^{rd} order (MUSCL) upwind biased and the number of grid points at 5*c* is 22×16 as shown in Figure 4.8. With only a 3^{rd} order scheme it is unreasonable to expect accurate vortex convection for extended distance. In addition, the *axial* grid count and stretching ratio could likely be improved.

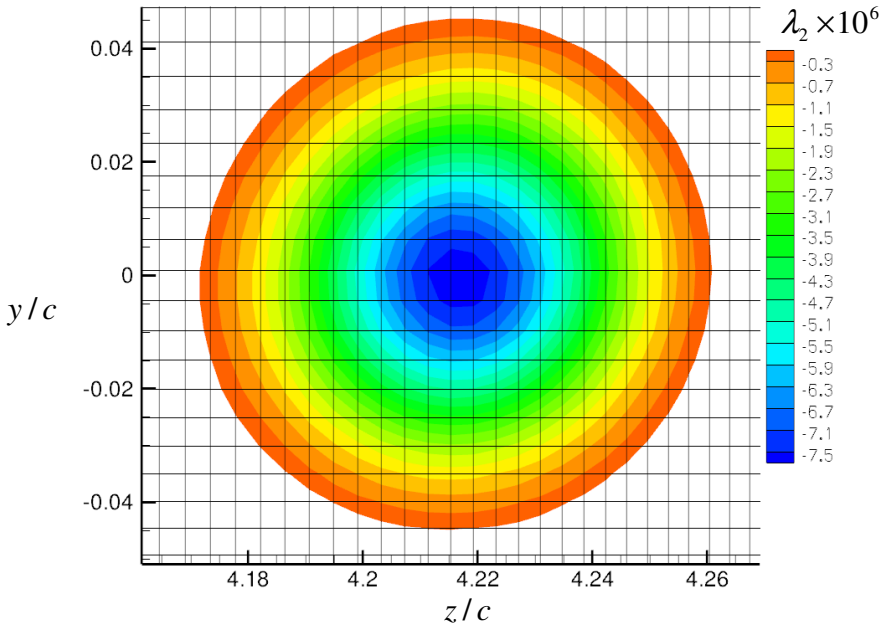

Figure 4.8 Vortex Core Grid Resolution at 5c with Fine Grid (FRSM)

Nonetheless, remarkable agreement is shown for mean velocity profiles at the 5*c* station when using the fine grid with the FRSM. The tangential component is shown in Figure 4.9 and the axial deficit in Figure 4.10. The FRSM fine grid simulation predicts both peak velocity components to within measurement uncertainty! The data also shows a big success for the very simple "ad hoc" [27] correction term, (referred to as SA w/ correction) particularly for predicting the axial velocity deficit. An interesting observation is that the FRSM coarse grid simulation yields better results (with regard to vortex resolution) than the SA models (both versions) on the fine grid, requires less computational resources, less time to convergence, and solves for Reynolds stresses. Unfortunately, the FRSM coarse grid simulation probably has the worse prediction of lift and drag, but this could be calibration issues and might be better resolved with another model for the pressure-strain term.

Mean velocity profile comparisons are also shown for the 10*c* station in Figure 4.11 and 4.12. Again, both fine and coarse grid FRSM simulations "out-perform" the SA model simulations. Figure 4.10 indicates that all simulations predict the location and size of the spiral wake (just above $-y/c = 0.2$). This is because turbulence in the spiral wake is shear dominated and much more isotropic, in the sense that the principal axes of

the Reynolds stress tensor are coincident with the principal axes of the rate-of-strain tensor.

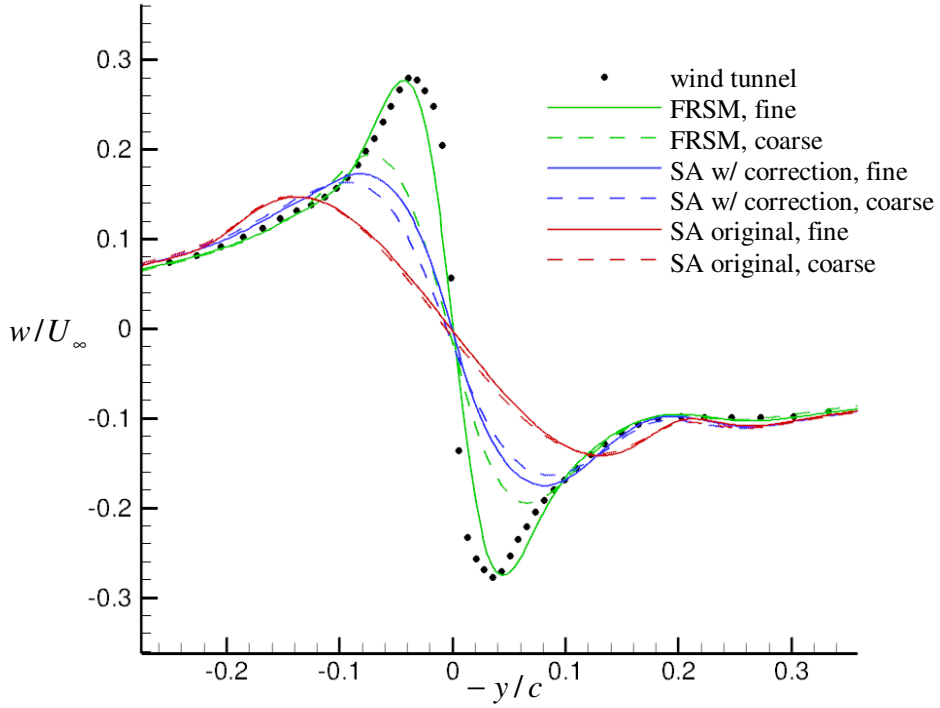

Figure 4.9 Spanwise Velocity Component Comparison at 5c Downstream Station

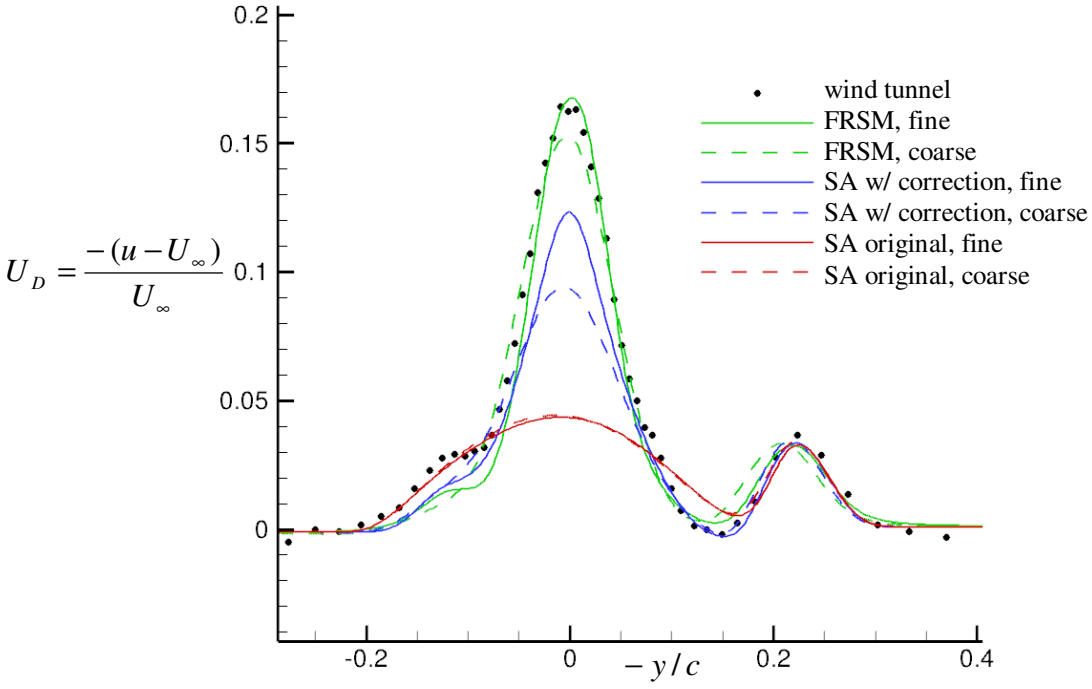

Figure 4.10 Axial Velocity Deficit Comparison at 5c Downstream Station

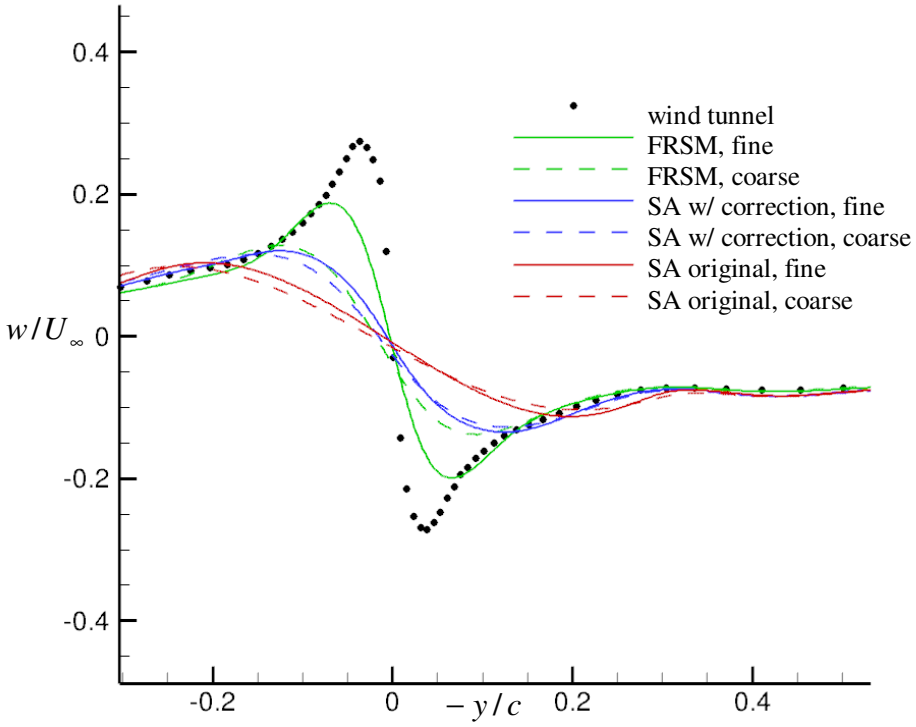

Figure 4.11 Spanwise Velocity Component Comparison at 10c Downstream Station

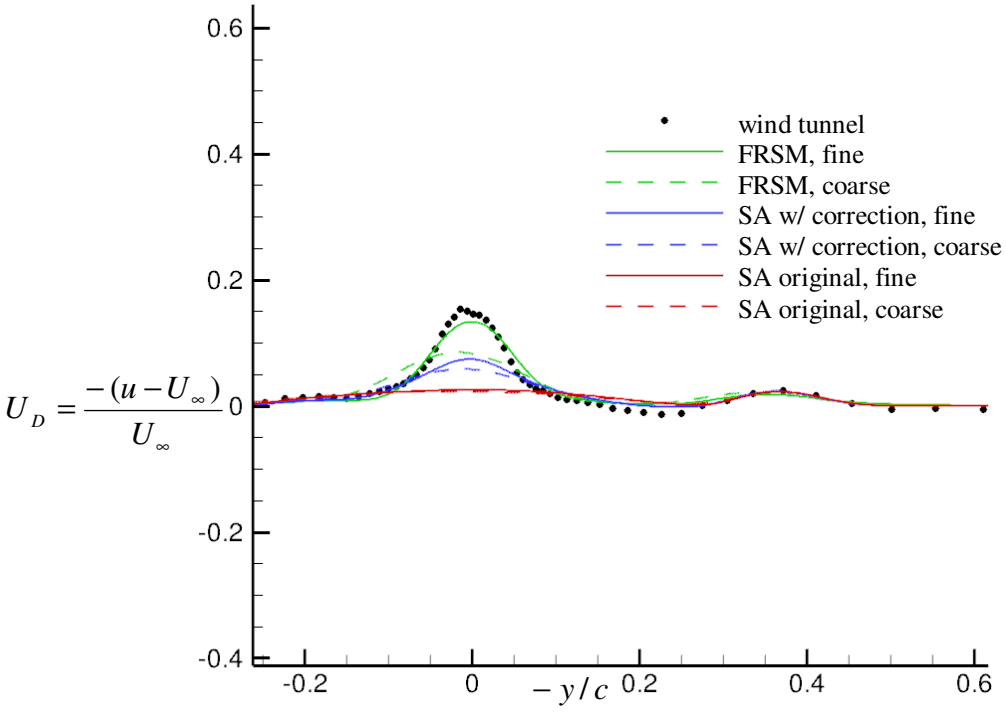

Figure 4.12 Axial Velocity Deficit Comparison at 10c Downstream Station

4.4.3: Reynolds Stress-Mean Strain Rate Anisotropy

The Boussinesq eddy-viscosity model states that turbulent transport of momentum is analogous to molecular transport of momentum, in that, the principal axes of the Reynolds stress tensor are coincident with the principal axes of the rate of strain tensor. For compressible flow (and assuming fluid is isotropic, homogenous, and Stoke's hypothesis applies) the linear constitutive relationship for the Reynolds stress tensor is:

$$\bar{\rho}\tau_{ij} = -\overline{\rho u'_i u'_j} = 2\nu_T s_{ij} - \frac{2}{3}(\nu_T s_{mm})\delta_{ij} \tag{4.4}$$

This relationship follows the same form as the viscous stress tensor, t_{ij}, seen in equation 2.13 and repeated here for convenience:

$$\overline{t_{ij}} = 2\mu s_{ij} - \frac{2}{3}(\mu s_{mm})\delta_{ij} \tag{4.5}$$

Note, if the turbulence model directly calculates turbulence kinetic energy, $k \equiv \frac{1}{2}\left(\overline{u'} + \overline{v'} + \overline{w'}\right) = -\frac{1}{2}\tau_{ii}$, as most two-equation models do, than the constitutive equation must be adjusted as:

$$\bar{\rho}\tau_{ij} = -\overline{\rho u'_i u'_j} = 2\nu_T s_{ij} - \frac{2}{3}(\bar{\rho}k + \nu_T s_{mm})\delta_{ij} \tag{4.6}$$

Where the $-\frac{2}{3}\bar{\rho}k$ term ensures $k = -\frac{1}{2}\tau_{ii}$, but otherwise does not alter the orientation of the axes. Equation 4.4 (and 4.6) is acceptable for slowly varying near-isotropic turbulence even though physically, turbulence always lags behind and continually adapts to the mean strain rate. Turbulence occurs as a result of the mean flow. The turbulence lag increases with increased acceleration of the mean strain rate. In wing-tip vortices it is primarily the centripetal acceleration in the crossflow plane that creates a huge lag, or anisotropy, between the Reynolds stress tensor and the mean rate of strain tensor. The result is that EVMs will (mistakenly) increase the production of turbulence in a futile attempt to reduce the lag and attempt to make the Reynolds stress tensor coincide with the mean rate-of-strain tensor.

FRSMs individually calculate the six independent components of the Reynolds stress tensor—naturally accounting for the fact that turbulence will lag behind the mean strain rate. Rotation, streamline curvature, or any other form of mean strain rate

acceleration should not pose any difficulties with an FRSM. Contour plots in the vortex core are shown for each component of both the mean strain rate tensor, s_{ij}, and the Reynolds stress tensor, τ_{ij}. Figure 4.13 shows normal components and figure 4.13 shows the shear components. The mean strain rate components are plotted as $-s_{ij}$, where the equation is repeated for convenience:

$$s_{ij} = \frac{1}{2}\left(\frac{\partial u_i}{\partial x_j} + \frac{\partial u_j}{\partial x_i}\right) \tag{4.7}$$

The normal Reynolds stress components show misalignment with the mean rate-of-strain. (The Reynolds stresses properly show minima in the vortex core, this will be discussed in section 4.4.4). The turbulence lag is seen clearly in the shear component comparison. The standout observation is that the crossflow, $\overline{v'w'}$, Reynolds stress component shows a staggering $45°$ lag from the matching mean rate-of-strain—Figures 4.14 *e)* and *f)*, in agreement with Chow et al. [20]. This is caused by the swirling crossflow velocity in tip vortices and is what plagues EVMs from predicting a laminar vortex core.

Normal Components

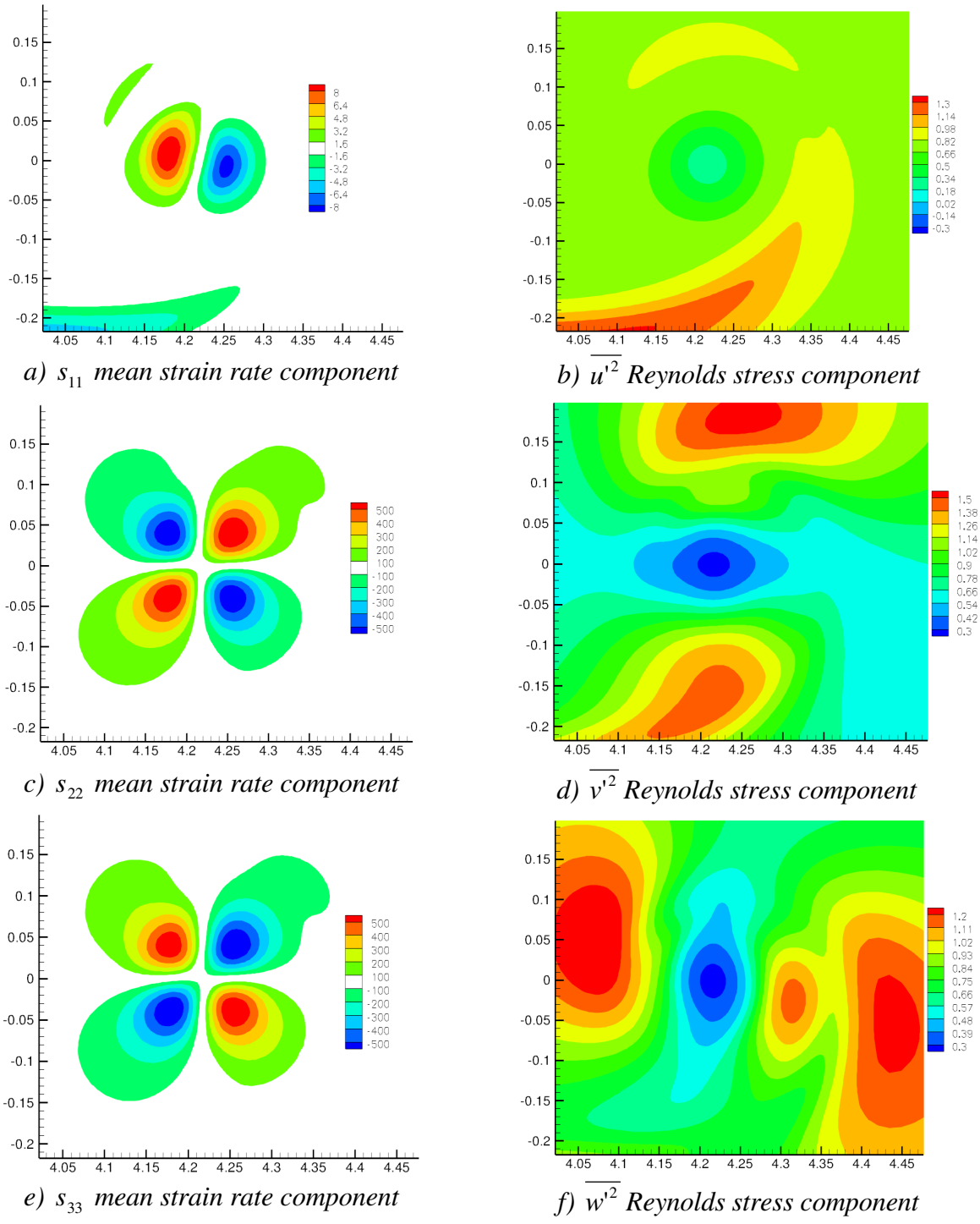

a) s_{11} *mean strain rate component*

b) $\overline{u'^2}$ *Reynolds stress component*

c) s_{22} *mean strain rate component*

d) $\overline{v'^2}$ *Reynolds stress component*

e) s_{33} *mean strain rate component*

f) $\overline{w'^2}$ *Reynolds stress component*

Figure 4.13 Normal Component Anisotropy of Mean Strain Rate and Reynolds Stress Tensor at 5c Downstream Station, Fine Grid, FRSM

Shear Components

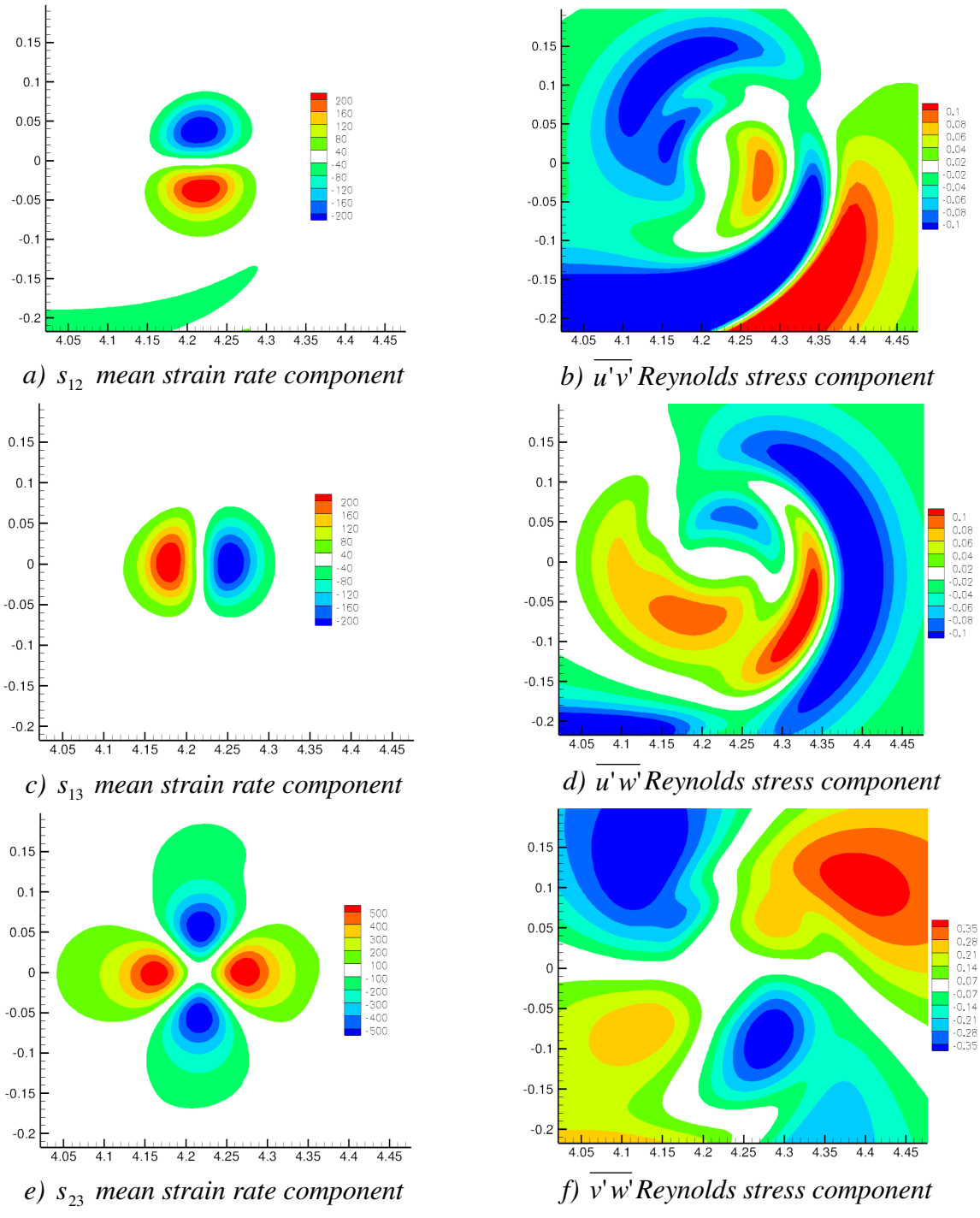

a) s_{12} *mean strain rate component*

b) $\overline{u'v'}$ *Reynolds stress component*

c) s_{13} *mean strain rate component*

d) $\overline{u'w'}$ *Reynolds stress component*

e) s_{23} *mean strain rate component*

f) $\overline{v'w'}$ *Reynolds stress component*

Figure 4.14 Shear Component Mean Strain Rate and Reynolds Stress Tensor Anisotropy at 5c Downstream Station, Fine Grid, FRSM

4.4.4: Predicting a Laminar Vortex Core

As the literature review indicates, the swirl velocity is a stabilizing mechanism for a vortex and the axial velocity deficit is destabilizing. Ragab et al. [28] show that when a stable vortex is subjected to perturbations, helical disturbances grow in such a way as to redistribute axial and angular momentum; this effectively reduces axial velocity deficit and re-strengthens the stabilizing rigid body rotation. In essence, the swirling velocity allows vortices to be very persistent and stable. Such a stabilizing effect should be linked with laminar flow. Zeman asserts that the turbulence production rates should be very nearly zero in the vortex core [14]. There should be a local minimum of turbulence kinetic energy, indicating that turbulence is passive, dominated by molecular viscosity, and that the core is laminar. Devenport et al. [15] use spectral decomposition to show that turbulent fluctuations in the core are orders of magnitude lower than the turbulent spiral wake. In this thesis a minimum of turbulence kinetic energy (per unit mass), *k*, will be the measure for determining whether the core is laminar.

$$k \equiv \frac{1}{2}\left(\overline{u'^2} + \overline{v'^2} + \overline{w'^2}\right) \tag{4.8}$$

Not all turbulence models directly calculate turbulence kinetic energy. The four main turbulence parameters are: turbulence kinetic energy, *k*, turbulent dissipation rate, ε, eddy viscosity, ν_T, and specific dissipation rate, ω (per unit TKE). Various length and time scales can be derived using combinations of the above. Arguably, the two most common, and physically intuitive, are *k* and ε ($\varepsilon \equiv -dk/dt$). The SA model solves a transport equation for ν_T. Approximate formulas for *k* and ε in terms of ν_T and velocity gradients are [52]:

$$k = \frac{\nu_T}{2a_1}\Omega^{1/2} \tag{4.9}$$

$$\varepsilon = C_\mu \frac{\nu_T}{4a_1^{\,2}}\Omega \tag{4.10}$$

Where, $a_1 = 0.15$, C_μ is an empirical constant and $\Omega = \frac{\partial u_i}{\partial x_j}\frac{\partial u_i}{\partial x_j}$. The equations were originally given by Spalart [52]. Equation 4.7 is used to calculate turbulence kinetic energy (TKE) for the SA models. The fine grid comparison for the three turbulence

models, (FRSM and SA w/ and w/out correction) at the 5*c* station is shown in Figure 4.15. The results are staggering. The original SA model shows a huge peak of turbulence kinetic energy—in what should be a laminar—core center, about twenty times greater than the turbulent wake. The corrected SA model shows significant improvement over the original model. It does show a local minimum at the vortex center, but still, even that is greater than TKE levels in the wake. Notice the locations (marked with an arrow) where the SA modification turns from "passive" ($|\omega_{ij}| \le |s_{ij}|$) to "active" ($|\omega_{ij}| \ge |s_{ij}|$). The FRSM is the only model to appropriately predict a true minimum at the vortex center that is significantly lower than the turbulent wake. But, unfortunately, the FRSM shows the presence of an "ambient" turbulence. TKE values far away from the vortex and wake should return to zero. This is a result of the user-defined turbulence prescribed at the pressure far-field boundary conditions (see Table 3.3).

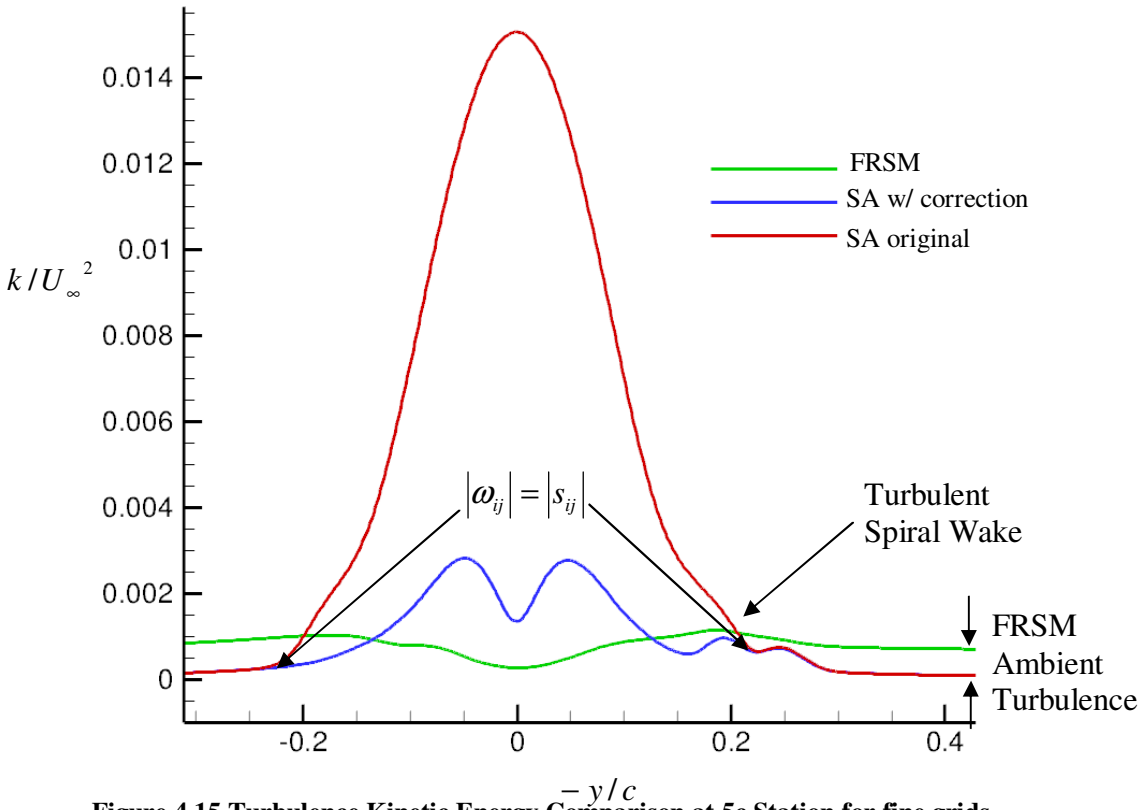

Figure 4.15 Turbulence Kinetic Energy Comparison at 5c Station for fine grids

To analyze the ambient turbulence further, all six Reynolds stress components are shown in Figure 4.16. Experimental Reynolds stress measurements are included. Reynolds stress uncertainties from wandering are more pronounced than mean velocity. They are shown in Table 4.5. When comparing Reynolds stresses, it is more appropriate to look for qualitative agreement and not brute accuracy.

Table 4.5 Experimental Reynolds Stress Uncertainty from Wandering [15]

Quantity	Spiral wake $\times 10^{-6}$	Core $\times 10^{-5}$
$\overline{u'^2}/U_\infty^2$	3.1	1.4
$\overline{v'^2}/U_\infty^2$	9.5	1.5
$\overline{w'^2}/U_\infty^2$	9.9	2.0
$\overline{u'v'}/U_\infty^2$	4.3	1.4
$\overline{u'w'}/U_\infty^2$	4.5	2.3
$\overline{v'w'}/U_\infty^2$	2.9	0.85

The experimental Reynolds stress data shows huge overshoots in all components directly at the core center. If this peculiarity (most definitely an artifact of wandering) is set aside, then some of the plots show rough qualitative agreement, such as Figure 4.16 *a), b),* and *f).* The $\overline{v'w'}$ plot shown in Figure *f)* probably shows the best agreement and has the least experimental uncertainty. It is the most distinctive Reynolds stress component because it is shows the anisotropy. The ambient turbulence problem is unmistakable in the normal Reynolds stress components, Figure 4.16 *a), b),* and *c).* Contour plots of $\overline{u'^2}/U_\infty$ are shown at 5*c*, 10*c*, 15*c*, and 20*c* stations in Figure 4.17. The ambient turbulence of roughly $\overline{u'^2}/U_\infty^2 = 35\times 10^{-5}$ (shaded light blue) is obvious everywhere. Also, the effect of numerical diffusion is clearly evident.

Reynolds stress comparison

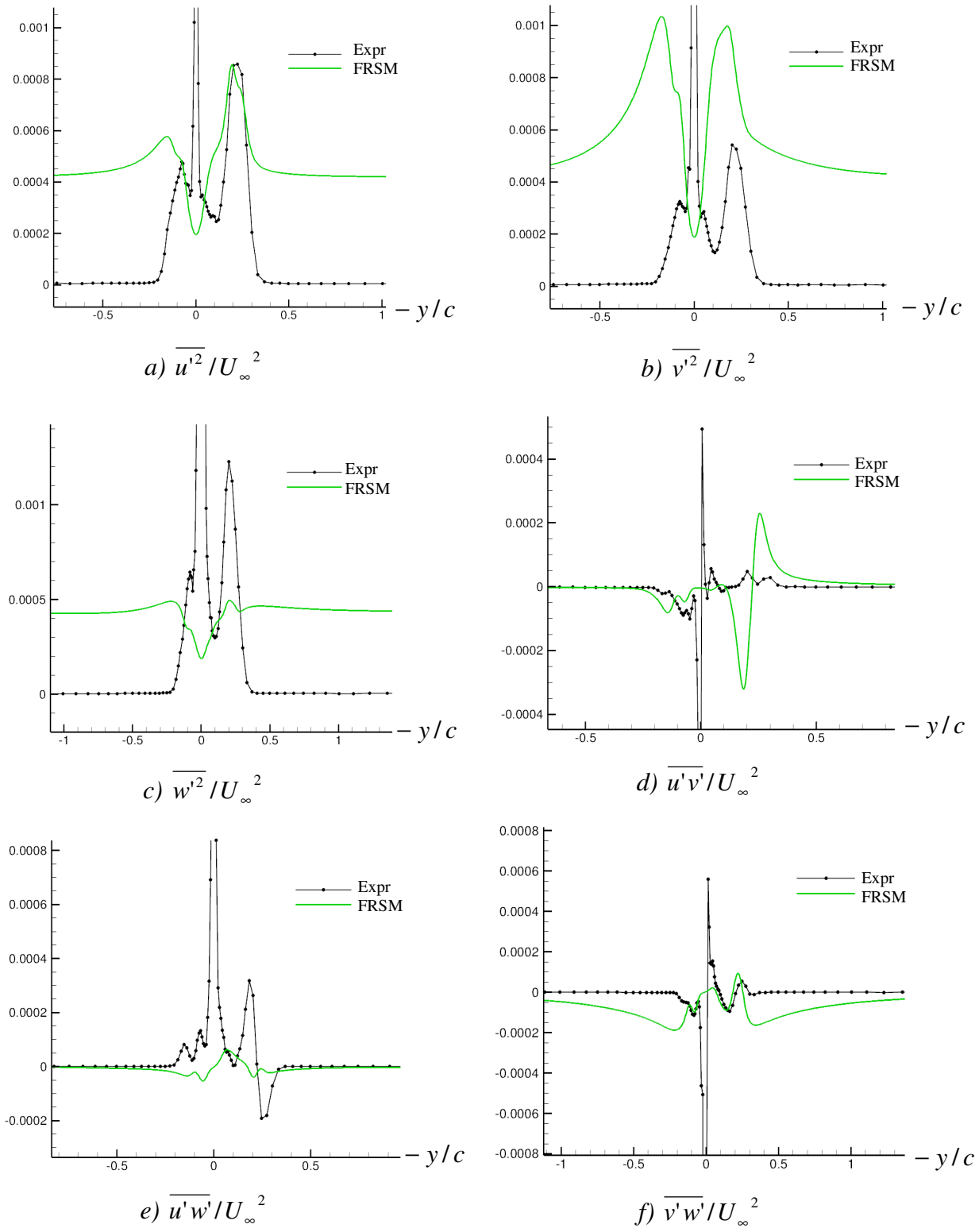

Figure 4.16 Reynolds Stress Comparison with Experiment at 5c Station, FRSM Fine Grid

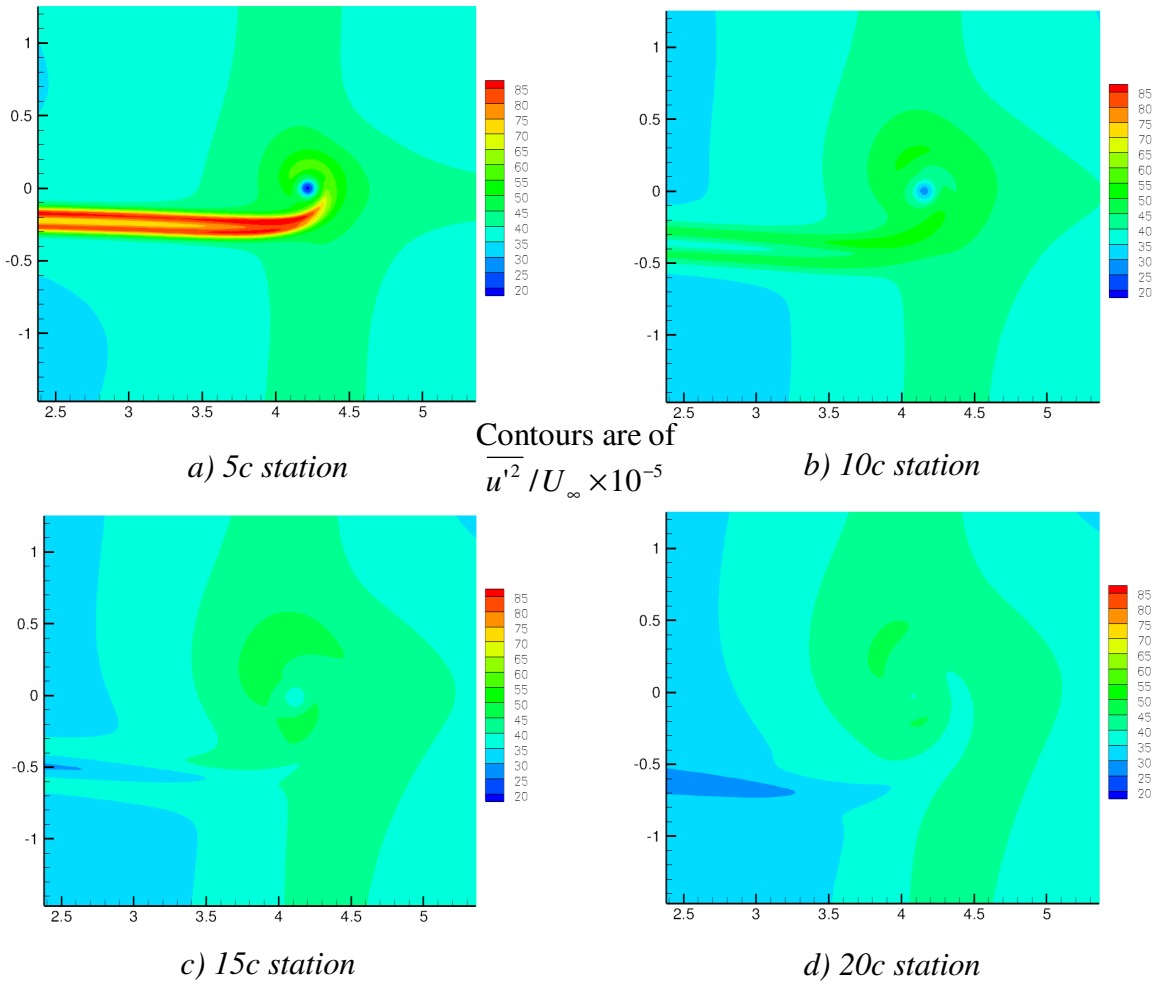

Figure 4.17 uu Reynolds Stress Component at 5c, 10c, 15c, and 20c Downstream Stations

The ambient turbulence incongruity observed in Figures 4.15 – 4.17 can be explained by an over-prescription of turbulence at the pressure far-field (inflow) boundary conditions. In FLUENT the boundary condition turbulence levels are prescribed via turbulence kinetic energy. All of the FRSM simulations in this thesis use the default value of $k = 1\frac{m^2}{s^2}$ (as shown in Table 3.3), where $k \equiv \frac{1}{2}\left(\overline{u'^2} + \overline{v'^2} + \overline{w'^2}\right)$. This implies:

$$\overline{u'^2} = \overline{v'^2} = \overline{w'^2} = \frac{2}{3}\left(1\frac{m^2}{s^2}\right) \tag{4.11}$$

and,
$$\overline{u'v'} = \overline{u'w'} = \overline{v'w'} = 0 \tag{4.12}$$

The boundary condition turbulence level affects the ambient turbulence throughout the entire computational domain. Equation 4.11 states that the square of normal turbulent fluctuations is $\frac{2}{3}m^2/s^s$ or 0.00046 when normalized with $U_\infty{}^2$. This closely matches the "ambient" turbulence seen in Figure 4.16 *a), b),* and *c)* and also Figure 4.17. (Note that the effects of gridding can be seen in Figure 4.17. Higher ambient turbulence closer to 0.00046 shaded in *green* is in a high density grid region implying that denser grid preserves the boundary condition turbulence more than the coarse grid section). Equation 4.12 states that ambient shear turbulent fluctuations is zero, which agrees with Figure 4.16 *d), e),* and *f).* The actual magnitude of turbulent velocity fluctuations is 0.816*m/s* or about 2% of the free-stream velocity (known as turbulence intensity):

$$\overline{u'} = \overline{v'} = \overline{w'} = \sqrt{\frac{2}{3}\left(1\frac{m^2}{s^2}\right)} \approx 0.816\frac{m}{s} \tag{4.13}$$

The Virginia Tech Stability Wind Tunnel, where the experimental data was measured, features a very low turbulence intensity of about 0.03% [53]. The over-prescription of turbulence in the simulations was an over-sight. The initial turbulence intensity should have been set to 0.03%. It is plausible that the Reynolds stresses in Figure 4.16 would have been more comparable to experiment. Nonetheless, the mean flow results, even with excessive ambient turbulence, are a remarkable testimony for the use of FRSMs.

4.4.5: Near-Field Vortex Roll-Up

The purpose of the near-field vortex roll-up analysis is not only to further understand the effects of turbulence modeling, but also to gain insight into the complex physical features of the roll-up process. The goals in this section are: to qualitatively locate smaller secondary vortices as described by Devenport et al. [15], and Duraisamy [22]; to investigate when the vortex core becomes laminar; and, to see if there is in fact an axial velocity *surplus* as described by Chow et al. [20].

All of the near-field figures are created with ten planes of constant *x* separated by a distance of $\frac{1}{5}c$. The furthest downstream plane is $x/c = 1$ and only fine grid simulations are shown. Contours of TKE for the FRSM, SA w/ correction, and SA original are shown in Figure 4.18, Figure 4.19, and Figure 4.20, respectively. These

figures show that the original SA model drastically and immediately over-predicts core TKE levels. The corrected SA model is a significant improvement, but, does not match the FRSM in predicting *full* core laminarization, because, core TKE values are about the same as the turbulent wake. If the FRSM simulation is assumed to be accurate then it does not predict an *initially* fully turbulent core as suggested by Chow et al. The Reynolds number of Chow et al. is $\mathrm{Re} = 4.6\times10^{6}$ and probably explains why their vortex is more turbulent than the current simulation ($\mathrm{Re} = 530000$). It is unclear where exactly the vortex core becomes fully laminar, but does appear to become increasingly laminar with increased downstream distance.

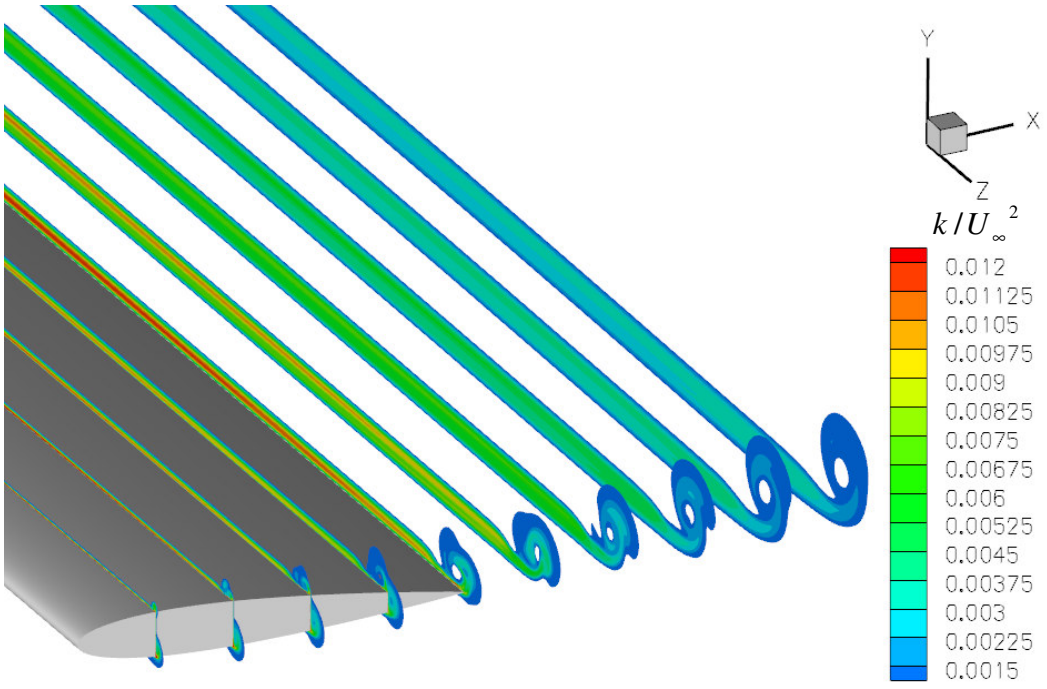

Figure 4.18 Near-Field Turbulence Kinetic Energy, FRSM

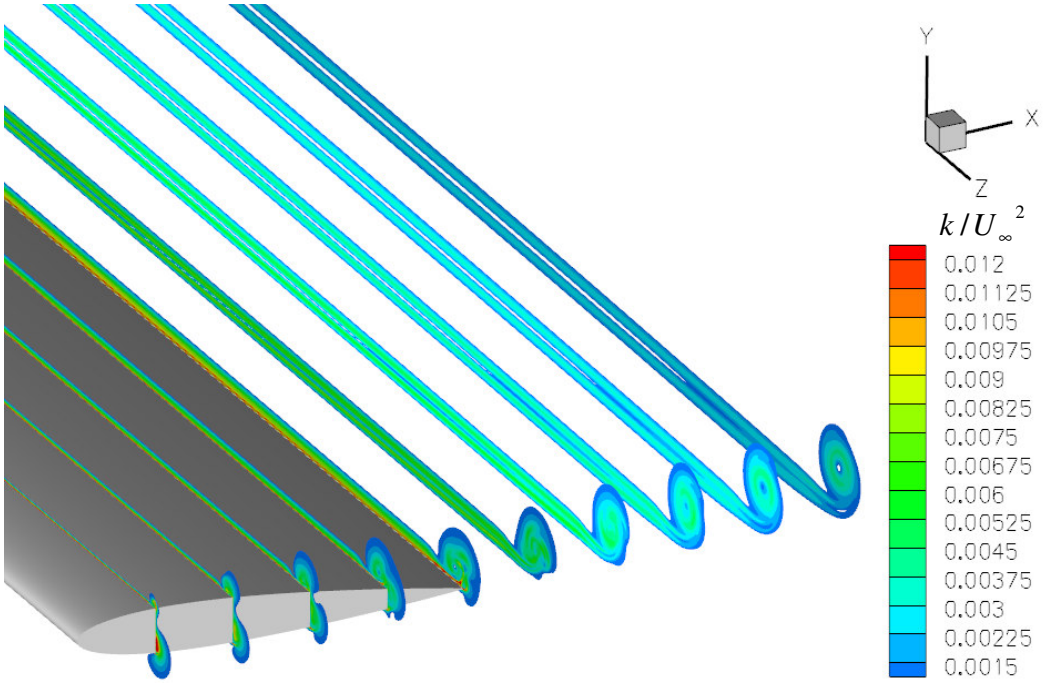

Figure 4.19 Near-Field Turbulence Kinetic Energy, SA w/ correction

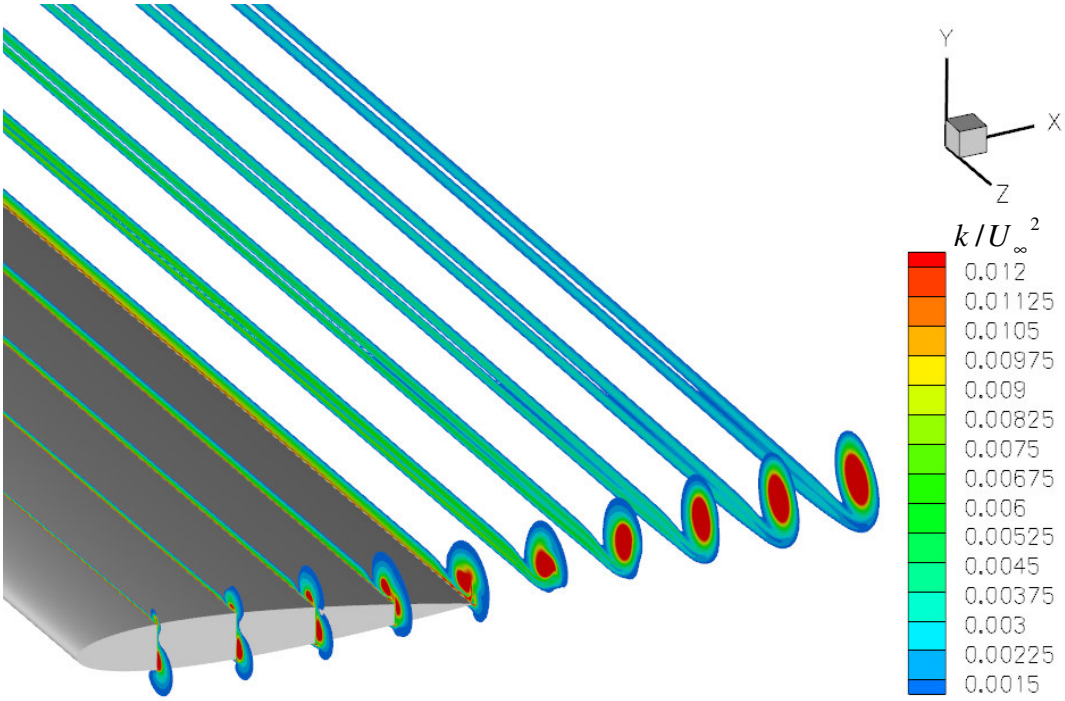

Figure 4.20 Near-Field Turbulence Kinetic Energy, SA Original

In addition to the near-field TKE, contours of crossflow velocity are shown for each turbulence model in Figure 4.21, 4.22, and 4.23. The standout observation is that the FRSM predicts the highest swirl velocities even at the trailing edge.

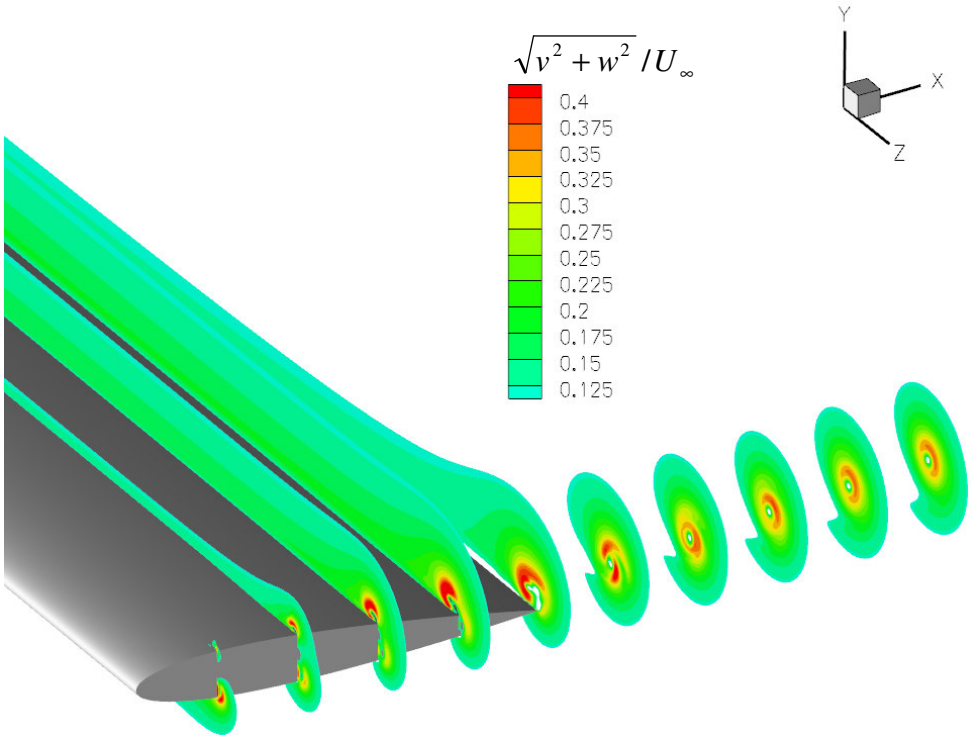

Figure 4.21 Near-Field Crossflow Velocity, FRSM

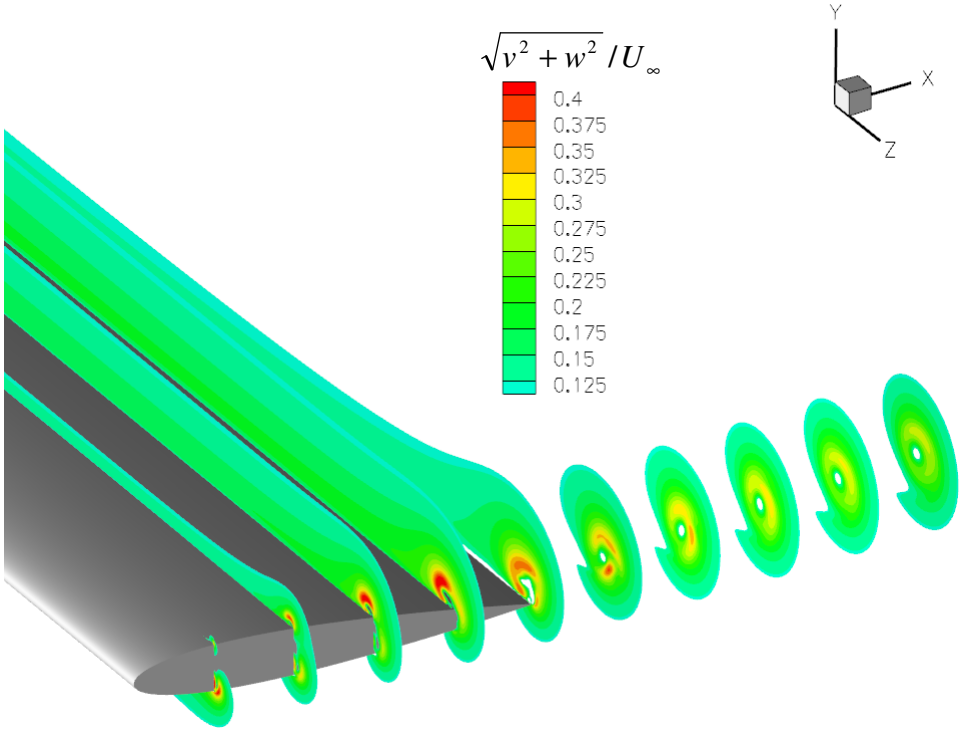

Figure 4.22 Near-Field Crossflow Velocity, SA w/ correction

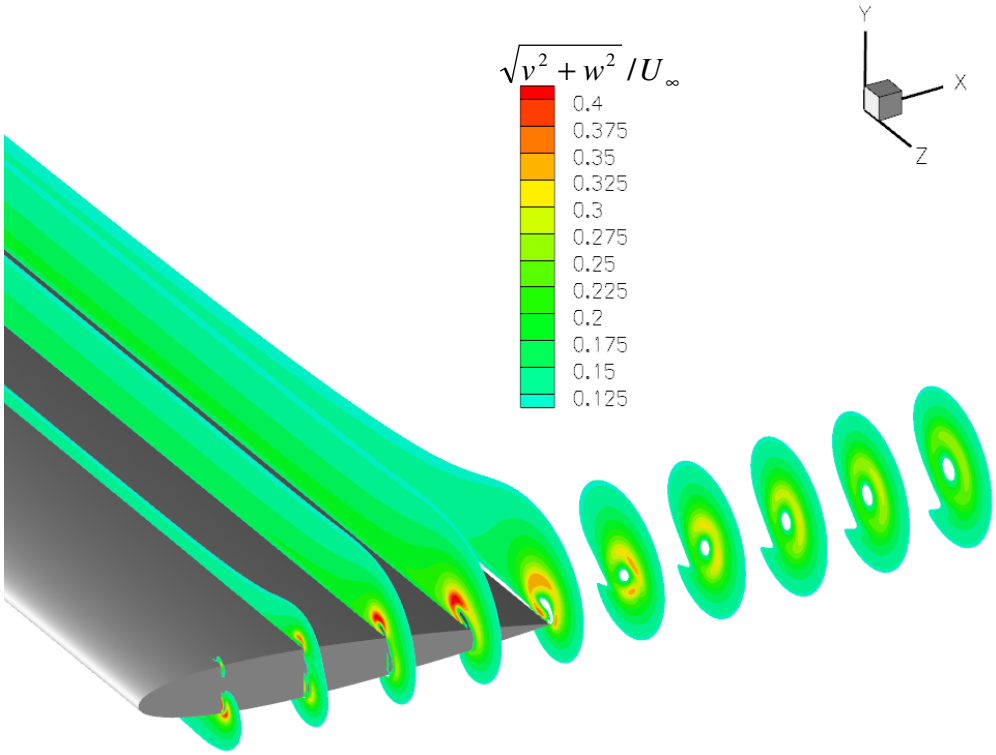

Figure 4.23 Near-Field Crossflow Velocity, SA original

The near-field axial velocity deficit is shown in Figure 4.24 for just the FRSM. Even with the significantly lower Reynolds number than Chow et al. (1997) it does predict a small axial velocity surplus in the same location. Development of the primary vortex is seen at about mid chord on the suction side and the distortion effects of a co-rotating vortex developing on pressure side are seen just downstream of the trailing edge before it is absorbed into the primary vortex as suggested by Devenport et al [15]. On the suction side, there is the evidence of a small counter-rotating secondary vortex created by close proximity of the primary vortex to the no-slip wall.

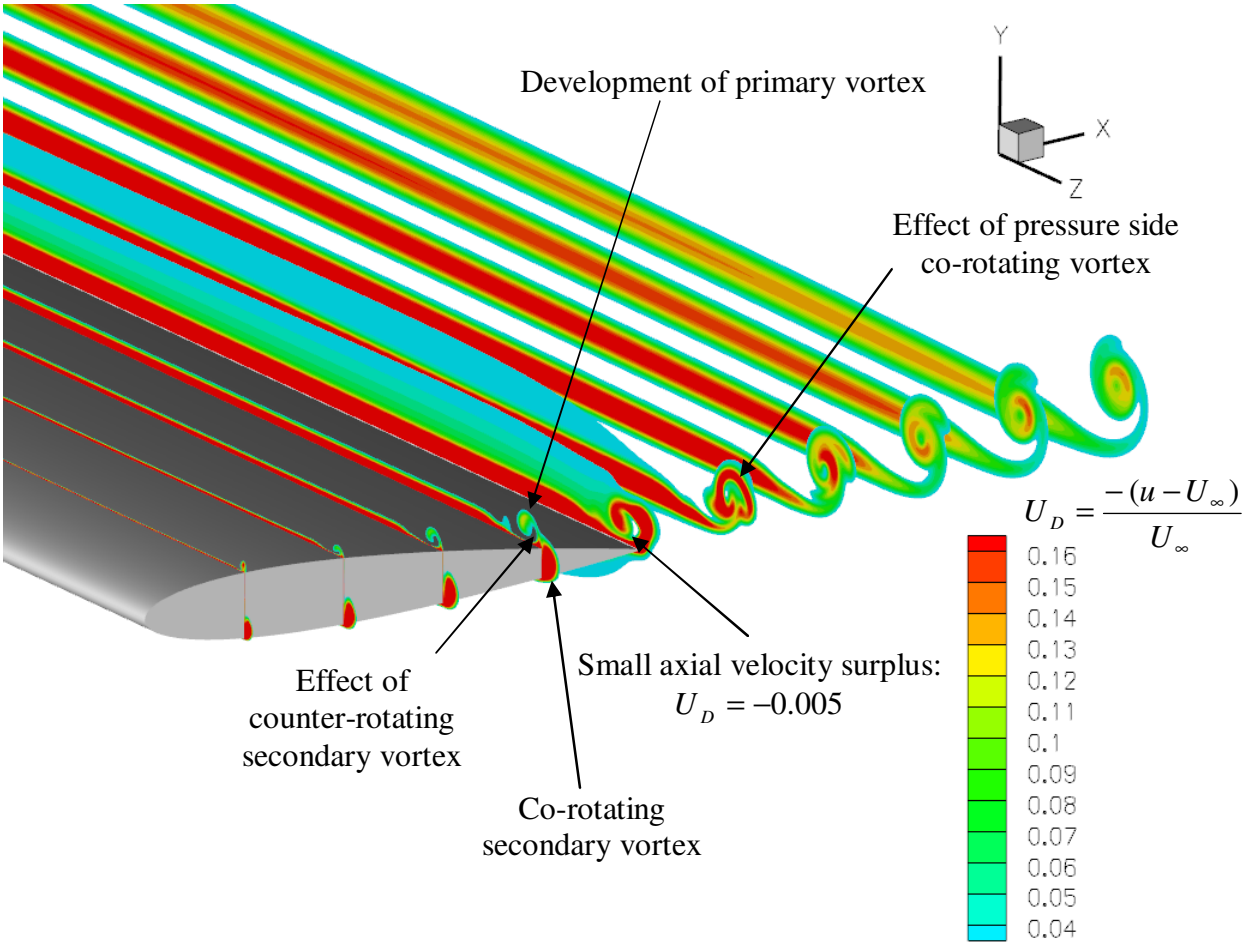

Figure 4.24 Near-Field Axial Velocity Deficit, FRSM

The full mirror-reflected wing is shown in Figure 4.25 with contours of axial velocity deficit at 1*c*, 2*c*,…,10*c* stations. The computational results properly predict increasing distance from the vortex core to the spiral wake. There is very conclusive

evidence that the FRSM fine grid simulation accurately predicts mean flow quantities up to 5*c* downstream of the trailing edge.

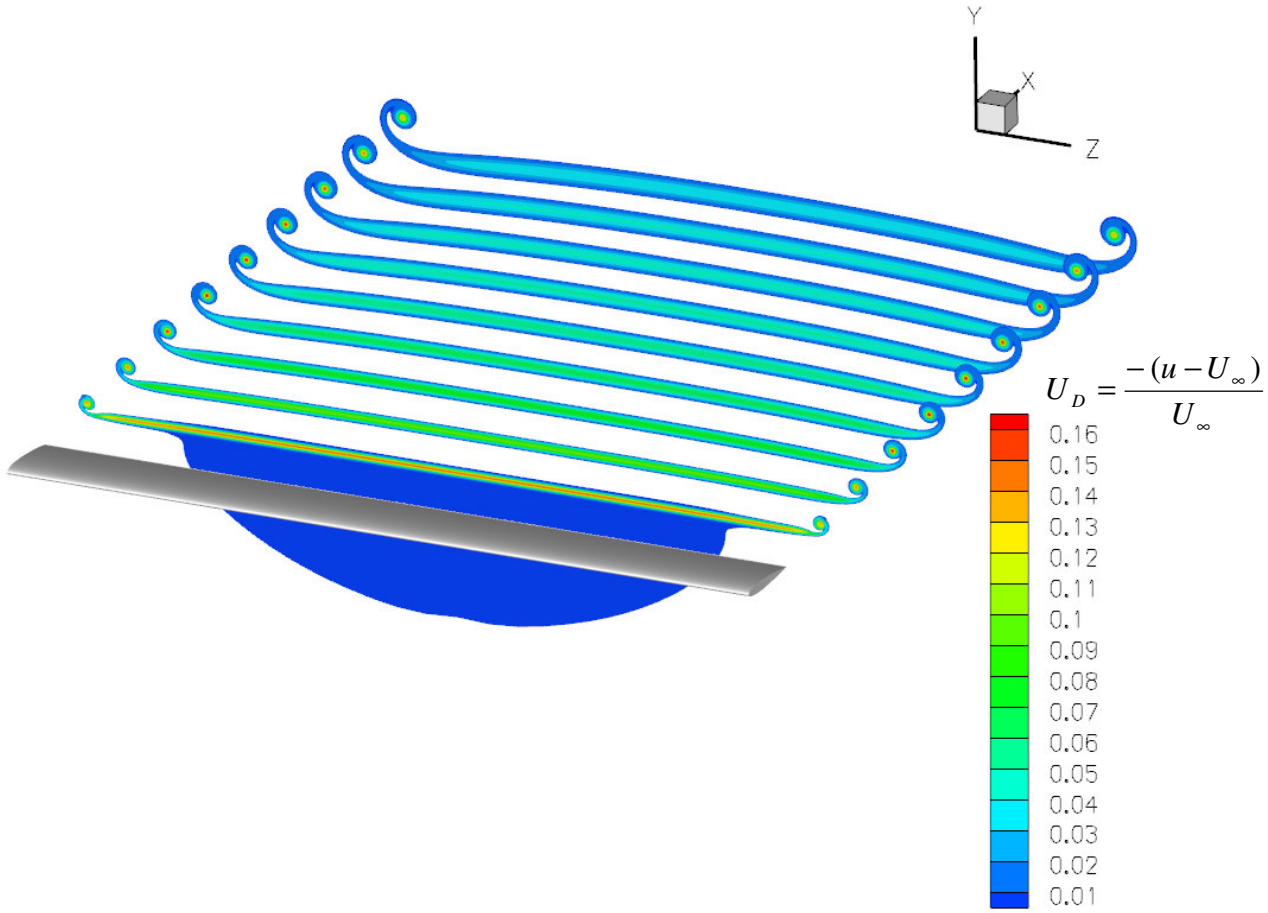

Figure 4.25 Axial Velocity Deficit 1c, 2c…, 10c Downstream Stations with FRSM Fine Grid

4.5: Conclusions

There were several notable conclusions from this chapter. It was shown that FRSMs are more sensitive to gridding; they, in general, require higher mesh resolutions, and, will prove to be more difficult to show grid independence. The 3rd order upwind biased differencing scheme with at least 16 grid points within the vortex core showed minimal vortex diffusion at 5*c* downstream station; but, at 10*c*, diffusion was evident. The FRSM displayed remarkable agreement with experimental measurements in vortex velocity profiles and was the only model to predict a truly laminar vortex core. The vortical flow correction term, $S \equiv |\omega_{ij}| + 2.0 \min\left(0, |s_{ij}| - |\omega_{ij}|\right)$, is a *drastic* improvement

over the original ($S \equiv \sqrt{2\omega_{ij}\omega_{ij}}$) for the prediction of vortex velocity profiles and lower TKE levels in the vortex core. A 45° lag in the τ_{23} Reynolds stress component compared to the s_{23} component of mean strain rate is the main contributor of anisotropy. Comparison of Reynolds stresses to experimental measurements was obscure; rough agreement was shown for some components, but not for others. In the near-field analysis, the vortex core was not found to be fully turbulent, but, it was shown to become more laminar with downstream distance.

Conclusions can be made on regarding Spalart's turbulence modeling challenges [8]. For *challenge one*, boundary layer growth prediction, the models were found to be roughly equal. For *challenge two*, free-shear momentum transfer, the FRSM was shown to be significantly better the either SA variant.

The idea of using more complex turbulence models on *coarse* grids instead of less complex models on *fine* grids should be explored further; the FRSM on the coarse grid yields better results (with regard to vortex resolution) than the SA models (both versions) on the fine grid, requires less computational resources, less time to convergence, and solves for Reynolds stresses.

In essence, for vortex flow simulations, equal attention should be paid to turbulence modeling as given to grid resolution and differencing scheme.

Chapter 5 Rotorcraft Simulation

This chapter is a brief qualitative study on rotorcraft wake-age in hover conditions. The main purpose is to show the current state of RANS simulations. The wake from a rotor craft is far more complex than its fixed wing counterpart. The blade loading near the hub is drastically different from the tip region because of the rotational velocity, $v = \omega r$. For a multi-blade rotor (which includes nearly all of them) in hover, the tip vortex from blade #1 will pass very close to the oncoming blade, #2, creating the so-called Blade-Vortex Interaction (BVI). The tip-vortex will most certainly alter the logarithmic law of the wall on blade #2, suggesting the need for high resolution wall treatments. High order accuracy schemes are required to resolve the vortex as it travels through the downwash shear layer produced by thrust of the blade. The far-field boundary conditions are also more problematic to manipulate because there is no free-stream velocity to fix the dynamic pressure. A large computation domain must be used.

5.1: Geometry and Boundary Conditions

The rotorcraft model is a crude approximation of a four bladed Sikorsky S-76 rotor. The VR12 airfoil geometry is used (not the actual S-76 airfoil). The airfoil data coordinates are shown in Appendix B. Blade length is $b = 6.7m$ and chord is $c = 0.4m$. Tip speed is $v_t = 205.69m/s$ and tip Reynolds number is $\mathrm{Re}_c = 5.6M$, corresponding to actual hover conditions. The angle of attack of the rotor is constant, $\alpha = 10°$. A rotating frame of reference with respect to the blades is used to resolve the rotor in a steady state. Rotation is about the positive *z*-axis. Coriolis and centripetal acceleration effects are added to the governing equations via source terms. The computational domain features only $90°$ azimuth angle wedge and one blade; as a result periodic boundary conditions are utilized. The grid contains 15M elements. The computational domain is shown in Figure 5.1 and 5.2. A curved outer side surface (not-shown in Figure 5.1) is a pressure inlet. The boundary conditions and differencing schemes are summarized in Table 5.1 and 5.2, respectively. 2nd order upwind differencing was used because it predicted "smoother" velocity stream traces in the far field. When the 3rd order scheme was used the velocity stream traces were seen to converge into each other.

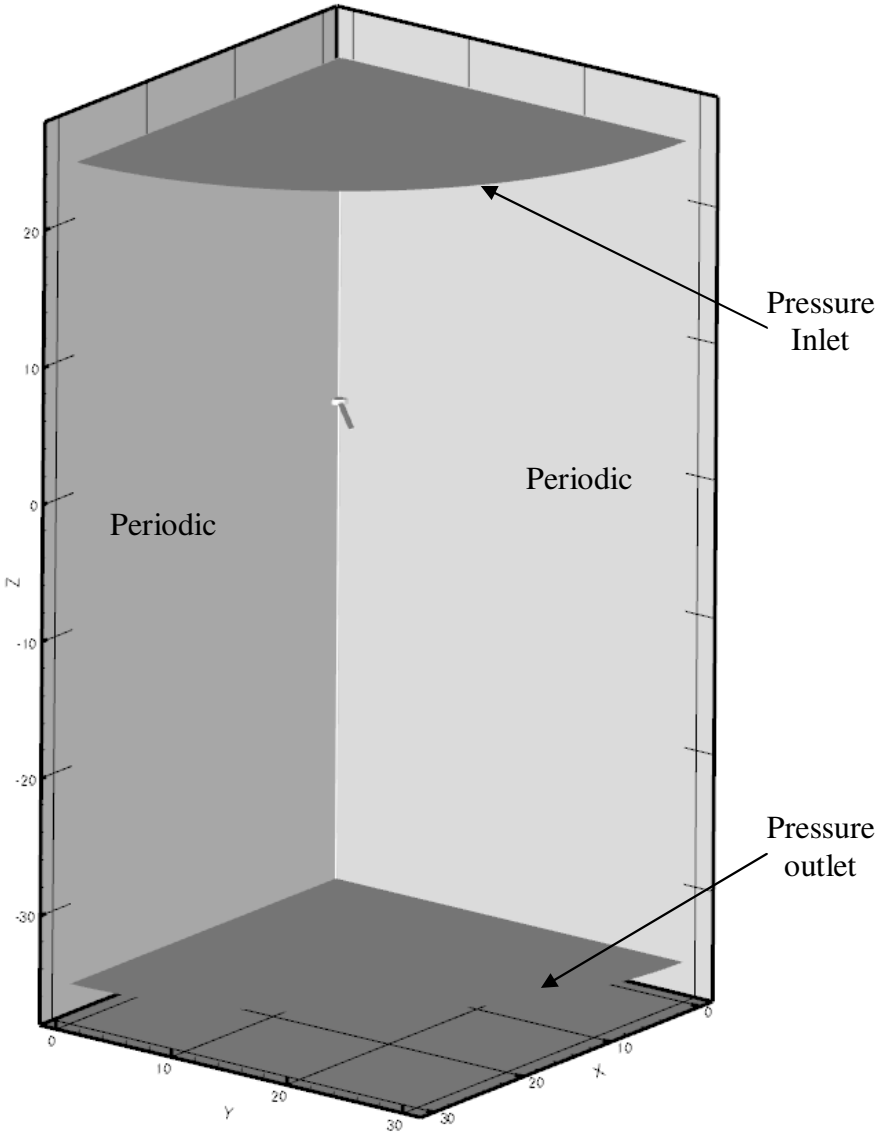

Figure 5.1 Computational Domain and Boundary Conditions

Periodic boundaries cannot intersect because of the derivatives and fluxes are calculated on them. Therefore, a small rod is included parallel to the *z*-axis as shown in Figure 5.2.

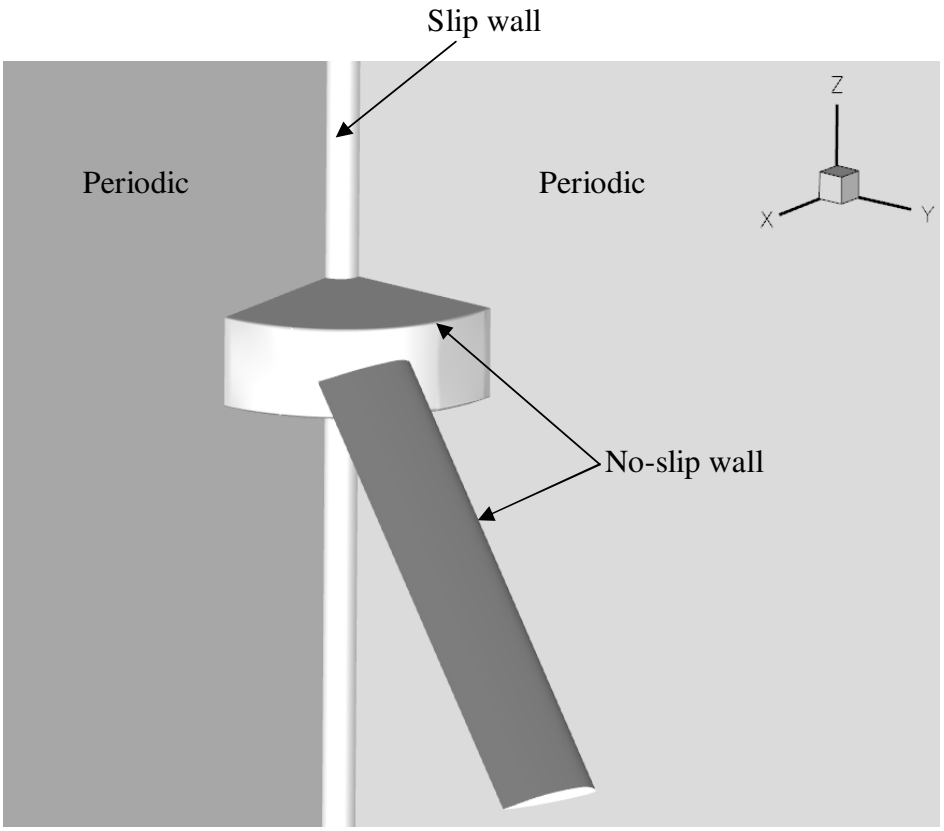

Figure 5.2 Close View of Computational Domain

Table 5.1 Boundary Conditions and settings

Fluid	Rotating reference frame $\omega_z = 30.7 rad/s$
Periodic	Rotational Periodicity
No-slip wall	$u_i = 0$ (no-slip condition) Roughness Constant = 0.5 Heat flux = 0 Stationary wall
Slip-wall	$\tau_w = 0$ Stationary wall
Pressure inlet	$p_{guage} = 0$ $\tilde{\nu} = 0.001 m^2/s$
Pressure outlet	$p_{guage} = 0$ $\tilde{\nu} = 0.001 m^2/s$ Backflow velocity normal to boundary

Table 5.2 Differencing Schemes

SA model	Pressure	Standard
	Density	2rd order upwind
	Momentum	2rd order upwind
	ν_T	2rd order upwind
	Energy	2rd order upwind

5.2: Grid

The grid was created in GAMBIT and is shown in Figures 5.3 – 5.6. The rotorcraft grid development was an arduous process compared to the fixed wing. Non-conformal grid boundaries were experimented with in the early stages but were abandoned because of glitches at curved interfaces. The non-conformal boundary seemed to effect the calculation of fluxes, particularly in the far-field.

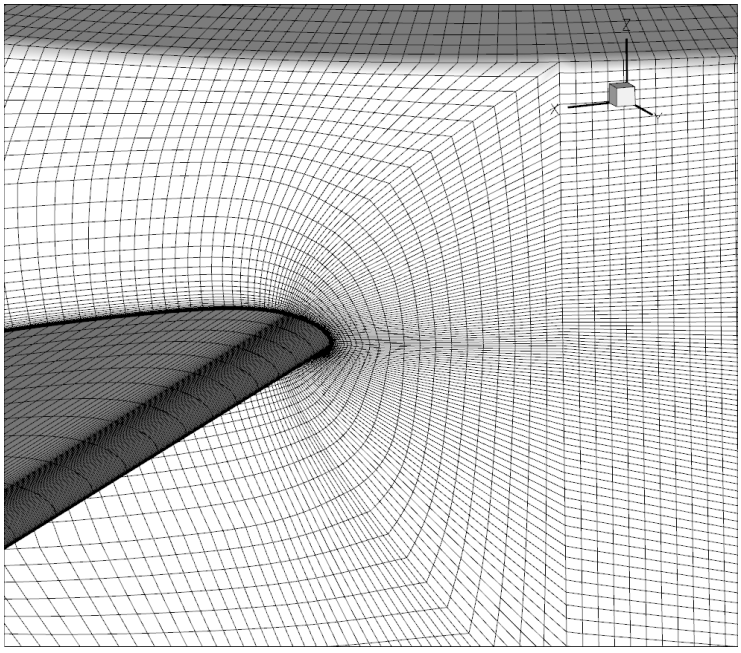

Figure 5.3 Hub and Rotor Mesh showing the boundary layer grid

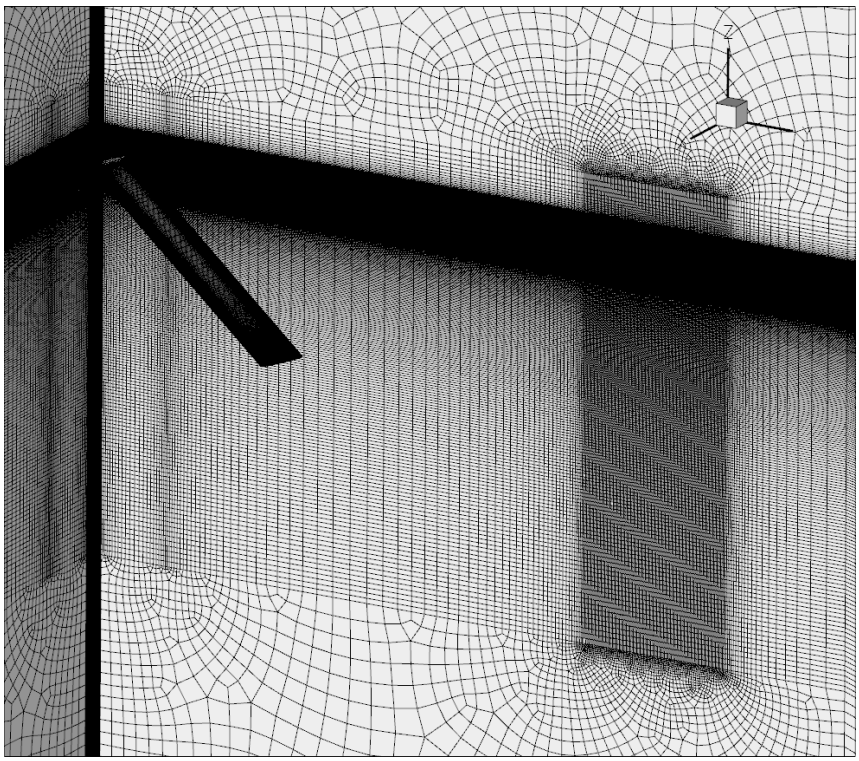

Figure 5.4 Mesh to Resolve the Tip-Vortices

Figure 5.5 Blade Surface Mesh

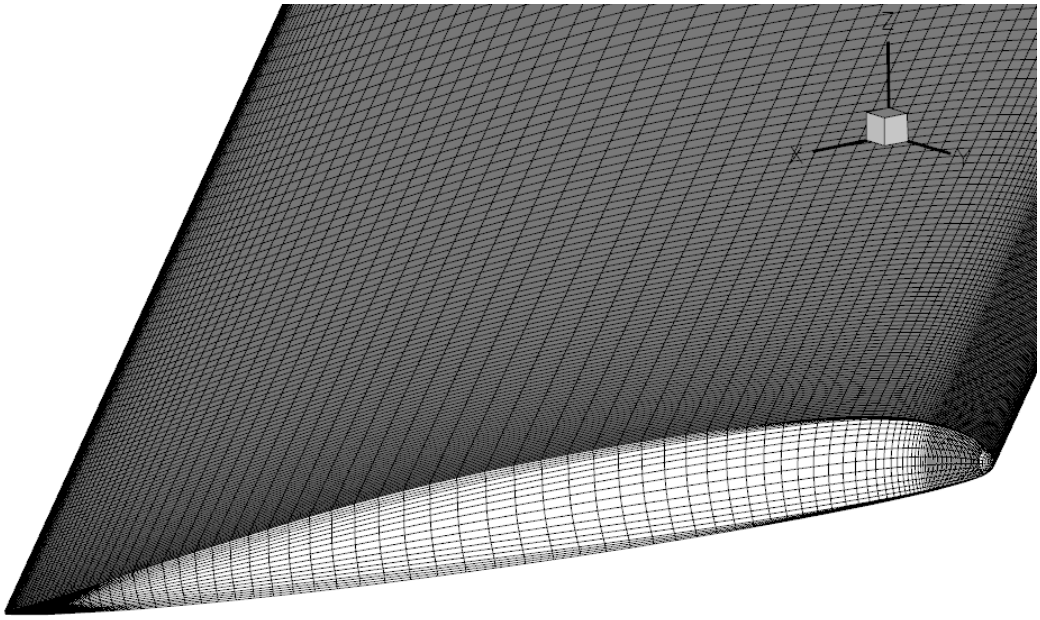

Figure 5.6 Blade Tip Mesh

5.3: Results

The goals in this chapter are mainly to show qualitative agreement with the accepted wake structure of a hovering rotorcraft. Unlike chapter 4, which featured quantitative comparisons of three different turbulence models, only the SA model (with vortical correction) was simulated. The FRSM model repeatedly failed to converge on the grid shown, as well as a plethora of others. The original SA model was not tested due to its obvious failure to resolve free-shear vortical flows (as shown in chapter four).

Figure 5.7 shows a vorticity isosurface of $\omega = 200 s^{-1}$. The image was created by rotating and copying the $90°$ wedge that was actually simulated three times to complete the $360°$, 4-blade rotor. Most of the wake is seen to immediately roll up into the vortex. The isosurfaces show the tail end of a vortex sheet entrained between two vortices. This vortex sheet is described by Leishman et al. [19] and Martin et al. [11]. Figure 5.7 *b)* shows excellent inboard drift of the wake.

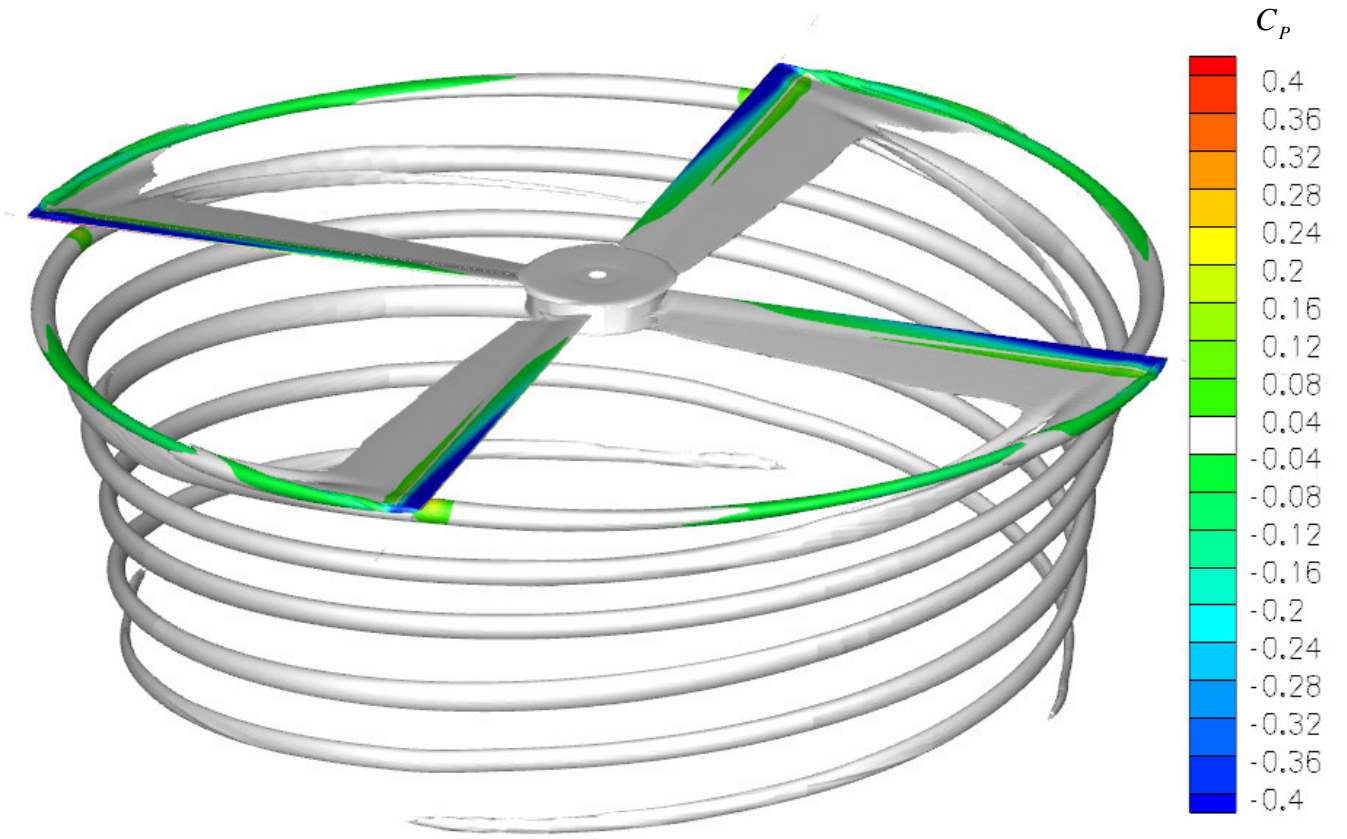

a) top perspective view

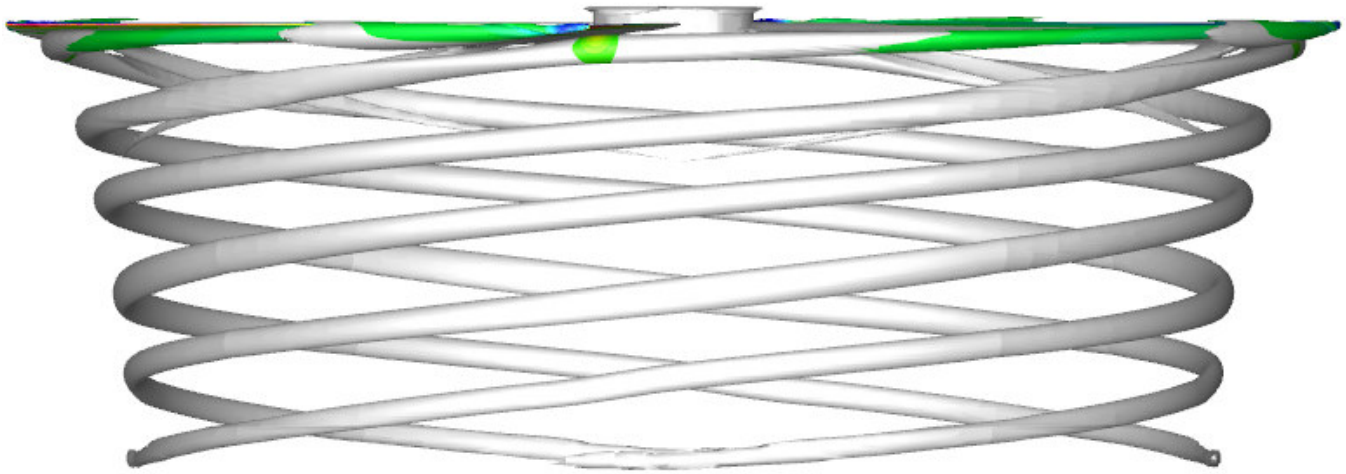

b) side view

Figure 5.7 Vorticity iso-surface Colored by Contours of Pressure Coefficient

Other qualitative wake images are shown in the *y-z* plane (also a $45°$ azimuth plane). The images in the plane capture the tip vortex-vortex sheet interaction better. Figure 5.8 shows a low-level contour plot of ω_x. Leishman claims, "modern CFD methods…have not yet allowed the details of the vortex sheet and the tip vortex to be fully resolved because of rapid artificial numerical diffusion…" [19]. Figure 5.8 suggests that the interaction of the tip vortex and the vortex sheet is being, at least partially, resolved for close to 1.5 full revolutions of the tip vortex (in consideration of the periodic boundary conditions, each vortex appearance represents a $90°$ revolution).

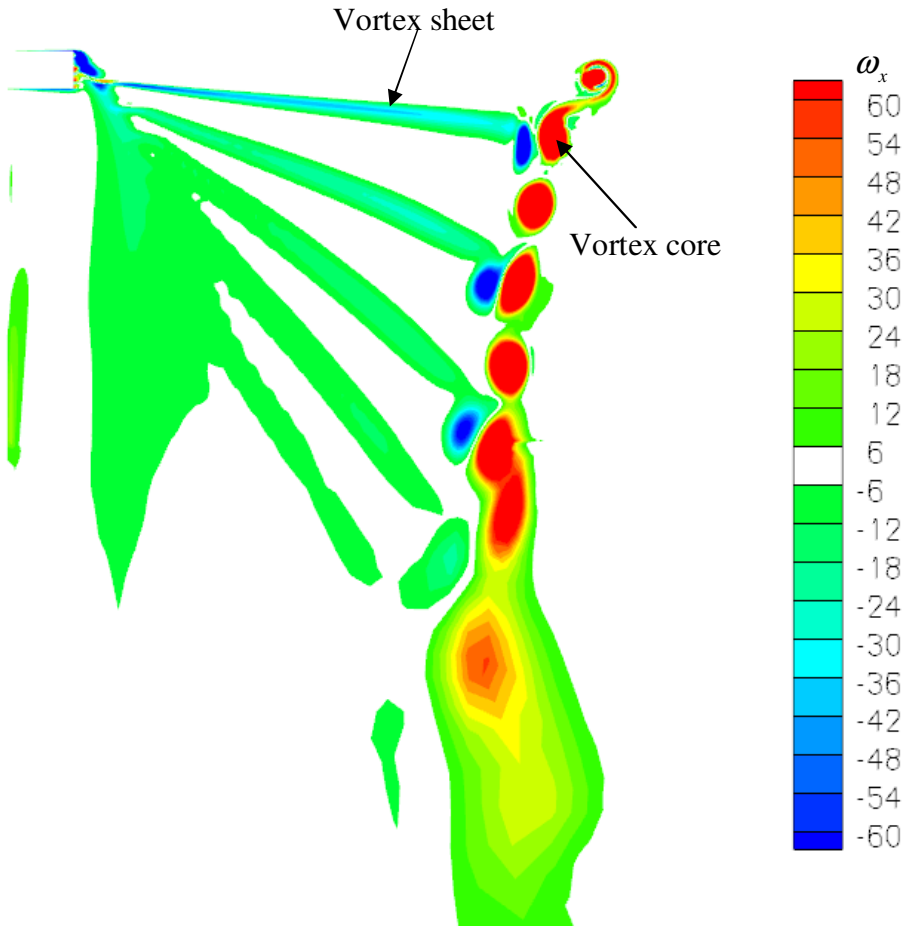

Figure 5.8 Low-level vorticity contours on the azimuth plane

Figure 5.9 shows negative values of λ_2 (see Appendix A for more information). To filter out small disturbances near zero the value is plotted as $\lambda_2 \leq -1$. The λ_2 definition indicates that the tip vortices are orders of magnitude lower the vortex sheet disturbance

implying that they are a more coherent structure. But, the low contour levels still show clear evidence of the interaction of the tip vortex with the vortex sheet.

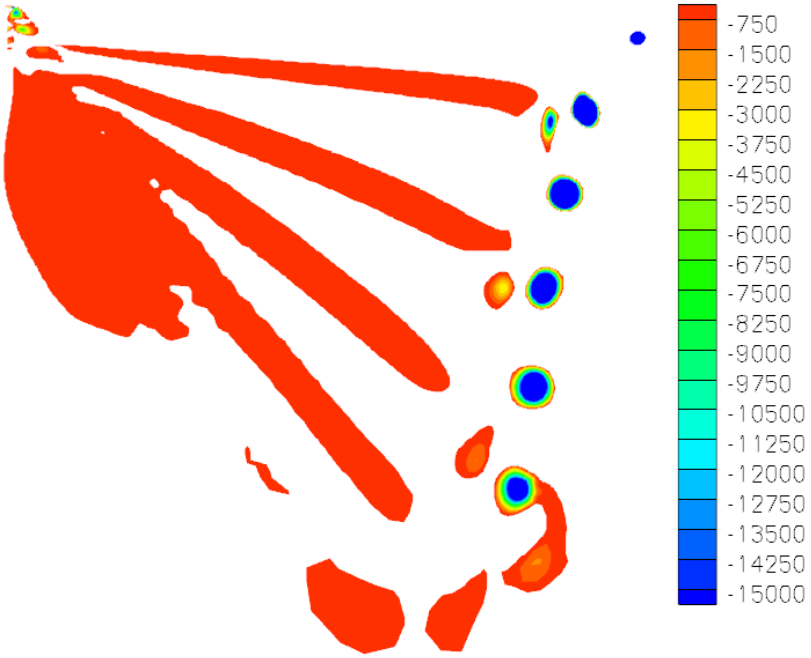

Figure 5.9 Lambda 2 Contours on the Azimuth Plane

Figure 5.10 shows a similar plot, but with overset velocity stream traces on top of the contours. The stream traces indicate that there are six vortices powerful enough force a swirling streamline.

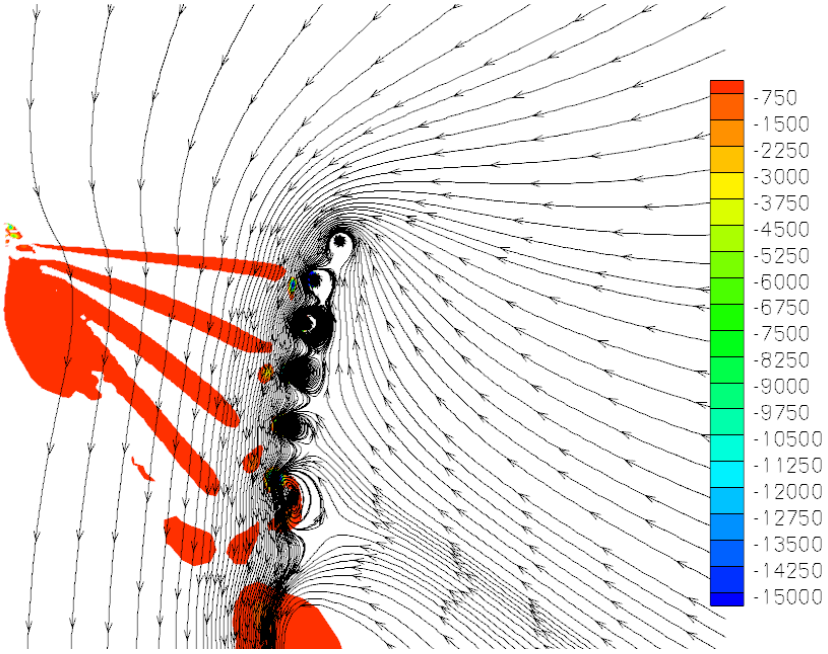

Figure 5.10 Lambda 2 Contours on the azimuth plane with Velocity Stream Traces

Perhaps the most interesting plot is a "zoomed out" version of Figure 5.9. The low levels of in the λ_2 definition seem to be predicting the unsteady oscillating effect from two nearby vortices. Using the λ_2 definition, this effect is captured in a very coarse grid section. It would be interesting to see what would happen on a grid with higher resolution. The resolution of wake-age is clearly altered when the grid changes from the high density structured mesh to the coarse unstructured mesh.

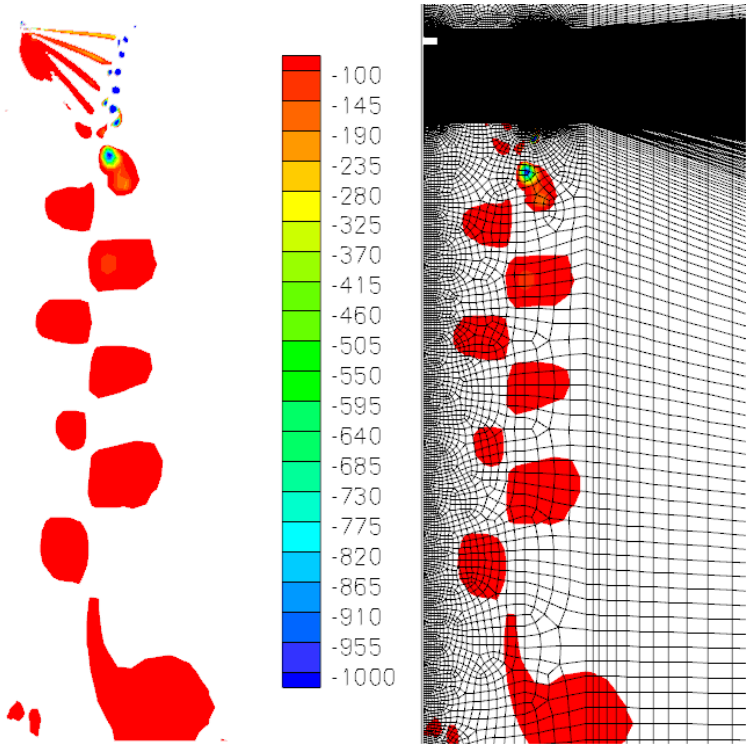

Figure 5.11 Lambda 2 Contours on a Zoomed out Azimuth Plane

5.4: Conclusions

In this section a qualitative analysis of rotorcraft wake-age was performed. It was determined that the SA model was able to visually resolve close to 1.5 revolutions of a vortex tube. This was greatly alleviated by taking advantage of the periodic boundary conditions and only simulating one blade. The λ_2 definition of Jeong and Hussain [9] was found to be extremely valuable in discerning coherent structures in the wake such as the entrainment of the vortex sheet. The definition is also extremely easy to use—simply plot negative values.

Chapter 6 Conclusions

This chapter summarizes the main conclusions from this thesis. The most important findings are contained in chapter 4, with the finite wing RANS simulations. They are summarized as follows:

1) The FRSM simulation showed *remarkable* agreement with experimental measurements in vortex mean velocity profiles (at the 5*c* downstream station) and was the only model to properly predict a laminar vortex core.
2) The vortical flow modification to the source term, $S \equiv |\omega_{ij}| + 2.0 \min\left(0, |s_{ij}| - |\omega_{ij}|\right)$, applicable to many EVMs, is a *drastic* improvement for the prediction of vortex velocity profiles and lower TKE levels in the vortex core.
3) A 45° lag in the $\overline{v'w'}$ Reynolds stress component compared to the s_{23} component of mean strain rate is a significant contributor of anisotropy.
4) A 3rd order upwind biased (MUSCL) differencing scheme with at least 16 grid points within the vortex core showed minimal vortex diffusion at 5*c* downstream (of the trailing edge) station; but, at 10*c*, diffusion was evident.

Conclusions from 2D RANS simulations contained in chapter 3 are as follows:

1) For attached shear flow, the FRSM and SA model give similar results
2) Boundary treatment making use of wall function should be avoided if the highest fidelity solution is sought after; otherwise, their predictions are not far off and they greatly alleviate the challenge of gridding a fully resolved boundary layer

In the steady RANS rotorcraft simulations of chapter 5, it was shown that, despite being a "simple" turbulence model, the SA model with source term modification showed excellent qualitative wake-age resolution.

Appendix A: Vortex Identification

At the crux of this thesis is the proper identification of a tip vortex. There are many quantities that can be used to identify a vortex, see Figure A.1. Tip-vortices are examples of a *coherent structure*. Perhaps one of the best coherent structure identification schemes has been proposed by Jeong and Hussain [9]. A brief overview of their work is included below. Also, results from their identification scheme are shown in Figure A.1 *f)* and Figure A.2.

Jeong and Hussain suggest two requirements that a vortical coherent structure must possess; it must have a net vorticity, and the geometry must be Galilean invariant (invariant to any inertial frame of reference). These requirements, though, do not offer any means of identification. Jeong and Hussain point out shortcomings and counter examples of the three very intuitive methods of vortex identification. That is pressure minimum, spiraling streamlines, and vorticity contours.

Calculating the local pressure minimum, Figure A.1 *a)* in a flow-field can be beneficial to locating the core of a coherent structure. In general, the core of a vortex has a local pressure minimum which works as the majority of the centripetal force for swirling motion (viscous effects can also factor in). Locating pressure minima can be a vague and cumbersome task when one considers the possible presence of stagnation points, jets, adverse pressure gradients, and wakes. An easy counter example to local pressure minimum criteria is a sink or source in the flow-field; there exits a pressure minimum having no vorticity whatsoever.

Another highly intuitive method of vortex identification is depicting a swirling streamline Figure A.1 *d)*. This method of identification is not completely adequate because a streamline does not necessarily have to complete a full-revolution in a coherent structure. This may occur during formation, pairing, tearing, or before decay. In addition, velocity streamlines are not Galilean invariant.

A third method of coherent structure identification is vorticity Figure A.1 *e)*. This is usually a great way to gain insight into a coherent structure but it is very susceptible to "number fudging" and may misrepresent crucial flow details. Finding a "correct" vorticity level to plot is ambiguous. After all, the largest values are likely to occur in a boundary layer. Another similar method that can be used is helicity, Figure A.1 *c)*,

formed by contracting the vorticty vector with velocity. For wing-tip vortices with axial velocity gradients it gives a more definitive identification scheme.

Jeong and Hussain (1995) propose a method of vortex identification, which calculates a local pressure minimum due to vortical motion only. That is, they remove viscous effects and unsteady straining effects. In this scheme, negative values of the middle eigenvalue of the invariant, $s_{ik}s_{kj} + \omega_{ik}\omega_{kj}$, indicates the presence of a coherent turbulent structure. An incompressible 2D equation can be extracted (in $y - z$ coordinates) [26]:

$$\lambda_2 = \left(\frac{\partial v}{\partial y}\right)^2 + \left(\frac{\partial w}{\partial z}\right)^2 + 2\left(\frac{\partial v}{\partial z}\right)\left(\frac{\partial w}{\partial y}\right) \tag{A.1}$$

The 2D $-\lambda_2$ scheme is shown in Figure A.1 *f)*. The 3D scheme is calculated and shown in Figure A.2 for the FRSM, coarse grid finite wing simulation. It is evident that the scheme identifies the coherent structure for the *entire* computational domain (over 100 chord lengths!)—even though the vortex appears completely diffused by other methods. A nice feature about the λ_2 definition is that for highly coherent structures the value scales to magnitudes $O(10^6)$ as shown in Figure A.1 *f)*.

Various vortex identification schemes

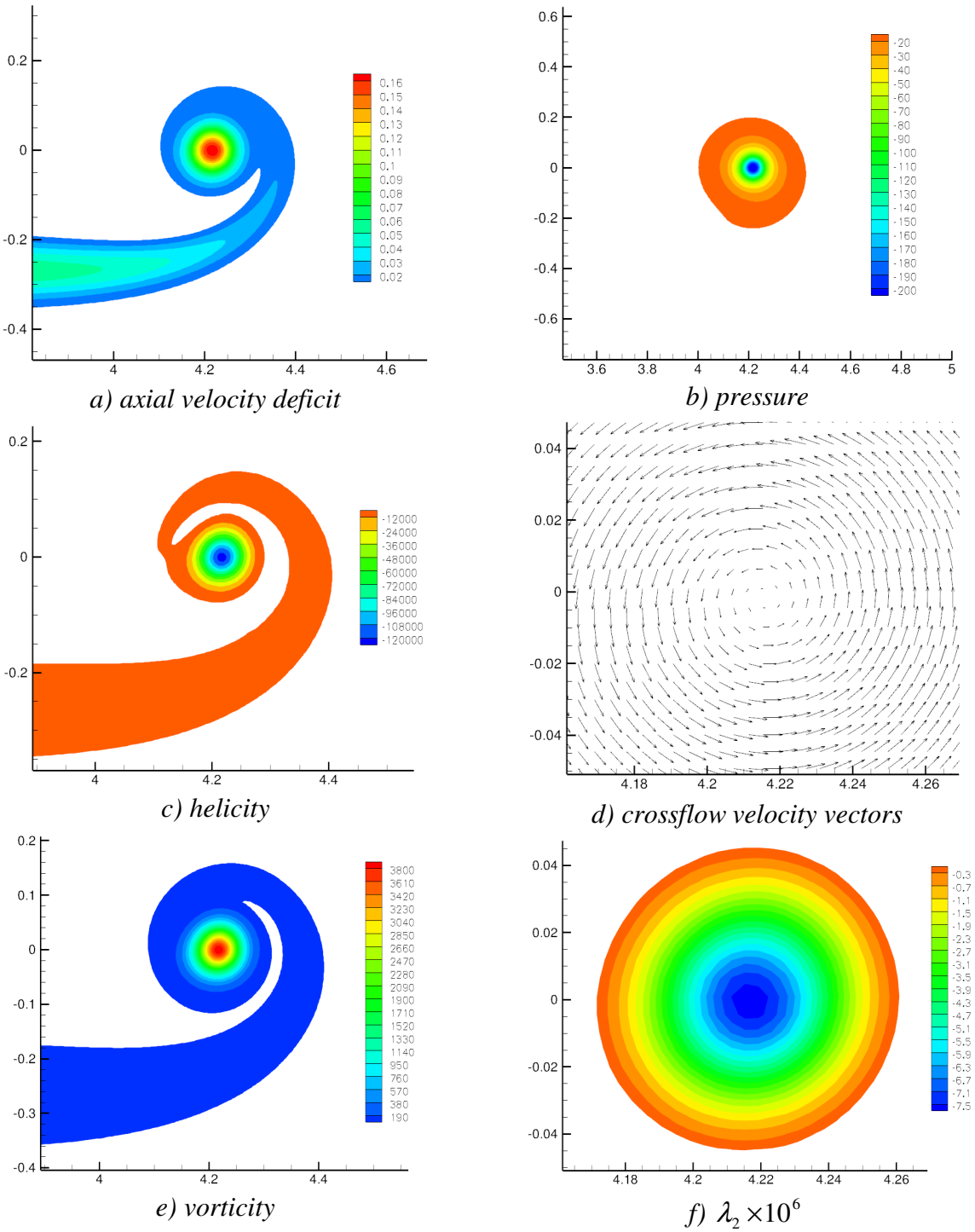

Figure A.1 Comparison of Different Schemes to Identify a Vortex, at the 5c Downstream Station for Finite Wing, Fine Grid, FRSM Simulation

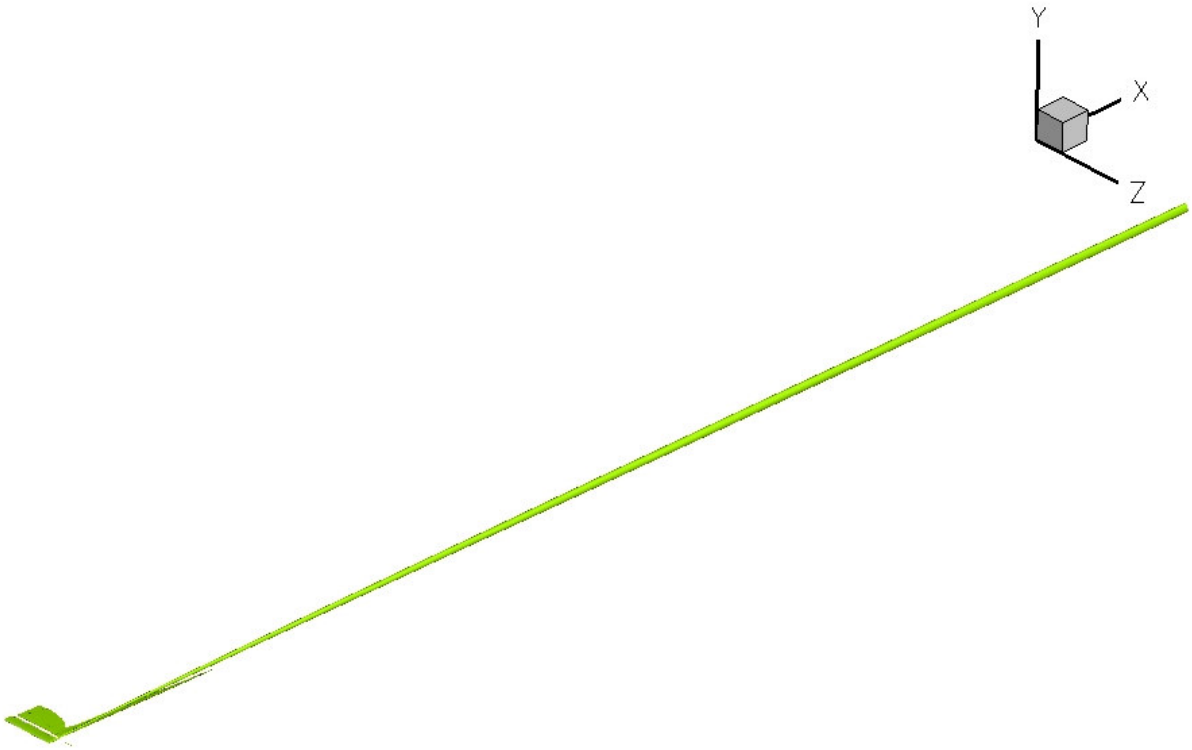

Figure A.2 Isosurface of Lambda 2 for the Finite Wing, Coarse Grid, FRSM Simulation

Appendix B: Airfoil Data Set

Points defining the NACA 0012 and VR 12 airfoil are shown in Table B.1. The data is obtained from the online UIUC airfoil coordinates database [49].

Table B.6.1 Airfoil Coordinate Points

NACA 0012			
Top Surface		Bottom Surface	
X / *c*	Y / *c*	X / *c*	Y / *c*
0	0	0	0
0.0005839	0.0042603	0.0005839	-0.0042603
0.0023342	0.0084289	0.0023342	-0.0084289
0.0052468	0.0125011	0.0052468	-0.0125011
0.0093149	0.0164706	0.0093149	-0.0164706
0.0145291	0.0203300	0.0145291	-0.0203300
0.0208771	0.0240706	0.0208771	-0.0240706
0.0283441	0.0276827	0.0283441	-0.0276827
0.0369127	0.0311559	0.0369127	-0.0311559
0.0465628	0.0344792	0.0465628	-0.0344792
0.0572720	0.0376414	0.0572720	-0.0376414
0.0690152	0.0406310	0.0690152	-0.0406310
0.0817649	0.0434371	0.0817649	-0.0434371
0.0954915	0.0460489	0.0954915	-0.0460489
0.1101628	0.0484567	0.1101628	-0.0484567
0.1257446	0.0506513	0.1257446	-0.0506513
0.1422005	0.0526251	0.1422005	-0.0526251
0.1594921	0.0543715	0.1594921	-0.0543715
0.1775789	0.0558856	0.1775789	-0.0558856
0.1964187	0.0571640	0.1964187	-0.0571640
0.2159676	0.0582048	0.2159676	-0.0582048
0.2361799	0.0590081	0.2361799	-0.0590081
0.2570083	0.0595755	0.2570083	-0.0595755
0.2784042	0.0599102	0.2784042	-0.0599102
0.3003177	0.0600172	0.3003177	-0.0600172
0.3226976	0.0599028	0.3226976	-0.0599028
0.3454915	0.0595747	0.3454915	-0.0595747
0.3686463	0.0590419	0.3686463	-0.0590419
0.3921079	0.0583145	0.3921079	-0.0583145
0.4158215	0.0574033	0.4158215	-0.0574033
0.4397317	0.0563200	0.4397317	-0.0563200
0.4637826	0.0550760	0.4637826	-0.0550769
0.4879181	0.0536866	0.4879181	-0.0536866
0.5120819	0.0521620	0.5120819	-0.0521620
0.5362174	0.0505161	0.5362174	-0.0505161
0.5602683	0.0487619	0.5602683	-0.0487619

VR12			
Top Surface		Bottom Surface	
X / *c*	Y / *c*	X / *c*	Y / *c*
0	0	0	0
0.00012	0.00240	0.00055	-0.00250
0.00080	0.00621	0.00200	-0.00470
0.00195	0.00969	0.00400	-0.00675
0.00340	0.01279	0.00620	-0.00840
0.00520	0.01582	0.00860	-0.00983
0.00700	0.01836	0.01100	-0.01095
0.00900	0.02081	0.01465	-0.01230
0.01105	0.02306	0.01955	-0.01350
0.01415	0.02610	0.02615	-0.01480
0.01860	0.02992	0.03430	-0.01605
0.02450	0.03434	0.04449	-0.01740
0.03205	0.03921	0.05690	-0.01890
0.04160	0.04425	0.07245	-0.02050
0.05350	0.04970	0.09240	-0.02210
0.06850	0.05530	0.11850	-0.02385
0.08800	0.06060	0.15000	-0.02555
0.11400	0.06560	0.20000	-0.02760
0.15000	0.07000	0.25000	-0.02910
0.20000	0.07320	0.30000	-0.03010
0.25000	0.07460	0.35000	-0.03080
0.30000	0.07510	0.40000	-0.03110
0.35000	0.07485	0.45000	-0.03100
0.40000	0.07380	0.50000	-0.03065
0.45000	0.07175	0.55000	-0.03000
0.50000	0.06910	0.60000	-0.02907
0.55000	0.06535	0.65000	-0.02778
0.60000	0.06067	0.69000	-0.02642
0.65000	0.05475	0.73000	-0.02482
0.69000	0.04932	0.77000	-0.02290
0.73000	0.04332	0.81000	-0.02071
0.77000	0.03710	0.84500	-0.01852
0.81000	0.03076	0.88000	-0.01605
0.84500	0.02482	0.91000	-0.01332
0.88000	0.01875	0.93500	-0.01084
0.91000	0.01362	0.95500	-0.00877

0.5841786	0.0469124	0.5841786	-0.0469124
0.6078921	0.0449802	0.6078921	-0.0449802
0.6313537	0.0429778	0.6313537	-0.0429778
0.6545085	0.0409174	0.6545085	-0.0409174
0.6773025	0.0388109	0.6773025	-0.0388109
0.6996823	0.0366700	0.6996823	-0.0366700
0.7215958	0.0345058	0.7215958	-0.0345058
0.7429917	0.0323294	0.7429917	-0.0323294
0.7638202	0.0301515	0.7638202	-0.0301515
0.7840324	0.0279828	0.7840324	-0.0279828
0.8035813	0.0258337	0.8035813	-0.0258337
0.8224211	0.0237142	0.8224211	-0.0237142
0.8405079	0.0216347	0.8405079	-0.0216347
0.8577995	0.0196051	0.8577995	-0.0196051
0.8742554	0.0176353	0.8742554	-0.0176353
0.8898372	0.0157351	0.8898372	-0.0157351
0.9045085	0.0139143	0.9045085	-0.0139143
0.9182351	0.0121823	0.9182351	-0.0121823
0.9309849	0.0105485	0.9309849	-0.0105485
0.9427280	0.0090217	0.9427280	-0.0090217
0.9534372	0.0076108	0.9534372	-0.0076108
0.9630873	0.0063238	0.9630873	-0.0063238
0.9716559	0.0051685	0.9716559	-0.0051685
0.9791229	0.0041519	0.9791229	-0.0041519
0.9854709	0.0032804	0.9854709	-0.0032804
0.9906850	0.0025595	0.9906850	-0.0025595
0.9947532	0.0019938	0.9947532	-0.0019938
0.9976658	0.0015870	0.9976658	-0.0015870
0.9994161	0.0013419	0.9994161	-0.0013419
1.0000000	0.0012600	1.0000000	-0.0012600

0.93500	0.00934	0.97000	-0.00678
0.95500	0.00617	0.98000	-0.00522
0.97000	0.00423	0.99000	-0.00356
0.98000	0.00312	0.99500	-0.00253
0.99000	0.00216	1.00000	-0.00150
0.99500	0.00173		
1.00000	0.00150		

Bibliography

[1] Wilcox, D.C., "Turbulence Modeling for CFD, 3rd Edition," San Diego, California: Birmingham Press, Inc., 2006.

[2] Lamb, H., "Hydrodynamics," Cambridge University Press, 1916.

[3] Moin, P., and Kim, J., "Tracking Turbulence with Supercomputers," *Scientific American*, Vol. 276, 1997.

[4] Moin, P., and Mahesh, K., "Direct Numerical Simulation: A Tool in Turbulence Research," *Annual Review of Fluid Mechanics*, Vol. 30, 1998.

[5] Biferale, L., Blank, M., Frisch, U., "Chaotic Cascades with Kolmogorov 1941 Scaling," *Journal of Statistical Physics,* pp. 781-795, 1994.

[6] Kolmogorov, A.N., *Turbulence and Stochastic Process: Kolmogorov's Ideas 50 Years On*, "Dissipation of Energy in the Locally Isotropic Turbulence," *Mathematical and Physical Sciences*, Vol. 434, No. 1890, 1991.

[7] Zhou, Y., "Implications of Turbulence Interactions: A Path Toward Addressing Very High Reynolds Number Flows," *Conference on Turbulence and Interactions, France*, 2006.

[8] Spalart, P.R., "Strategies for Turbulence Modeling and Simulations," *International Journal of Heat and Fluid Flow*, Vol. 21, 2000.

[9] Jeong, J. and Hussain, F., "On the Identification of a Vortex," *Journal of Fluid Mechanics*, Vol. 285, pp. 69-94, 1995

[10] Page, R.D., Clawson, K.L., Garodz, L.J., Rudis, R.P., "Report on Tower Fly-by Testing," *Proceedings of the FAA Wake Vortices Conference,* Washington, D.C., 1991.

[11] Martin, P.B., Pugilese, G.J., Leishman, J.G., "High Resolution Trailing Vortex Measurements in the Wake of a Hovering Rotor," *Proceedings of the 53rd Annual Forum of the American Helicopter Society,* 2001.

[12] Moore, D.W. and Saffman, P.G., "Axial Flow in Laminar Trailing Vortices," *Proceedings of the Royal Society, London, A*., Vol. 333, 1973.

[13] Jacquin, L., and Pantano, C., "On the Persistence of Trailing Vortices," *Journal of Fluid Mechanics*, Vol. 471, 2002.

[14] Zeman, O., "The Persistence of Trailing Vortices: A Modeling Study," *Center for Turbulence Research*, In: *Physics of Fluids, American Institute of Physics*, 1995.

[15] Devenport, W.J., Rife, M.C., Liapis, S.I., and Follin, G.J., "The Structure and Development of a Wing-tip Vortex," *Journal of Fluid Mechanics*, Vol. 312, 1996.

[16] Spalart, P.R., "Airplane Trailing Vortices," *Annual Review of Fluid Mechanics*, Vol. 30, 1998.

[17] Green, S.I., Acosta, A.J., "Unsteady Flow in Trailing Vortices," *Journal of Fluid Mechanics,* Vol. 227, 1991.

[18] Heyes, A.L., Jones, R.F., Smith, D.R., "Wandering of Wing-tip Vortices," *Proceedings of the 12th International Symposium on Application of Lase Techniques to Fluid Mechanics,* Lisbon, 2004.

[19] Leishman, J.G., "Principles of Helicopter Aerodynamics," Cambridge University Press, 1998.

[20] Chow, J.S., Zilliac, G.G., and Bradshaw, P., "Mean and Turbulence Measurements in the Near Field of a Wingtip Vortex," *AIAA Journal*, Vol. 35, No. 10, 1997.

[21] Komerath, N., Wong, O., and Ganesh, B., "On the Formation and Decay of Rotor Blade Tip Vortices," *AIAA/34th Fluid Dynamics Conference and Exhibit, Oregon*, 2004.

[22] Duraisamy, K., "Studies in Tip Vortex Formation, Evolution and Control," *Ph.D. Dissertation, Department of Aerospace Engineering, University of Maryland*, 2005.

[23] Lockard, D.P., and Morris, P.J., "Wing-Tip Vortex Calculations Using a High-accuracy Scheme," *Journal of Aircraft*, Vol. 35, No. 5, 1998.

[24] Wallin, S. and Girimaji, S.S., "Evolution of an Isolated Turbulent Trailing Vortex," *AIAA Journal*, Vol. 38, No. 4, 2000.

[25] Bhagwat, M., Moulton, M.A., and Caradonna, F.X., "Hybrid CFD for Rotor Hover Performance Prediction," *AIAA/24th Applied Aerodynamics Conference, California*, 2006.

[26] Lui, Y., Yu, X., and Lui, B., "Turbulence Models Assessment for Large-Scale Tip Vortices in an Axial Compressor Rotor," *Journal of Propulsion and Power*, Vol. 24, No. 1, 2008.

[27] Dacles-Mariani, J., Kwak, D. and Zilliac, G., "On Numerical Errors and Turbulence Modeling in Tip Vortex Flow Prediction," *International Journal for Numerical Methods in Fluids,* Vol. 30, 1999

[28] Ragab, S. and Sreedhar, M., "Numerical Simulations of Vortices with Axial Velocity Deficits," *Physics of Fluids*, Vol. 7, 1995.

[29] Egolf. T.A., "Recent Rotor Wake Simulation and Modeling Studies at United Technologies Corporation," *AIAA Paper 2000-0115*, 2000.

[30] Qin, J.H., "Numerical Simulations of a Turbulent Axial Vortex," *Ph.D. Thesis, Department of Aerospace Engineering, Purdue University*, 1998.

[31] Spalart, P.R., "Trends in Turbulence Treatments," *AIAA Paper 2000-2306*, 2000.

[32] Lumley, J. L., "Toward a Turbulent Constitutive Equation," *Journal of Fluid Mechanics,* Vol. 41, 1970.

[33] Saffman, P.G., "A Model for Inhomogenous Turbulent Flow," *Proceedings of the Royal Society of London,* Vol. A317, 1970.

[34] Wilcox, D.C., Rubesin, M.W., "Progress in Turbulence Modeling for Complex Flow Fields Including Effects of Compressibility," *NASA TP-1517,* 1980.

[35] Craft, T.J., Launder, B.E., and Suga, K., "Development and Application of a Cubic Eddy-Viscosity Model of Turbulence," *International Journal of Heat and Fluid Flow 17*, pp. 108-115, 1995.

[36] Pettersson-Reif, B.A., Durbin, P.A., and Ooi, A., "Modeling Rotational Effects in Eddy-viscosity Closures," *International Journal of Heat and Fluid Flow*, Vol. 20, No. 6, 1999.

[37] Spalart, P.R., and Shur, M., "On the Sensitization of Turbulence Models to Rotation and Curvature," *Aerospace Science and Technology*, Vol. 1, No. 5, 1997.

[38] Menter, F.R., Kuntz, M., and Langtry, R., "Ten Years of Industrial Experience with the SST Turbulence Model," Ed. Hanjalic K., Nagano, Y., and Tummers, M., In: *Turbulence, Heat, and Mass Transfer 4, Begell House Inc, New York*, pp. 625-632, 2003.

[39] FLUENT 6.3 User's Guide, FLUENT Inc., Lebanon, NH, 2006.

[40] Jakirlic, S., Hanjalic, K., and Tropea, C., "Modeling Rotating and Swirling Turbulent Flows: A Perpetual Challenge," *AIAA Journal*, Vol. 40, No. 10, 2002.

[41] Thakur, S. and Shyy, S., "Reynolds Stress Models for Flows in Complex Geometries: Review and Application," *AIAA 99-3782*, 1999.

[42] Hytopoulos, E. and Simpson, R.L., "Critical Evaluation of Recent Second-Order Closure Models," *AIAA-93-0081*, 1993.

[43] Srinivasan, G.R., and Baeder, J.D., "TURNS: A Free-wake Euler/ Navier-Stokes Numerical Method for Helicopter Rotors," *AIAA Journal*, Vol. 31, No. 5, 1993.

[44] Dimanlig, A.C.B., Meadowcroft, E.T., Strawn R., and Potsdam, M., "Computational Modeling of the CH-47 Helicopter in Hover," *IEEE Computer Society*, 2007.

[45] Mazher, A.K., "A New Approach to Dynamic Modeling of Turbulence," *AIAA/4th Theoretical Fluid Mechanics Meeting, Ontario, Canada*, 2005.

[46] Farve, A., "Equations des Gaz Turbulents Compressibles," *Journal de Mecanique,* Vol. 4, 1965.

[47] Spalart, P.R., and Allmaras, S.R., "A One-Equation Turbulence Model for Aerodynamic Flows," *AIAA Paper 92-0439*, 1992.

[48] Launder, B. E., Reece, G. J., Rodi, W., "Progress in the Development of a Reynolds-Stress Turbulence Closure," *Journal of Fluid Mechanics,* Vol. 68, 1975.

[49] "UIUC Airfoil Coordinates Database," 2008. *University of Illinois at Urbana Champaign.* 2009 <http://www.ae.uiuc.edu/m-selig/ads/coord_database.html>

[50] Sheldahl, R. E., Klimas, P. C., "Aerodynamic Characteristics of Seven Airfoil Sections Through 180 Degrees Angle of Attack for Use in Aerodynamic Analysis of Vertical Axis Wind Turbines," *SAND80-2114*, Albuquerque, New Mexico, 1981.

[51] Launder, B. E., Spalding, D. B., "The Numerical Computation of Turbulent Flows,"*Computer Methods in Applied Mechanics and Engineering*, 3:269, 1974.

[52] Guo, Y. and Chang, K.C., "On the Calculation of Reynolds Stresses by CFD," *AIAA/35th Fluid Dynamics Conference and Exhibit, Ontario, Canada*, 2005.

[53] Devenport, W. J., *Personal Communication,* Virginia Tech, 2009.